FABRICATION OF FINEGRAINED SIC AND SIC-EXFOLIATED GRAPHENE NANOCOMPOSITES USING SPARK PLASMA SINTERING OF POLYMER DERIVED SIC

By

ARIF RAHMAN

Bachelor of Science in Mechanical Engineering
Bangladesh University of Engineering and Technology
Dhaka, Bangladesh
2006

Master of Science in Mechanical Engineering
Oklahoma State University
Stillwater, OK, USA
2009

Submitted to the Faculty of the
Graduate College of
Oklahoma State University
in partial fulfillment of
the requirements for
the Degree of
DOCTOR OF PHILOSOPHY
July, 2014

FABRICATION OF FINEGRAINED SIC AND SIC-EXFOLIATED GRAPHENE NANOCOMPOSITES USING SPARK PLASMA SINTERING OF POLYMER DERIVED SIC

Dissertation Approved:

Dr. Raman P. Singh

Dissertation Advisor

Dr. Sandip P. Harimkar

Dr. Jay C. Hanan

Dr. Ranji Vaidyanathan

Name: ARIF RAHMAN
Date of Degree: JULY, 2014
Title of Study: FABRICATION OF FINEGRAINED SIC AND SIC-EXFOLIATED GRAPHENE NANOCOMPOSITES USING SPARK PLASMA SINTERING OF POLYMER DERIVED SIC
Major Field: MECHANICAL ENGINEERING
Abstract:

In spite of excellent thermo-mechanical properties of silicon carbide (SiC), its application is limited due to its inherent brittle nature. Inclusion of a high strength and high modulus second phase can potentially improve the fracture toughness of SiC with proper processing. This study presents a systematic approach to understand the effect of processing parameters on sintering of SiC matrix without binders first, and then effect of graphene reinforcement on mechanical and microstructural properties of SiC.

At first, nanostructured bulk SiC ceramics are processed using a novel approach that combines pyrolysis of preceramic polymer and spark plasma sintering (SPS). Allylhydridopolycarbosilane (AHPCS) is used as the preceramic polymer and pyrolyzed under inert conditions to produce SiC powder. Fourier transform infrared spectroscopy (FTIR) confirmed complete conversion of preceramic polymer to amorphous SiC at 1400 °C. Subsequently, spark plasma sintering (SPS) technique is used to compact the SiC powder at temperatures ranging from 1600 to 2100 °C at a uni-axial pressure of 70 MPa and a soak time of 10 minutes. *In situ* crystallization of amorphous SiC using SPS results in fine grained structure ranging from 97–540 nm. Close to theoretical density materials are obtained, at the higher sintering temperatures, with mechanical properties that exceed those of commercially available micron-sized sintered silicon carbide.

Later, the effect of graphene nanoplatelets on the microstructure and mechanical properties of silicon carbide (SiC) was investigated. Graphene nanoplatelets are dispersed in a liquid preceramic polymer by ball milling. Pyrolysis of the graphene nanoplatelet–preceramic polymer slurry results in near-stoichiometric SiC–graphene nanoplatelet powder. This method leads to improved dispersion of graphene in the SiC matrix as compared to conventional mechanical blending of dry powders and thereby significantly influences the resulting mechanical properties. Subsequently, spark plasma sintering (SPS) is used to consolidate dense bulk SiC–graphene composites with varying graphene content up to a maximum of 5 wt.%. X-ray diffraction (XRD) and scanning electron microscopy (SEM) investigations reveal that inclusion of graphene restricts grain growth of SiC matrix during SPS processing. Fracture toughness of SiC-graphene composite is increased by 40% with the inclusion of 2 wt.% graphene nanoplatelets. However, for higher graphene content the change in fracture toughness is limited. Improvement in fracture toughness is due to crack deflection mechanism provided by the graphene platelets. Similar graphene content also resulted in 20% improvement in flexural strength. Finally, Raman spectroscopy is used to understand the complex effect of sintering temperature and pressure on graphene nanoplatelet.

TABLE OF CONTENTS

LIST OF TABLES

Table Page

LIST OF FIGURES

CHAPTER I

Introduction

β-silicon carbide (β-SiC) exhibits unique properties which include high hardness, elastic modulus, thermal stability, and chemical/oxidation resistance [18–20]. In spite of these excellent properties, one major factor that limited the use of SiC in structural application is its inherent brittleness (low fracture toughness) [21–23]. Reducing ceramic grain size to nanoscale along with nanoscale reinforcement in ceramic matrix results in improvement in fracture toughness [24–33]. Nanoscale fillers also have potential for improving other properties of ceramic matrix composites (CMCs). For instance, carbon nanotubes (CNTs) significantly affect electrical and thermal properties of CMCs [12, 34–37]. However, processing of nanograined CMCs is difficult. Processing issues include grain growth during sintering process [38–40] and dispersion of nanofillers (such as CNTs) in the ceramic matrices [41–43]. Hence, it is critically important to overcome these processing issues to understand the potential of nanograined CMCs to full extent in advanced applications. Graphene, a recently discovered material, is one of the strongest filler materials available today and is expected to replace CNTs due to its excellent properties and relative ease of processing/dispersion in various material matrices [15, 44, 45]. The reinforcement with graphene in the SiC is expected to not only enhance the toughness and thermal conductivity of the composite but also restrict the grain growth of the ceramic matrix [16]. Following sections of this background review highlight the current understanding of the processing and properties of the SiC, CMCs, and graphene as a nanofiller.

I.1 SiC structure, polytypes and properties

SiC exhibits unique intrinsic properties due to the strong covalent bond between the Si and C atoms. Si and C belong to group IV and have 4 valence electrons. Four sp^3 electron orbitals are formed by hybridization of one s and three p electrons. These orbitals are arranged in a symmetric tetrahedron so that each carbon atoms form closed packed parallel layers with the Si atom situated in the tetrahedron holes between the layers. Crystals of SiC have layered structure of the tetrahedra and stacking sequence of these layers decides the polytype of the material. There are two phases of SiC, namely β-SiC and α-SiC. The β phase has a cubic lattice with an ABCABC... stacking sequence. This phase is also known 3C polytype where the 3 refers to 3 layers in a unit cell and C refers to the cubic crystal structure. The α phase is either hexagonal or rombohedral crystal structure that can exist as any of the 200 known polytypes based on the stacking sequence [5]. Most common α phases are 2H with a stacking sequence of ...ABAB..., 4H with a stacking sequence of ...ABAC..., 6H with a stacking sequence of ...ABCACB..., and 15R with stacking sequence of ...ABCBACABACBCACB...Fig. I.1 shows schematic stacking in 3C, 6H, 4H, and 15R SiC polytypes. The β phase has been considered as a low temperature phase, stable up to 1500°C to 2000°C whereas the α phase is considered a high temperature phase. It is believed that the β phase transforms into one or more α phase at temperatures above 2000°C unless there is a stabilizing agent that changes the transformation temperature. However, later on it was found that β phase can exist at higher temperature and should not be considered a low temperature phase [46]. Moreover, the 3C-SiC is considered more stable compared to other hexagonal polytypes of SiC up to a temperature of 2100°C [1]. The stability of different polytypes depends on temperature, impurities, growth kinetics, and supersaturation. Elements from group III and V have been shown to stabilize polytypes of SiC. For example, aluminum and boron have stabilizing effect on 4H-SiC whereas nitrogen and phosphorus seems to stabilize 3C-SiC [5].

Even though there is a variation in stacking sequence in SiC polytypes, the bonding

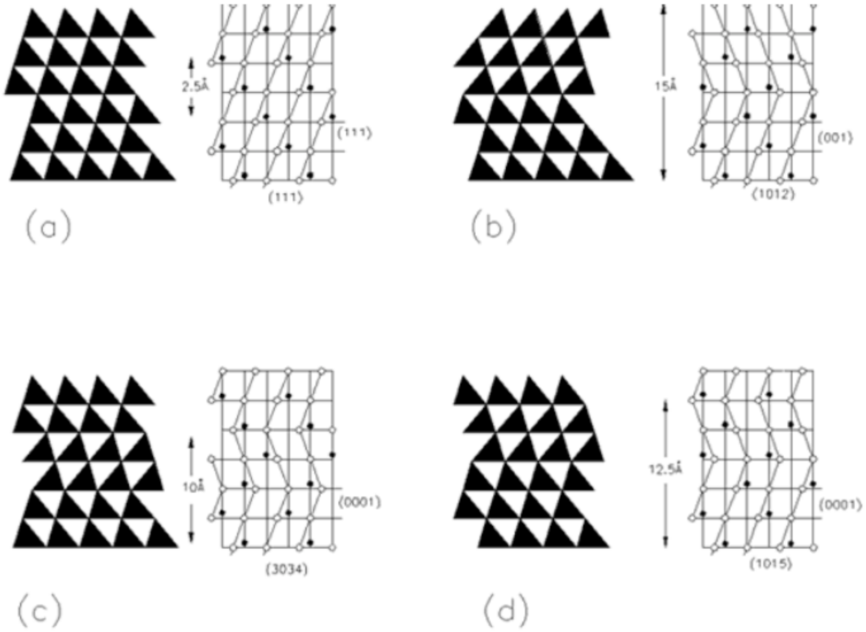

Figure I.1: Schematic representation of stacking in (a) 3C-SiC, (b) 6H-SiC, (c) 4H-SiC, and (d) 15R-SiC [5].

Property	3C-SiC	2H-SiC	4H-SiC	6H-SiC
Lattice constant, a (nm)	0.43589	0.3081	0.3081	0.3081
Lattice constant, c (nm)	-	0.5031	1.0061	1.5092
Density (g/cc)	3.215	3.219	3.215	3.215
Band gap (eV)	2.39	3.33	3.26	3.0
Electron mobility (cm^{2}V^{-1}s^{-1})	$\leq$1000	–	$\leq$850	$\leq$450
Thermal conductivity (W cm^{-1}K^{-1})	3.2	–	3.7	4.9

Table I.1: Physical, electrical and thermal properties of different SiC polytypes [1] between Si and C is 88% covalent and 12% ionic with a bond distance of 1.89 Å in all polytypes. Hence effect of stacking sequence on properties of SiC polytype is dependent on the property being measured. While electronic and thermal properties show dependence on stacking sequence, mechanical properties show no such dependence [1, 2]. For example, band gap and thermal conductivity of different polytypes differ due to their structure as shown in table I.1. Due to smaller band gap, 3C-SiC provides some advantages over other α phases such as isotropic electron Hall mobility which is higher than 4H and 6H polytypes. In contrast, mechanical properties of SiC show dependence on microstructure (grain size and morphology), impurities at grain boundaries, and structural defects (porosity). In fact, mechanical properties of two most commonly used polytypes of SiC (6H and 3C) show similar trend as found in several references [3, 47]. For comparison, table I.2 shows common mechanical properties usually determined in experimental studies for β-SiC and 6H(α)-SiC. From these data one can conclude that different polytypes have little/no effect on mechanical properties of SiC.

Mechanical Property	3C-SiC	6H-SiC
Elastic modulus (GPa)	392 – 448	410 – 450
Vicker's hardness (GPa)	20.7 – 24.5	24.9 – 26.7
Flexural strength (MPa)	360 – 424	340 – 420
Fracture toughness (MPa $m^{1/2}$)	2.6 – 3.7	2.6 – 3.4

Table I.2: Mechanical properties of two most commonly found SiC polytypes [2, 3]

I.2 Synthesis of SiC

Berzelius, a Swedish chemist, was the first to report the probability of existence of SiC as a compound in nature in 1824 [48]. Later, it was separately experimentally synthesized in the laboratory by Despretz (1849), Schutzenberger (1881), and Moissan (1891) [49]. Moissan also discovered natural silicon carbide in an iron meteorite, hence the mineral name "moissanite" after his name. However, it was Edward Goodrich Acheson who came up with the process for large scale SiC production in 1891 [50] and the process was named after his name as "Acheson process". In this process, a mixture of silica and coke were heated to a very high temperature of 2600°C to produce SiC by the following reaction:

$$\mathrm{SiO_2} + 3\,\mathrm{C} \longrightarrow \mathrm{SiC} + 2\,\mathrm{CO}$$

The Acheson process has been one of the most widely used commercial process for large scale SiC production. α-SiC is produced by higher temperature reaction (2200°C to 2600°C). SiC crystals produced in this process are then milled and purified to obtain a commercial grade silicon carbide powder. Alternatively, β-SiC powder is produced by carbothermal reduction of high purity silica by carbon black in the temperature range of 1500 – 1800°C.

There have been few other synthesis methods that are being used for producing SiC powder. Among them, sol-gel method uses reaction of silicon and carbon at high temperature to produce SiC power [51, 52]. Gas phase synthesis method utilizes reaction between SiH_4 or $SiCl_4$ and hydrocarbon such as CH_4 [53, 54]. Polymer precursor route is another promising process for synthesis of high purity, nanocrystalline SiC. In this process, ceramic is derived from thermal decomposition of preceramic organosilicon polymer [55]. Advantage of polymer pyrolysis includes lower average processing temperature, hence control over microstructure of the produced powder.

I.2.1 Preceramic polymers for SiC synthesis

Silicon carbide fibers were first fabricated by Yajima *et al.* using a preceramic polymer [56]. After that, polymer derived silicon-based ceramics has been an active area of research. Yajima *et al.* used polycarbosilane (PCS) as polymer precursor. In PCS the 1:2 Si:C ratio results in excess carbon in the SiC fiber and due to this excess carbon, the mechanical properties of this nonstoichiometric amorphous SiC fiber is inferior compared to bulk, crystalline stoichiometric SiC [57]. Also, excess carbon limits the fiber application temperature to ∼ 1200°C, since, at higher temperature oxygen reacts with silicon and carbon to produce gaseous products and affects the fiber properties [57]. In order to achieve stoichiometric SiC, different polymer precursors with 1:1 Si:C were explored. Polymethylsilane (PMS) and polysilethylene (PSE) are two such polymer precursors. Pyrolysis of PMS produces excess silicon with low ceramic yield. Excess silicon reduces oxidative stability at higher temperature and can compromise the integrity of the ceramic part due to swelling at higher temperature. Polysilethylene (PSE) produces improved materials, but requires an expensive method of preparation.

To address the issue of excess C or Si, efforts have been made to achieve stoichiometric SiC from polymer precursors. Researchers have explored blends of polymer or copolymer precursors to fabricate stoichiometric SiC. Some of them have succeeded to fabricate near stoichiometric SiC with ceramic yield of ∼60% [58, 59]. Problem with these precursors are their synthesis are multistep with low chemical yield making them expensive [60].

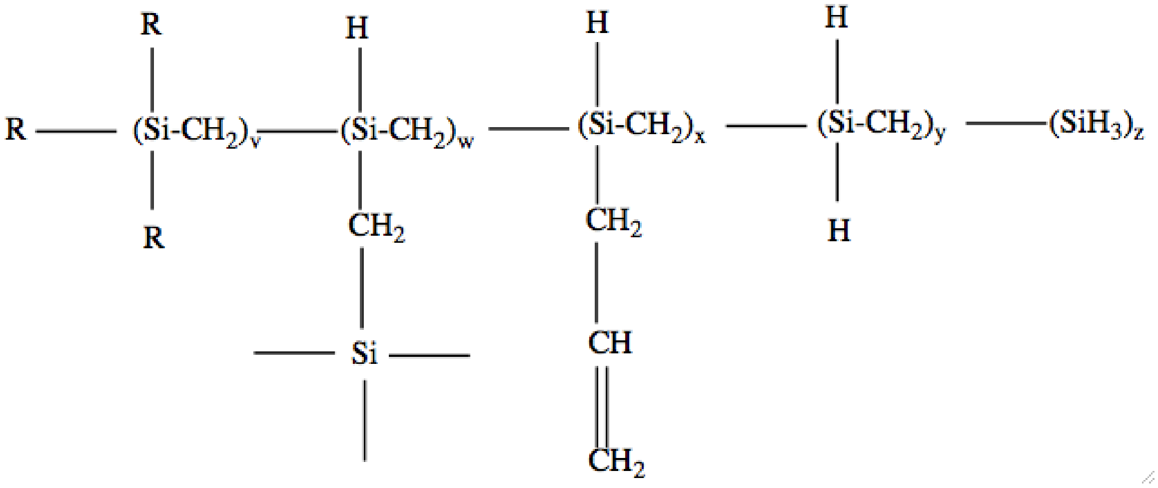

Figure I.2: Nominal structure of AHPCS [6]

Other than stoichiometry of SiC, there are certain requirements that must be met for the preceramic polymer to be useful [61]. First of all, the preceramic polymer must be in a form that is processable by conventional processing technique. Depending on its application, there might be requirements of solubility in organic solvent, fusibility for forming stable melt if it is a solid, and for some applications, there might be requirements of liquid precursor of different viscosity. Finally, an important requirement for a polymer precursor to be useful is, high ceramic yield upon pyrolysis. The desirable ceramic yield is $\sim$80% or higher.

Considering all these requirements, the polymer precursor used in this study is allylhydridopolycarbosilane(AHPCS) which is commercially available. AHPCS is a modified version of a higly branched polycarbosilane HPCS (hydridopolycarbosilane). Whitmarsh *et al.* [62] first reported successful synthesis of AHPCS by Grignard coupling of (choloromethyl)trichlorosilane that produced chloropolycarbosilane, then a small percentage (5-10%) of Si-H group was substituted with Si-allyl group before reduction with lithium aluminum hydride to produce AHPCS. As shown in figure I.2, AHPCS has a nominal structure of $[Si(CH_2CH{=}CH_2)_2CH_2]_{0.1}[SiH_2CH_2]_{0.9}$ [63]. Like HPCS, AHPCS has a 1:1 Si:C ratio and high ceramic yield with low volume shrinkage [63]. It is stable in air for several hours and has a low modifiable viscosity [64]. According to Starfire Systems Co. (Malta, NY) AHPCS has a ceramic yield of $\sim$80–85% [4]. AHPCS has been widely evaluated as potential candidate for coating material, as a binder for ceramic powders as well as a source of matrix for ceramic matrix composites [65].

Property	**SMP–10 (AHPCS)**
Density	0.998
Appearance	Clear, Amber liquid
Viscosity	45 to 120 cps at 25°C
Solubility	Hexanes, Toulene, Insoluble in water
Flash Point	89°C (192°F)
Moisture Absorbtion	$< 0.1\%$ in 24 hrs at room temperature
Nominal Cure Temperature	250 to 400°F
Surface Tension	30 dynes/sq.cm

Table I.3: Properties of AHPCS [4].

The properties of AHPCS are listed in table I.3, as provided by Starfire systems. According to Starfire systems, the polymer cures to a green body at a temperature of 180–400°C and converts to a fully ceramic amorphous SiC at 850–1200°C with minimal shrinkage.

I.3 Processing of SiC

Bulk processing of SiC is considered difficult due to strong covalent bond in Si–C and low self diffusivity. Sintering is the most commonly used technique for densification of powder SiC into bulk form. Sintering is a thermal treatment process on loose particles to bond them into coherent solid structure via mass transport that occur on atomic scale [66]. Densification and grain coarsening are two competing mechanisms during sintering. The driving force for sintering is the minimization of the total interfacial energy. So, the process is modeled as a function of change in interfacial energy (densification) and change in interfacial area (grain growth) as shown in Eqn I.1 [7].

$$\Delta(\gamma A) = (\Delta\gamma)A + \gamma(\Delta A) \tag{I.1}$$

Where γA is the total interfacial energy of the powder compact, A is the total surface area, and γ is the specific surface energy. So, $\Delta(\gamma A)$ represents the total change in interfacial energy due to densification and grain coarsening. $\gamma(\Delta A)$ represents grain coarsening as there is only change in interfacial area while interfacial energy remains same. And finally, $(\Delta\gamma)A$ represents densification where $\Delta\gamma$ relates lowering the surface free energy by replacement of solid/vapour interface by solid/solid interface. This process is shown in fig I.3.

In a broad sense, sintering can be classified into two main mechanisms, namely, solid state sintering and liquid phase sintering. In solid state sintering, densification occurs through lattice and grain boundary diffusion of mass without any presence of wetting liquid at the grain boundary. During solid state sintering the powder compact undergoes three different stages [67]. In the initial stage, inter-particle neck growth takes place with center to center approach of several percent through surface diffusion, vapor transport, plastic flow or viscous flow. Surface diffusion is dominant among these processes as lower energy is required to break fewer number of interatomic bonds during this process. In the intermediate stage, the inter-particle necks grow and grain boundary diffusion moves atoms to fill pores so as to satisfy the force balance in the triple junction defining a dihedral angle. This angle depends on the sold-vapour to solid-solid surface energy ratio. Initially, the pore phase is continuous interconnected channel throughout the triple surface intersections. Eventually, continuous shrinkage in the pore phase makes it discontinuous and results in almost $\sim$ 20% shrinkage in this stage. During the final stage, pore phase continually shrinks and entrapped at the four grain corners as closed spheres. In ideal case, these pores would shrink to zero size in stable manner with the material becoming dense solid reaching the theoretical density. However, instead of complete pore shrinkage, exaggerated grain growth occurs through bulk and grain boundary diffusion resulting in reduced grain boundary area. Densification during this step is close to 3–5%. Fig. I.4 depicts different diffusion mechanisms taking place during solid state sintering.

Liquid phase sintering (LPS) can be considered a sintering mechanism of two phase systems where one phase is in liquid form during the sintering process (Fig. I.5). Usually,

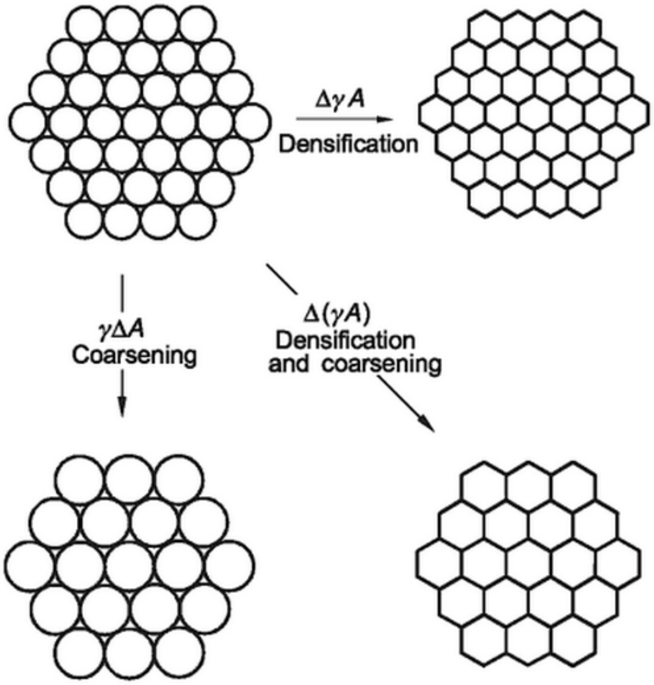

Figure I.3: Two competing mechanisms during sintering under the driving force for sintering [7].

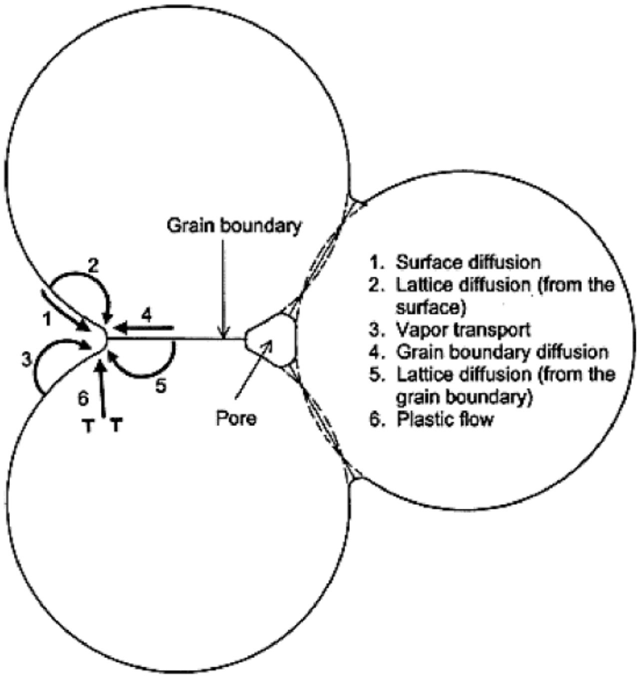

Figure I.4: Different diffusion mechanisms taking place during sintering in a three particle array [8].

4 – 15 wt% of additive is added as a secondary phase in LPS. Decrease in surface area of pores in the liquid phase is responsible for the change in free energy and considered the driving force for sintering in this case. For complete densification the requirements are, (1) an appreciable amount of liquid forming during sintering, (2) reasonable solubility of the solid in the liquid phase, and (3) complete wetting of the solid [68]. LPS consists of three distinct stages [69]. The first stage is the redistribution of the liquid phase and rearrangement of the solid particles under capillary pressure gradients. After reaching the sintering temperature the additive wets the solid surface by forming liquid and surface tension forces particle rearrangement. Particle rearrangement is favored by distribution of the liquid phase between particles and inside pores caused by the capillary pressure. In this case, the solid particles have to be wet properly by the liquid phase. This depends on the surface tension of the liquid in general. Liquids with low surface tension provides better wetting capability compared to liquids with high surface tension. Increase in packing efficiency is responsible for sharp density increase during this stage. The second stage is densification through

solution re-precipitation and grain shape accommodation. In the solution re-precipitation process atoms usually dissolve from smaller particles into the liquid inter-granular phase and then precipitate onto the larger particles. The rate of this process depends on the solubility of the solid phase into the liquid phase. Grain coarsening results in pore elimination by grain shape adjustment through out this process. In the final stage, densification slows down as the microstructure consists of connected solid grains with liquid occupying spaces between the grains. This stage is similar to solid-state sintering where grain growth continues as the compact sinters to full density or trapped gas in the pores stop densification.

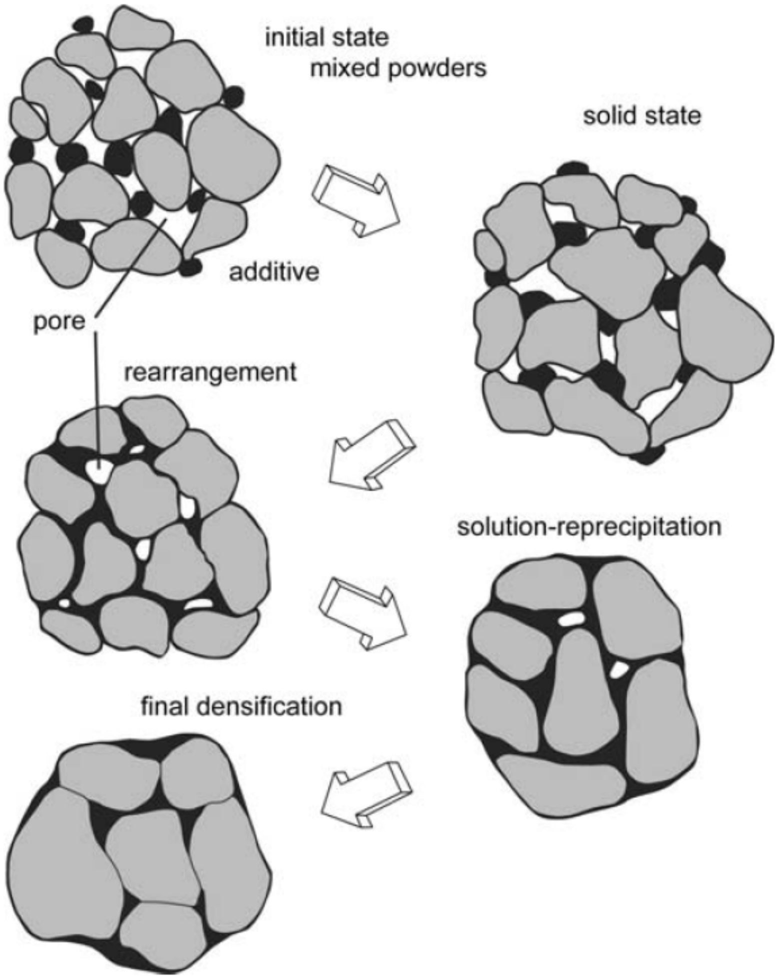

Figure I.5: Schematic representation of different stages of liquid phase sintering [9].

Based on these sintering mechanisms several sintering techniques have been utilized to densify ceramic material. They are briefly discussed below.

I.3.1 Pressureless sintering

This is also known as high temperature sintering. In this method, high temperature for longer duration is used to sinter highly covalent material. Since no external pressure is applied, this method provides the possibility of any size and shape of sample. However, absence of pressure makes the densification difficult. To improve the process, additives can be used. These binder materials can also cause decomposition reactions (especially oxide additives) as the sintering takes place at very high temperature for longer durations and thereby hinder the densification process.

Prochazka was the first to sinter silicon carbide with small amount of carbon and boron using pressureless sintering [70]. Later several authors have reported sintering silicon carbide using pressureless sintering. Mulla et al. have used small CO pressure for sintering SiC with addition of Al_2O_3 [71]. This inhibited the reaction between SiC and Al_2O_3 and improved densification. However, free Si phase was formed during the sintering process that is detrimental for high temperature mechanical properties. Moreover, exaggerated grain growth occurred due to longer sintering time (≥ 30 min).

I.3.2 Hot pressing (HP)

To avoid longer sintering time with higher sintering temperature, pressure is simultaneously introduced during sintering and this process is termed as hot pressing. This external pressure acts as a driving force for densification by increasing the rearrangement of the particles. Moreover, during the final stage of sintering this external pressure acts against the internal pore pressure favoring reduction of porosity without exaggerated grain growth. Use of lower sintering temperature in hot pressing allows densification with finer equiaxed grains. It also enables sintering without the use of secondary phase. For this reason, highly covalent ceramics like silicon carbide or silicon nitride can be sintered to bulk dense bodies using hot pressing. Nonetheless, hot pressing is associated with very high production cost and its use is limited in industry. Moreover, this process is limited to sintering only simple shapes and also has restriction on the size of the part that can be sintered.

Lange reported hot pressing behavior of SiC using Al_2O_3 as binding agent [72]. SiC was sintered to near theoretical density under 28MPa pressure and 1950°C sintering temperature for 1 hour. Al_2O_3 formed a liquid phase during sintering and resulted in a fine microstructure with grain size between 2 – 4 μm. Recently, other researchers have used hot pressing to sinter SiC using different additive systems close to theoretical density [73, 74]. Room temperature mechanical properties were found to be excellent due to finer microstructure. However, mechanical properties degraded rapidly at higher temperature due to softening of the amorphous grain boundary phase.

I.3.3 Hot isostatic pressing (HIP)

Hot isostaic pressing is similar to hot pressing except the pressure is applied isostatically by a gas. Argon or nitrogen is generally used for exerting pressure in HIP-ing. In this method, a glass or metal container is used to hold the green body under vacuum and placed in a pressure vessel. During sintering a few thousand psi pressure is maintained on the green body by a compressor and gas pressure is increased to higher value so that the closed porosity collapse before complete densification. HIPing can be done to a temperature of 2200°C and a pressure of 200 MPa. This technique provides the ability to process complex geometry unlike hot pressing. HIPing is commercially used to remove closed porosity in metal castings.

Since HIPing provides ability to produce finer microstructure, the influence of smaller grain size on mechanical properties of SiC was investigated by Vassen et al. [75, 76] using HIPing. In that study, material was fabricated using hot isostatic pressing (HIP) of nanograined SiC powder of particle size 20 nm with 1 wt% of boron and 1 wt% of carbon as additives. Temperature of 1700°C and pressure of 350 MPa were used for sintering SiC with grain size of 150 nm. Subsequently, a modification of the fabrication process in the form of heat treatment before HIPing led to reduced grain size of 80 nm in the final product. Vickers hardness measurement as a function of grain size revealed grain size dependence of hardness similar to Hall-Petch effect. Liquid phase sintering of ceramics leads to nanocrystalline superplastic ceramics where intergranular glassy phase promotes grain boundary sliding. In case of solid state sintering it is difficult to fabricate nanocrystalline ceramics since it requires higher temperature that leads to grain growth. Shinoda et al. have used 3.5% C and 1% B as additives in hot isostatic pressing of SiC to fabricate nanocrystalline SiC-B, C with an average grain size of 200 nm. Total percent elongation of about 140% was observed at 1800°C tensile experiment. This superplastic behavior was attributed to boron segregation at grain boundaries to promote grain boundary sliding [77].

I.3.4 Ultra high pressure sintering (UHP)

In ultra high pressure (UHP) sintering, applied pressure is in the range of 4 – 8 GPa [78–80]. Ultra high pressure allows lower sintering temperature and additive free dense bulk samples. Moreover, UHP sintering requires very short sintering time resulting in fine microstructure of the sintered compact. However, application very high pressure restricts its use in commercial application as complex geometry can not be sintered using this method.

Qian et al. sintered diamond-SiC composites using UHP method in the temperature range of 1400 – 2000°C with pressure ranging from 6 – 8 GPa [81]. Void free composites sintered in this work had superior properties compared to diamond-SiC composites prepared using liquid silicon infiltration technique. In another work, Gadzira et al. used fine silicon and natural graphite particles to produce SiC by self-propagating synthesis process [79]. 1400°C sintering temperature and 4 GPa pressure led to SiC-C solid solution composite with microhardnes of 40 GPa. However, raising the sintering temperature to 1600°C and pressure to 6 GPa disintegrated the SiC-C solid solution and decreased the microhardness to 29 GPa. In a similar work, Gadzira et al. obtained defect free β-SiC structure using UHP sintering [78]. Raman spectroscopy study indicated C-C sp^3 bonds which was attributed to the carbon antisites in the SiC structure. Formation of a SiC-C solid solution led to reduction of the β-SiC lattice parameter.

I.3.5 Spark plasma sintering (SPS)

Even though the techniques discussed above enable sintering of silicon carbide with binders to near theoretical density, use of binders affects mechanical properties of SiC. Binders affect its ability to maintain excellent mechanical properties at higher operating temperature as these additives segregate at the grain boundary and form a glassy secondary phase. This secondary phase softens at high temperature and significantly reduces mechanical strength of SiC. Moreover, most of these techniques provide no control over the microstructure of the compact being sintered. These shortcomings can be overcome using a novel sintering technique called spark plasma sintering (SPS). The SPS process involves simultaneous application of uniaxial pressure and pulsed current to the powder mixture placed in graphite dies. The schematics of the SPS process and associated mechanisms are presented in Fig I.6. The unique effects during SPS including, joule heating at the particle contacts and/or localized sparks at the gaps between particles cause localized surface heating and solid state sintering of the powder. Since the heating effects under the influence of electric current are localized at the powder surface, the SPS process allows sintering of the powder without significant grain growth [82]. This is a great advantage over conventional hot pressing where grain growth is unavoidable due to bulk heating of the samples. Furthermore, the surface activated mechanisms cause full densification with SPS within much shorter time (typically less than 20 minutes) and at significantly lower temperature ($<$2000 °C) compared to conventional hot pressing. With these unique effects, SPS processing is expected to initiate nanocrystallization and retain the nanostructured grain size in the bulk samples.

The sintering mechanism behind the SPS process is still not well understood. Especially, the formation of 'plasma' as proposed by Tokita is still neither proven nor discarded [10]. Recently, Hulbert et al. reported the absence of plasma during SPS pro-

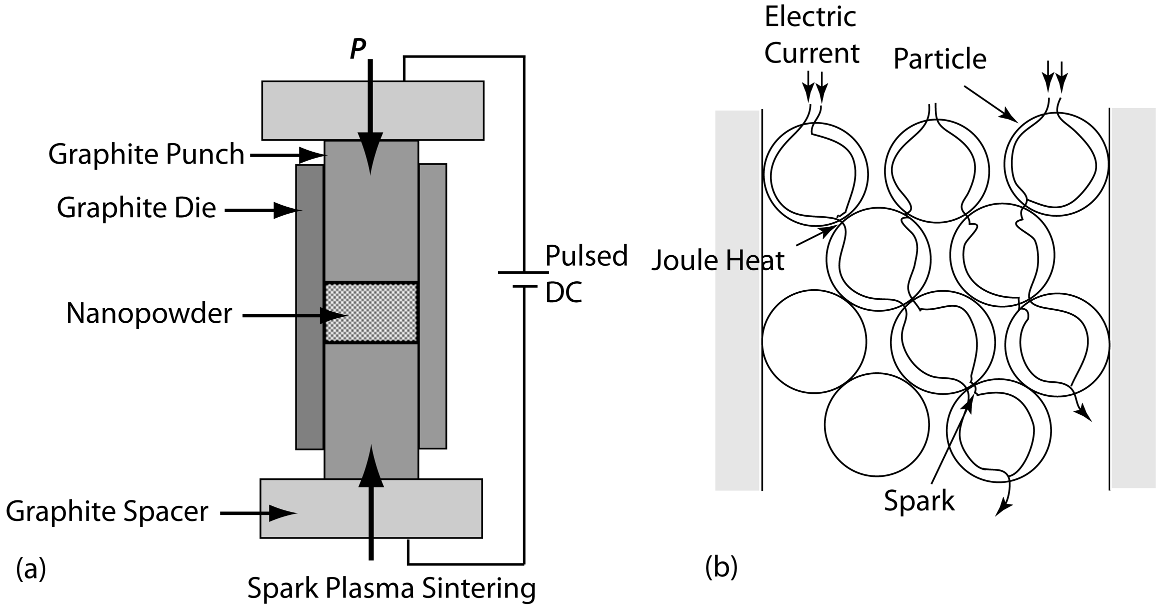

Figure I.6: Schematic of (a) Spark plasma sintering setup, (b) mechanisms of sintering [10].

cess [83, 84]. In that work, three different experimental techniques were used, namely, in situ atomic emission spectroscopy, direct visual observation, and ultrafast in situ voltage measurements to prove the absence of plasma. To support their claim, different materials were sintered using different sintering conditions. Even though the presence of plasma is debatable, it is generally accepted that the contact area of the particles reaches temperature above melting temperature of the material and leads to localized melting that favors inter-particle bonding. However, this overheating is a surface phenomena as the temperature gradient is very steep along the radius of the particle and does not affect the bulk sample as a whole [85]. Zhaohui et al. recently proposed four steps for the SPS process based on the microstructural evolution [86]. The first step is activation and refining of the powder. In this step, localized heating of the particles due to spark discharge activates the particles and surface oxide layer is removed by voltage breakdown effect. Next step is the formation and growth of the inter-particle neck. As the surface of the particles become activated spark discharge becomes stronger favoring mass transport by evaporation, condensation and diffusion leading to neck formation and neck growth. When all the particles are interconnected, spark discharge effect stops and joule heating becomes the main mode of heating and densification. That is the third step of SPS process. Finally, plastic deformation of the particles due to the applied pressure enhances densification and completes the SPS process.

One concern in SPS process is the measurement of the sample temperature during sintering [87]. Usually either a thermocouple placed inside a hole near the sample or an optical pyrometer is used to measure the sample temperature during SPS. Using a thermocouple gives temperature measurement close to the actual temperature of the sample. However, at higher sintering temperature use of thermocouple is difficult. Hence, pyrometric measurement is used for higher sintering temperature. During pyrometric measurement, the pyrometer is focused on the external surface of the die. This works well when the heating rate is very low that permits thermal equilibrium, but there is discrepancy in measured temperature when higher heating rate is used. Moreover, temperature distribution depends on the thermal conductivity of the sample and the die. The discrepancy in measured temperature can be as high as 100°C for higher sintering temperature with higher heating rates [88,89].

To avoid the negative effects of sintering additives, spark plasma sintering technique has recently been used to consolidate bulk SiC. Since very high heating rates (up to 600 °C/min) are achievable using SPS due to the passage of high amount of pulsed direct current through graphite dies and punches, grain growth during densification of nanostructured SiC can be inhibited due to exposure to high temperatures for very short time [82]. Yamamoto et al. used SPS to consolidate SiC powder prepared using mechanical alloying of commercially available Si and C powder [90]. Although dense SiC ceramics were prepared using this method, mechanical properties were lower compared to commercially available SiC powder consolidated with additives using SPS. More recently, Guillard et al. and Lara et al. have carried out parametric study to understand the effect of time, temperature and pressure on densification of SiC without the use of additives during SPS [91,92]. While temperature and pressure played a vital role in densification process, grain growth was found to be restricted to $\sim$ 100 nm with the use of higher pressure (150 MPa) at the same sintering temperature. Zhang et al. investigated the effect of granulation process on the microstructure and mechanical properties of SiC sintered using SPS [93]. Binderless granulation process resulting in 80 μm granules was considered the key factor in accelerating the densification process reaching a relative density of 98.5% at 1860°C. However, this process led to coarse-grained (2.05 μm) microstructure even at a sintering temperature of 1860°C. Lomello et al. used laser pyrolysis to prepare β-SiC nanopowders as initial powder for SPS [94]. Although use of this technique to prepare initial powder seems beneficial as the mean particle size was 16.6 nm, presence of 5 wt% oxygen and 1 wt% free carbon as a by-product in the initial powder hinders the densification process, more importantly, has detrimental grain coarsening effect.

I.4 Fillers used for SiC matrix

Even though SiC has excellent mechanical properties, its application has been limited due to lower fracture toughness of the material [21–23]. To induce crack resistance in SiC, fillers such as whiskers, particulate or carbon fibers have been studied over the years [11, 95–97]. Reinforcing SiC with carbon fibers not only overcome low toughness issue but also the high flaw sensitivity of monolithic SiC ceramics [11]. It has been reported that the interfacial bonding between carbon fiber and SiC dominates the mechanical properties of the composite [98]. Fiber debonding and pullouts mechanisms, which occur at the fiber-matrix interface when the interface is neither very strong nor weak, increases the toughness of carbon fiber reinforced SiC (Fig I.7) [11]. Various processing techniques such as Chemical Vapor Infiltration (CVI), Liquid Polymer Infiltration (LPI), and Melt Infiltration (MI) have been sued to fabricate SiC/C composites. However, these methods are often associated with high processing cost and time consuming. Furthermore, oxidation of carbon fiber during processing is detrimental to properties of the composite. As an alternative, short carbon fiber reinforced SiC composite have been fabricated due to its ease of processability using spark plasma sintering . However, sintering additives have been used during sintering

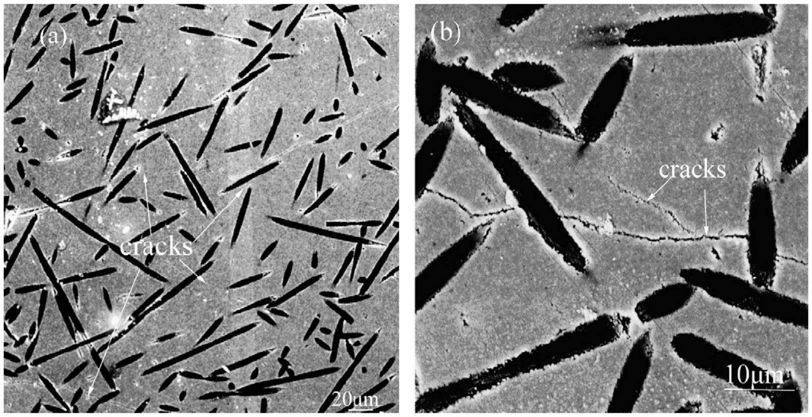

Figure I.7: SEM image of polished surface of the short carbon fiber reinforced SiC composites at 1650°C and 25 MPa [11].

process in order to aid densification [11, 95]. Similar studies on carbon-fiber reinforced SiC is also studied by Tang *et al.* where volume percentage of C fiber was varied and the composite was processed using hot pressing [97]. Even tough carbon fiber-SiC composites have been well studied for quite some time now, none of these studies reported significant improvement in fracture toughness for SiC ceramics. Note that the SiC ceramic matrices in most of these investigations had micro-grained structure (grain size significantly greater than 100 nm) with diameters of carbon fibers in the range of 5-25 μm.

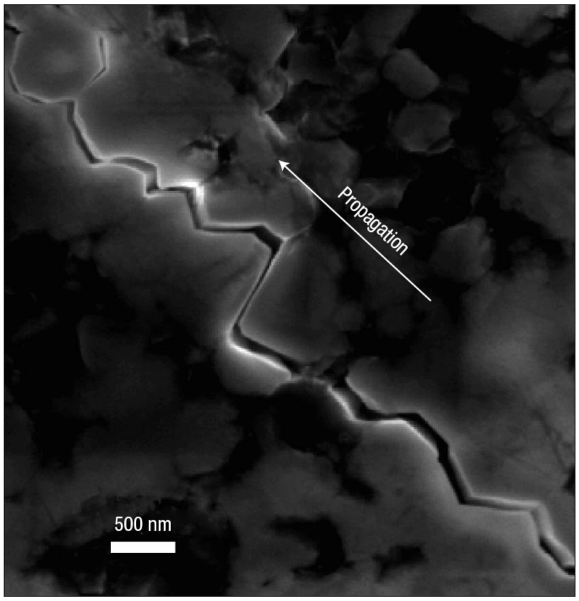

Figure I.8: SEM image of Intergranular crack growth in a 5.7 vol % SWCN Al_2O_3 nanocomposite [12].

Recently, carbon nanotubes (CNTs) are attracting significant attention as potential toughening agents in micro-grained ceramics due to its excellent properties, such as low density, high aspect ratio (1000-10000), tensile strength (150 GPa), and an elastic modulus of 1 TPa [28]. Initial investigations on toughness of CNT/ceramic composites indicated little or no improvement in fracture toughness due to difficulties such as dispersion of CNT in matrix, and methods used for determining fracture toughness that failed to uncover the actual failure mechanism. Zhan *et al.* have observed three fold increase in fracture toughness for 10vol% CNT-Al_2O_3 compared to pure alumina [12]. Toughening of SWCNT reinforced Al_2O_3 is clearly seen in Fig I.8 below, where mode of failure is intergranular [28]. Recently, CNT reinforced ceramics composites were processed using powder metallurgy routes where dispersion of CNT in the matrix were achieved by ball milling using high energy ball mills. It should be noted that conventional hot pressing was avoided while compacting these materials as hot pressing might damage CNTs and degrade their properties [12]. It was observed that conventional sintering techniques like hot pressing were not helpful in compacting these composites as sintering this composites at higher temperatures for longer time results in damaging of CNTs. Furthermore, the higher temperatures associated with hot pressing can result in detrimental β-SiC to α-SiC phase transformations of the matrix. In a recent investigation, Ma *et al.* reported only incremental (10%) increase in toughness for CNT reinforced SiC composites processed using conventional hot pressing [26]. While significant progress has been made towards using chemical, mechanical, and ultrasonic methods to enhance the dispersion of the CNTs in various matrices, the non-uniform distribution of CNTs is still a serious issue. High quality carbon nanotubes dispersed effectively in the ceramic matrix is very essential in order to carry loads and transfer stress which results in toughening of the ceramic.

It can be seen from the aforementioned review that nano-fillers play an important role in determining the mechanical and functional properties of ceramics. Hence selection of proper nano-filler and its dispersion dominates the changes that are to be expected from the resultant compositse.

I.5 Graphene

Graphene is a one atom thick 2-D layer of sp^2 carbon arranged in a honeycomb lattice [13, 44]. It is considered the building block of different forms of carbon such as fullerene, carbon nanotube and graphite. While fullerene and carbon nanotube can be visualized as graphene rolled into spherical and cylindrical shape, graphite is basically graphene sheets stacked together to form a 3-D structure (fig. I.9). In graphene, each carbon atom forms bonds with its 3 nearest neighbors in the hexagonal structure. 3 valence electrons are responsible for these 3 σ bonds between the atoms. These covalent bonds give graphene its unique mechanical and thermal properties. The remaining valence electron forms the π band perpendicularly oriented to the molecular plane and dominates the planar conduction [99]. Graphene existed as a theoretical material for many years [99]. Earlier it was

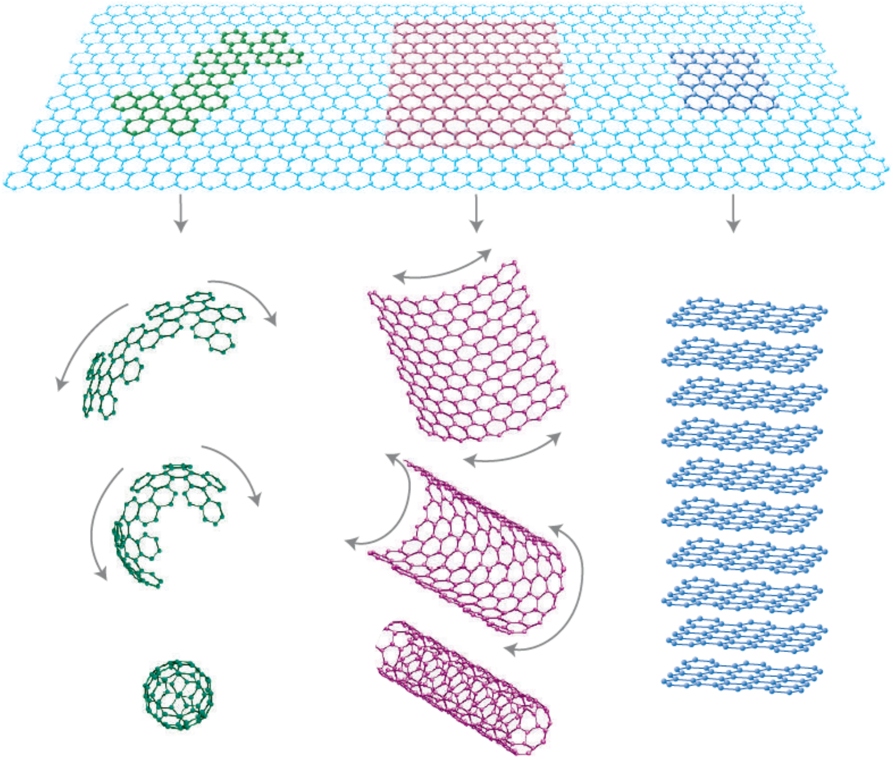

Figure I.9: Graphene as a building block for fullerene, CNT and graphite [13].

considered that 2 dimensional material would be thermodynamically unstable and could not exist [100, 101] until it was produced by a simple mechanical exfoliation method by Geim's group in 2004 [102].

I.5.1 Graphene synthesis

After Geim's group produced single layer graphene, there have been many reports of different methods of producing graphene. Geim's group produced graphene by mechanical exfoliation of highly oriented pyrolytic graphite (HOPG) using a scotch tape. It is a peeling process where HOPG was dry etched in oxygen plasma to make 5 μm deep mesa that were stuck on to the photoresist and peeled off by scotch tape. Thin flakes were then washed in acetone and transferred to silicon substrate that were single or multiple layer graphene flakes. Although this method is easy and repeatable, it is inefficient for large-scale commercial production of graphene sheets. Exfoliation of graphite in liquid phase has also been proposed by several research groups. Stankovich et al. used ultrasonication of graphite oxide and exfoliated graphite oxide nanosheet in aqueous suspension followed by reduction using hydrazine hydrate at 100°C for 24 hour [103]. However, oxygen was left in the structure resulting in partially reduced exfoliated nano-graphite oxide sheet. In a similar approach, Hernandez et al. and Lotya et al. separately used ultrasonication of graphite in N-methyl-pyrrolidone and sodium dodecylbenzene sulfonate respectively to produce single and few layer graphene [104, 105]. This method seems to be promising for large scale production of graphene. One concern using the liquid exfoliation is the defects created in the graphene sheets during ultrasonication. Another method used for production of graphene layers is thermal decomposition of SiC and is of interest in the semiconductor industry. This method involves heating SiC to high temperature between 1000°C to 1500°C in ultra-high vacuum and sublimate Si from the structure. This leaves a carbon rich layer on the surface [106]. Few layer graphene has been produced by thermal decomposition of SiC. It required preparation of the Si face of 6H-SiC single crystal by oxidation first, followed by electron bombardment in ultra-high vacuum to 1000°C for removal of oxide layer. Finally, heating the samples to 1250–1450°C produced few layer graphene that had mobilities of $1100\text{cm}^2\text{V}^{-1}\text{s}^{-1}$ [107]. Even though this method is successful in producing high quality graphene layers, controlling the number of layers and effect of SiC interface in the produced film are still some concern. Chemical vapor deposition (CVD) growth of graphene on substrate is another promising method for preparing high quality single and few layer graphene. Somani et al. were the first to report producing few layer graphene films on Ni foil using camphor utilizing CVD process [108]. Advantages of this method includes production of high quality graphene and ability to transfer the film to any other substrate by etching the metal substrate. For metal substrates with high carbon solubility ($>$ 0.1 atomic %) such as Co or Ni, the carbon is dissolved into the substrate at growth temperature and subsequently precipitated on the substrate by faster cooling to form few layer graphene films [109]. Metal substrates with low carbon solubility like Cu requires a sequence of steps to grow graphene film [110]. First, exposure of methane and hydrogen to Cu forms C_xH_y on the surface and depending on the temperature, methane flow, methane pressure and hydrogen partial pressure the surface can be undersaturated, saturated or supersatu-

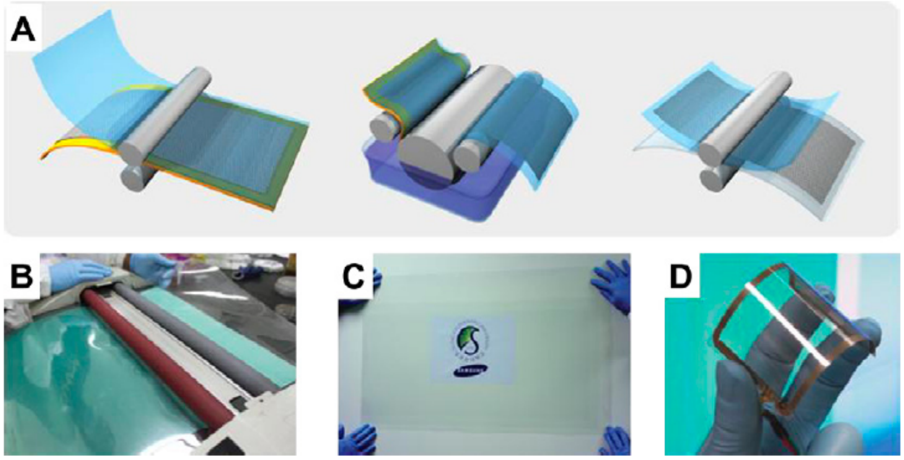

Figure I.10: Graphene film produced by Bae et al. using CVD process, (A) Schematic of graphene film grown on copper foil and transferred to another substrate, (B) Roll-to-roll transfer process, (C) Transparent large graphene film on PET sheet, and (D) Flexibility of graphene/PET sheet [14].

rated. These C_xH_y species on supersaturated Cu surface forms nuclei and grows to form graphene island. Process temperature, methane flow rate and partial pressure of methane dictates how well the graphene islands cover the Cu substrate. In a recent report, Bae et al. demonstrated roll-to-roll production of ultra-large (30 inch) graphene film using CVD method [14]. This process gained a lot of attraction as graphene film was grown on Cu substrate and transferred to a target substrate without loosing important properties or inducing ripples in the film. Briefly, their process includes, adhesion of polymer support to the graphene film on Cu foil, chemical etching of the Cu foil and finally transferring the graphene film onto a new substrate (PET) as shown in fig. I.10.

Apart from the methods described here, there are few other methods that have been used to produce single or few layer graphene such as molecular beam deposition or unzipping carbon nanotubes [111,112]. Molecular beam deposition was used recently to form several layers of graphene on Ni substrate. Thermal cracker was used to break down ethylene gas at 1200°C and C was deposited on Ni substrate at 800°C. The difference between this method and CVD is, carbon is not absorbed into the substrate before forming graphene films on the substrate. Unzipping of multiwalled carbon nanotube (MWCNT) has been also shown form graphene sheets. In this method, MWCNTs were suspended in H_2SO_4 and treated with $KMnO_4$ to produce oxidized graphene nanoribbons that were subsequently reduced chemically. Using this method, however, deteriorate electrical properties of the graphene sheet.

I.5.2 Properties of graphene

Graphene or few layer of graphene possess a combination of unique set of electrical, optical, and mechanical properties. Especially, these properties provide a way to overcome the shortcomings of other materials that are currently being used or worked on. So far, graphene has been studied for its electronic properties exhaustively. At room temperature, graphene with high electron mobility of 2000 $cm^2V^{-1}s^{-1}$ allows for unusual quantum Hall effect (QHE) for both electrons and holes [113, 114]. Morevoer, high mobility, and sensitivity to field effect made graphene to be an alternative to carbon nanotubes for field-effect transistors [115]. Graphene mobility can be enhanced by removal of the substrate. In case of suspended graphene mobility exceeds 200,000 $cm^2V^{-1}s^{-1}$ which is larger than reported for any other semiconductor or semi-metal. Another interesting property of graphene is its linear dispersion curve near the Dirac point. This has prompted observation of different quantum electrodynamic properties. However, devices such as sensors or transistors require non-linear effects for amplification of signals. Unfortunately, as a zero band gap semiconductor graphene can not be used for fabrication of such devices. Several attempts have been made to create a band gap in graphene for device fabrication. By including defects in the form of sp^3 hydrocarbon in sp^2 lattice or by distorting sp^2 lattice under uniaxial strain a gap can be induced in graphene. Another way of inducing bandgap is to carve graphene into a ribbon-shape. The gap varies with the width of the nano-ribbons.

Graphene has $\sim$98% transmittance property that makes it highly transparent to light [115]. Combined with electrical properties, this optical property paves the way for new applications of graphene in optoelectronics and photonics. Transparency of graphene film decreases linearly with film thickness or number of layers. Even with 10 nm thickness the transmittance is 70% for graphene layers. Indium tin oxide (ITO) is used a standard material as transparent electrodes. It has 40Ω/sq sheet resistance and 80% transparency. Graphene with a higher transmittance and lower resistance can be used as a transparent electrode for solar cells if low cost production of graphene is possible by chemical exfoliation.

In electronic devices, dissipation of heat during usage is an important factor for better performance and longevity. As graphene is considered for electronic devices, it is no surprise that thermal conductivity of graphene is also a matter of interest for the scientific community. In the past, allotropes of carbon like graphite, diamond or carbon nanotube (CNT) have shown high thermal conductivity due to the covalent bonding between C atoms

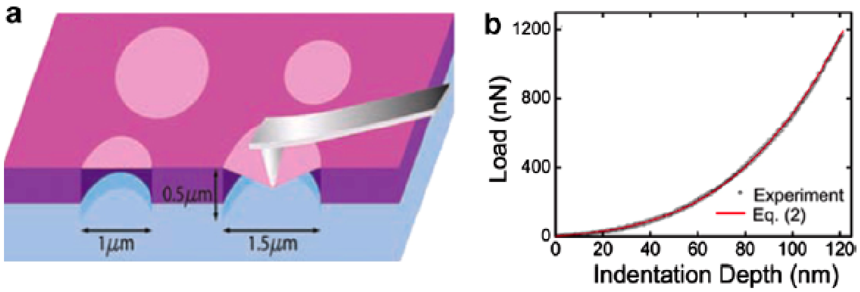

Figure I.11: Mechanical properties of graphene. (a) Schematic representation of AFM indentation on suspended graphene. (b) experimental and simulated (red line) loading/unloading curve for AFM indentation of graphene [15].

and phonon scattering. Both CNT and MWCNT are shown to have thermal conductivity of ∼3000–3500 W/mK at room temperature [116, 117]. Nonetheless, high thermal contact resistance still dominates CNTs usage in devices. Recent thermal conductivity measurement of pure defect free graphene has shown that graphene can have the highest room temperature thermal conductivity of 5000 W/mK. This only applies for free standing graphene sheet. However, use of substrate reduces thermal conductivity to 600 W/mK [118]. Moreover, edge scattering and isotopic doping have detrimental effect on thermal conductivity of graphene.

Mechanical properties of graphene has been much less investigated compared to its electronic and optical properties until recently. Like other allotropes of carbon (CNT), graphene also possess excellent mechanical properties. Recent investigation of suspended graphene sheet using AFM nanoindentation by Lee et al. revealed that graphene is the strongest material ever measured with elastic stiffness of ∼340 N/m and breaking strength of ∼42 N/m [15]. These values translates to 1.0 TPa Young's modulus and 130 GPa intrinsic strength for bulk graphite. Moreover, graphene can sustain more than 20% local strain before fracture. Fig. I.11 illustrates the method used by Lee et al. for measuring mechanical response of suspended graphene. In a separate study, it was shown that intrinsic strength of graphene film reduces slightly as the number layers is increased from single (130 GPa) layer to 3 layers (101 GPa) [119].

I.5.3 Graphene nanocomposites

As described above, the properties of graphene, such as Young's modulus of 1TPa and ultimate strength of 130 GPa, make it one of the strongest materials available [15, 44, 45]. Moreover, graphene is considered to have super-electrical properties and very high thermal properties [44, 120]. Furthermore, graphene is expected to be 500 times less expensive compared to carbon nanotubes and it does not have the stringent dispersion and alignment requirement for using in composites [121]. One of the possible ways to utilize these unique properties of graphene is to use it as nanofillers in polymer nanocomposites. Unlike conventional polymer composites only a small volume of graphene is required for enhancement of properties. Due to the aforementioned attributes of graphene significant research interest has been attracted towards graphene reinforced polymer nanocomposites [44, 120–129]. Yasmin and coworker reported 25% increase in elastic modulus for 5-wt% graphite platelet reinforcement and 21% increase in tensile strength for 2.5-wt% graphene in epoxy matrix [121]. This increase in strength and modulus was attributed to high aspect ratio of graphite platelet along with better interfacial adhesion between epoxy and graphene. Ramanathan et al. used 0.05 wt% functionalized graphene sheets (FGS) as nanofiller in poly(methyl methacrylate) to observe remarkable 30 C improvement in glass transition temperature. Moreover, 33% increase in elastic modulus for only 0.01 wt% of FGS reinforcement was reported [122]. Wakabayashi et al. used solid state shear pulverization to make graphite polypropylene (PP) composite [130]. Addition of 2.5 wt% graphite lead to 100% increase in Young's modulus and 60% increase in yield strength compared to neat PP. Using melt mixing polymer solution and coating Kalaitzidou et al. prepared polypropylene-exfoliated graphene composites [125]. Coating method was found to be more effective than solution method for improvement of flexural strength up to 30% and flexural modulus up to 167% at 10vol%.

It is evident that the graphene/polymer nanocomposite system is well studied for quite some time now. However, graphene/ceramic composite system has not been well stud-

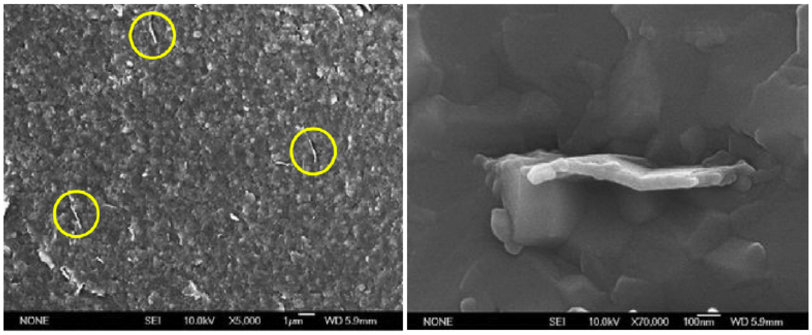

Figure I.12: SEM images of fractured surfaces of Al_2O_3 with 1 vol % graphene nanosheets [16].

ied till now. Most of the studies published so far indicates the possibility of improvement in properties due to addition of graphene in ceramic matrix. It has been reported that graphene nanosheet reinforced Al_2O_3 showed a percolation threshold of 3 vol%, however, for 15 vol% graphene nanosheet reinforcement electrical conductivity was increased to 5709 S/m which is 170% higher while compared with the result available for CNT reinforced Al_2O_3 [16]. This improvement in electrical conductivity was attributed to network like structure of graphene in the composite (Figure I.12). It was also observed that graphene nanosheet restrained grain growth of Al_2O_3 in the composite during spark plasma sintering process [131]. Excellent improvement (53%) in fracture toughness of alumina by graphene reinforcement has also been observed by Wang et al. [131]. This improvement in fracture toughness was mainly due to crack bridging and nanosheet pulling out. Liu et al. reported toughening of a multi-component system of ZrO_2-Al_2O_3 by graphene nanoplatelet [132]. Addition of graphene platelet increased fracture toughness by 40% by various extrinsic toughening mechanisms. Walker et al. reported a remarkable 235% increase in fracture toughness of Si_3N_4 by only addition of 1.5vol% [133]. This increase in fracture toughness was attributed to proper processing of the composite and a new toughening mechanism (out of plane crack deflection) that was observed for these composites. In their work, dispersion of the graphene was achieved by colloidal processing and compaction was obtained by spark plasma sintering. Recently, graphene-Si_3N_4 system has also been studied for tribological properties [134]. It was found that at lower wt% addition graphene bonds strongly to the matrix and does not provide any wear resistance. However, 3wt% graphene addition reduced wear rate by 60% compared to monolithic Si_3N_4.

In most of these investigations, the ceramic matrix used had starting grain size in the range of 100 nm-1μm (grain size after sintering was often not reported). These are very preliminary reports and significant understanding about the densification behavior, structure of ceramic-graphene interface, toughening mechanisms, and thermo/mechanical stability of the graphene needs to be reached. Furthermore, there is significant potential to further improve the properties by controlled nanostructuring ($<$500 nm grain size) of the ceramic matrices.

CHAPTER II

Obejctive

As discussed earlier, in spite of its unique set of properties, the application of SiC is limited due to its inherent brittle nature and low fracture toughness. One of the most effective ways to improve toughness is to reinforce the parent material with filler material to provide extrinsic toughening mechanisms. Including filler materials in ceramic matrix poses some fundamental challenges, for instance, uniform dispersion of the filler in the ceramic matrix and survival of the filler material during harsh processing required for dense bulk ceramic. While various dispersion techniques have been employed, improvement in toughness has been limited so far. Moreover, commonly used filler materials such as carbon fiber or CNT have shown degradation under ceramic processing conditions. Therefore, there is a need to employ a processing technique to include a proper filler materials in ceramic matrix to understand the real potential of extrinsic toughening in SiC matrix.

The ultimate goal of this work is to process dense bulk fine grained SiC matrix reinforced with graphene nanoplatelets to provide toughening to the host matrix. This requires setting up a proper processing parameters for preparing bulk dense SiC first and later, uniform dispersion of graphene nanoplatelets in the SiC matrix without thermal damage. As discussed in the previous chapter, processing and characterization of SiC has long been studied and well documented. Especially, after the introduction of binders in 1970, there has been a drive to sinter bulk dense ceramic with better mechanical properties. Different processing routes have been explored and studied. All these processing routes require additives for bulk dense ceramic. However, sintering with additives affects mechanical properties at high temperature. Since SiC is touted to be used in high temperature environment, use of additives becomes an issue in that respect. Without binders it is possible to sinter SiC to dense forms using high temperature and pressure for longer times using conventional methods. This processing, however, leads to grain coarsening that in turn affects mechanical properties. To be able to sinter SiC without binders requires a processing that will not only lead to dense bulk form but also restrict exaggerated grain growth. Spark plasma sintering (SPS) is one such processing technique that can lead to dense bulk SiC without significant grain growth. Until now, there have been very few studies that involve sintering of SiC using SPS without additives. Moreover, it should be taken into account that even before bulk processing, the final microstructure will depend on the initial microstructure of the powder that is being used for bulk processing. Hence it is certainly equally important to produce SiC powder with desired initial microstructure. Polymer precursor route provides the ability to produce high purity SiC with desired microstructure.

Considering the requirements mentioned above, in this work a novel approach, combining polymer precursor processing and spark plasma sintering (SPS), is presented to process nanostructured silicon carbide ceramic. Polymer to ceramic conversion is studied using Fourier transform infrared (FTIR) spectroscopy. To optimize processing parameters amorphous/nanocrystalline powder is SPS sintered at different temperatures ranging from 1600°C to 2100°C under 70 MPa pressure and different soaking time. Effect of processing parameters on densification and microstructural evolution are analyzed. Mechanical properties obtained using different experimental techniques are correlated with microstructure of SiC sintered at different temperatures.

In this study, commercially available powder is also consolidated using SPS with or without additives. These samples are only sintered at 2100°C and evolution of microstructure is analyzed. Mechanical properties determined using microhardness, bi-axial flexure test are compared with samples sintered using pyrolyzed powder. Differences in mechanical properties are explained with respect to microstructure of the respective materials. Commercially available conventionally sintered samples are also acquired and tested. These results are also compared with samples sintered using current method and analyzed.

Finally, graphene reinforced SiC matrix is fabricated using polymer pyrolysis and SPS. Thermodynamic calculation confirmed allylhydridopolycarbosilane (AHPCS) to be a proper dispersion medium for graphene nanoplatelets. Addition of graphene does not hinder the polymer to ceramic conversion as ensured by FTIR study. As processing condition can damage graphene nanoplatelets, it is critically important to study the survival of graphene nanoplatelets. There have been some reports on thermal stability of graphene [135, 136]. Suspended graphene sheet heated using Joule heating showed thermal stability even at 2600 K temperature as reported by Kim et al. [135]. However, sintering is a more complex process, as the powder is compacted under the simultaneous application of temperature and pressure. In that respect, detailed Raman spectroscopy study is performed to understand the complex effect of sintering temperature and pressure on graphene nanoplatelets embedded in the SiC matrix. Effect of graphene addition is studied on densification behavior and phase evolution of the SiC matrix. Mechanical properties with respect to graphene content are studied and detail analysis of change in mechanical properties due to graphene addition is presented.

CHAPTER III

Experimental Details

III.1 Powder preparation

III.1.1 Monolithic SiC powder

As a first step amorphous–nanocrystalline SiC powder was prepared from a preceramic polymer, allylhydridopolycarbosilane (AHPCS) (Starfire Systems Inc., Malta, NY). The powder preparation process was started by heating the liquid polymer precursor to 650 °C, at 1 °C/min, under an inert atmosphere and then holding it at 650 °C for 10 minutes . This initiated the cross-linking of the polymer precursor. For complete conversion to amorphous–nanocrystalline SiC, the heating was continued till 1400°C, at 3°C/min. The material was held at the final temperature for 1 hour to ensure thermal equilibrium and complete processing. Finally, the material was cooled down to room temperature, at 5

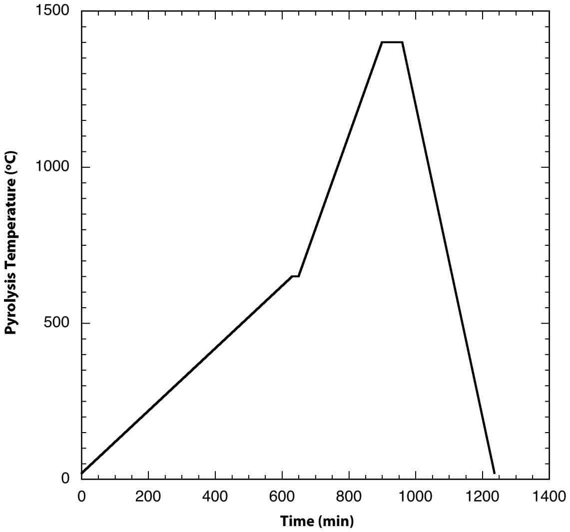

Figure III.1: Schematic of heating cycle used for pyrolysis.

°C/min. Figure III.1 shows the heating cycle used for pyrolysis of all the powder at a final temperature of 1400°C.

Due to the release of hydrogen gas during the polymer to ceramic conversion, the final material contained large voids. This material was ground using a hand grinder until the particles passed through a colander of mesh size 12 followed by subsequent milling into fine powder ($\sim$0.5μm) using a high energy ball mill (Pulverisette, Fritsch GmbH). Ball milling was performed using a ball-to-powder mass ratio of 5:1 with tungsten carbide (WC) balls as grinding media for 15 minutes with 750 rpm. Note that the starting powder was amorphous and the purpose of milling is to decrease the particle size without inducing any phase transformation. The amorphous/nanocrystalline powder was subsequently used in spark plasma sintering for processing nanostructured SiC.

For comparison commercially available superfine SiC powder (Alfa Aesar A13561) was also used. This powder was also ball milled using the same parameters mentioned above.

III.1.2 Graphene-SiC powder

Graphene nanoplatelets

Exfoliated graphene nanoplatelets, xGnP $^{®}$-M-5 grade (99.5% carbon) with an average diameter of 5 μm were obtained in dry powder from XG Sciences, Inc. (East Lansing, MI). These nanoplatelets are prepared from graphite intercalated compounds (GIC). GICs are prepared using nitric acid as oxidizer and sulfuric acid as intercalant. Rapid heating to high temperature leads to vaporization of the acids and forces the layers to expand resulting in exfoliation of graphite layers. GICs are processed using microwave at 1300W for 2 minutes that exfoliates the graphite layers. Moreover, microwave treatment removes residual intercalant (nitrogen and sulfur) components [137]. Fig. III.2 shows platelet size of the as-received xGnP platelets. According to manufacturer, the average thickness of the particles is 6–8 nm with typical surface area of 120 – 150 m^2/g [138].

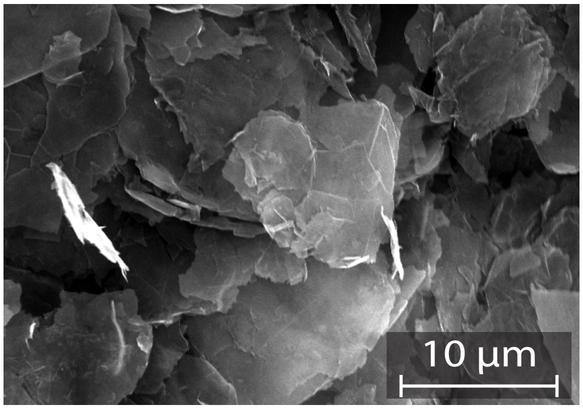

Figure III.2: As received xGnP platelets.

Pyrolysis of graphene-AHPCS

Two sets of powder were prepared for this study. For preparing SiC-graphene powder mixture, controlled weight fraction (2wt% and 5wt%) of graphene nanoplatelets was mixed with AHPCS polymer and ball milled using a planetary ball mill (PM-100, Retsch GmbH, Haan, Germany) for 30 minutes. Ball milling was performed using a ball-to-powder mass ratio of 10:1 with tungsten carbide (WC) balls as grinding media for 30 minutes with 300 rpm. Subsequently, this mixture was pyrolyzed using the similar procedure mentioned earlier. The pyrolyzed amorphous/nanocrystalline SiC reinforced with graphene nanoplatelets was carefully milled using parameters mentioned earlier such that uniform mixture without significant damage of graphene nanoplatelets can be achieved. It has been reported that controlled ball mill can aid in exfoliation of graphene nanoplates due to shear component of the applied stress [139]. SiC-graphene composite powder mixtures with varying levels of graphene reinforcements (0-5 wt.%) was prepared for subsequent SPS densification.

Another set of powder was prepared for comparison. In this case, AHPCS was pyrolyzed first to prepare SiC powder. Then, 2wt% and 5wt% graphene nanoplatelets were mixed with SiC powder (prepared from AHPCS) and ball milled in isopropanol as dispersing media using the parameters mentioned previously. For ease of identification, the first set of powder will be referred as AHPCS-2wt%C, AHPCS-5wt%C and the second set of powder will be referred as SiC-2wt%C, SiC-5wt%C. Note that these are essentially

SiC-graphene composite powder prepared in different way.

III.2 Sintering parameters

Spark plasma sintering (SPS) was used to consolidate nanostructured SiC obtained through pyrolysis of preceramic precursor using an SPS system (Model 10-3, Thermal Technology, LLC., Santa Rosa, California, USA). The DC pulse cycle for the system was 25 ms on and 5 ms off. The ball milled SiC powder was loaded in graphite die with an internal diameter of 20 mm and 10 mm of wall thickness. Graphite felt with a thickness of 4 mm was wrapped around the graphite die to avoid thermal loss during sintering. Temperature of the sample was monitored during sintering using an optical pyrometer through a hole of 2 mm diameter and 5 mm depth in the graphite die. Samples were sintered at various temperatures ranging from 1600 °C to 2100 °C, using a heating rate of 150 °C/min under argon atmosphere. Sintering pressure of 70 MPa and a soak time of 10 minutes were employed for all the samples. The schematic of the different steps involved in the processing is shown in Fig III.3.

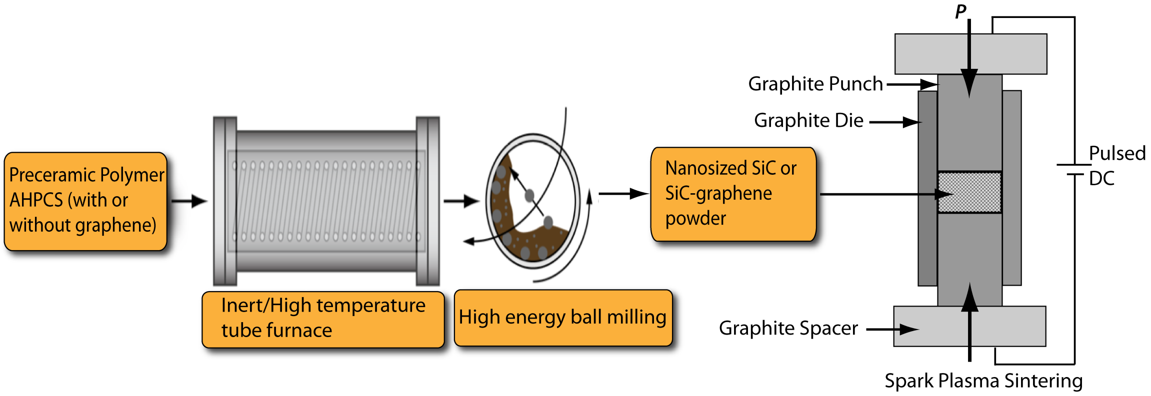

Figure III.3: Schematic of the fabrication process

Commercial SiC powder was also sintered using a temperature of 2100°C and pressure of 70 MPa with 10 min soak time. Since the commercial powder was difficult to consolidate, 5 wt% Al_2O_3 as binder was added to commercial SiC powder to consolidate using the same sintering parameters. Samples sintered using commercial powder would be referred as commercial SiC and samples sintered using commercial SiC powder with binder would be referred as commercial SiC-Al_2O_3 throughout the text.

SiC-graphene composite powder mixture was also sintered using 2000°C and 2100°C sintering temperature with 70 MPa uniaxial pressure and 10 min soaking time.

III.3 Physical characterization

III.3.1 Density measurement

Density of a material can be defined in different ways based on the measurement process used. Bulk density of a material refers to the density of the material without taking open and closed porosity into account. While skeletal density takes only open porosity into account, solid density takes both open and closed porosity into account. The density and porosity of the SPS sintered SiC and SiC-C samples for different processing temperatures was determined.

The buoyancy method [140] was used for determining bulk density and porosity of the samples using a density measurement kit along with a high-resolution analytical balance. For this method, the sample is evacuated and saturated with high purity distilled water and the open pores are filled with the saturation liquid. This is done using a four-hour evacuation cycle with intermittent purging at every hour to release trapped air. The mass of the sample in saturation liquid (water), m_2 , is determined using the density determination kit. The temperature of the saturation liquid is recorded to correct the density variation of water as a function of temperature. The wet mass, m_3 , of the sample is then determined by weighing in air. Before weighing, a lint-free cleaning tissue is used to remove any liquid that remained on the surface of the sample and this is done quickly to avoid loss of the saturation liquid due to evaporation. Finally, the sample is then dried in a drying oven set at 120°C for 12 hours and cooled to room temperature to remove the saturation liquid from the sample and the dry mass, m_1, is recorded. The bulk density, ρ_b , is calculated as,

$$\rho_b = \frac{m_1}{m_3 - m_2} \times \rho_{fl} \tag{III.1}$$

Where, m_1 is the mass of the sample in air, m_2 is the mass of the saturated sample in the fluid medium (water), m_3 is the mass of the saturated sample in air and ρ_{fl} is density of the medium used (water) at the recorded temperature to correct for variation in density of water at different temperature.

The open porosity, π_a , in volume $\%$ is calculated as,

$$\pi_a = \frac{m_3 - m_1}{m_3 - m_2} \times 100 \tag{III.2}$$

III.3.2 Fourier transform infrared (FTIR) spectroscopy

Infrared(IR) spectroscopy is used to analyze presence of chemical groups in a compound by measuring the absorption of infrared light over a range of wavelength. Absorption of infrared radiation does not change electronic state of the molecule, rather it causes vibrational and rotational changes in the molecule. The vibrational frequency of the molecules dictates the absorption frequency. On the other hand, the absorption intensity is solely dependent on the infrared photon energy transferred to the molecule. This in turn depends on the change in dipole moments. Molecular vibration causes change in dipole moments. As a result, molecule selectively absorb infrared based on the change in the dipole moment caused by absorption [141]. The absorption is measured as a function of frequency. At each vibrational transition the molecule absorb $\Delta E = h\nu$ energy. The Beer-Lambert law defines the intensity of the IR absorption:

$$I = I_0 e^{-\epsilon c d} \tag{III.3}$$

Here, I_0 and I refer to the incident and transmitted beams, respectively, ϵ refers to the molecular absorption coefficient, and c is the concentration of the sample and d is the concentration of the cell length. For quantitative analysis, the absorption is defined as,

$$A = \log \frac{I_0}{I} = \epsilon c d \tag{III.4}$$

The absorption is collected as an associated spectrum over a wide range of wavelengths by FTIR spectrometer. In the current investigation, FTIR was performed to study the polymer-to-ceramic conversion on the as received AHPCS polymer and heat treated polymer at different temperatures of 350, 650, 900, 1150, and 1400°C using pellets made from the mixture of the solids and dried KBr powder using Varian 680 IR spectrometer with 4 cm^{-1} resolution. Similar procedure was followed to study the behavior of the polymer during pyrolysis after addition of graphene nanoplatelets.

III.4 Microstructure characterization

III.4.1 X-ray diffraction

X-ray diffraction method is a conventional technique used for phase detection, grain size measurement, residual stress measurement and compositional analysis. Diffraction is a scattering process, wherein a sample is irradiated with x-ray and the atoms depending on their arrangement may elastically scatter the x-ray giving weak or strong intensity. When atoms are arranged periodically in a material, the scattering is strong giving rise to Bragg's peak according the equation III.5 [142].

$$\lambda = 2d \sin\theta \tag{III.5}$$

Where, λ is wavelength of the radiation, d is interplanar spacing and θ is diffraction angle. Since, λ and θ are recorded during an x-ray diffraction experiment d-spaing can be calculated using Bragg's law. Peak width provides information related to crystal size in a material. For very small crystals, grain size could be measured using Scherer formula as shown in eqn III.6 [142].

$$D = \frac{K\lambda}{\left(W_{FWHM} \times \frac{\pi}{180^\circ}\right)\cos\theta} \tag{III.6}$$

Where D is the particle or crystal dimension normal to the diffracting planes, W_{FWHM} is the full-width at half-maximum, K is a constant usually evaluated as 0.94, λ is the wavelength of the x-ray used, and θ is the diffraction angle. However, this equation does not take instrument broadening into account and would give a minimum grain estimate. Moreover, for larger crystals the effect of instrument broadening would be greater as the width of the peak is already small. To account for instrument broadening a full pattern analysis can be performed using fundamental parameters approach [143]. In this method, the observed profile, $I(2\phi)$ is considered as a convolution of the diffraction profile, $S(2\phi)$ and the instrumental aberration function, $A(2\phi)$.

$$I(2\phi) = \int_{-\infty}^{+\infty} S(2\zeta)A(2\phi - 2\zeta)d2\zeta = S * A \tag{III.7}$$

Again, instrumental aberration funciton $A(2\phi)$ is the convolution of emission profile $L(2\phi)$ radiated from the x-ray target, and functions related to the instrument profile such as the length of the receiving slit, radius of the diffractometer, angular width of the divergence etc. That is

$$A(2\phi) = L * D_1 * D_2 * ..... * D_n \tag{III.8}$$

It is difficult to develop analytical form for $A(2\phi)$, hence the convolution integral is reduced to a summation in which the step size is the same as the x-ray data. In this case, the function is considered linear between adjacent calculated points. Finally, multilinear regression is used to determine all the linear terms whereas Gauss-Newton iteration is used to determine the non-linear terms.

Significant efforts of this work was directed towards understanding the nanocrystallization and densification behavior of amorphous SiC during SPS. Detailed XRD studies was performed on SPS sintered SiC and SiC-graphene samples. Graphene nanoplatelets pyrolyzed to different temperatures ranging from 750°C–1400°C was also analyzed with XRD to observe any shift in peak. For the current study, phase analysis of the sintered compacts was performed using Philips Norelco X-ray diffractometer operating with Cu Kα (λ= 1.54178 Å) radiation at 45 kV and 40 mA. The diffraction angle was varied between 10° and 90° 2θ at a step increment of 0.02° 2θ with a count time of 1 s. Profile refinement was performed using XFIT program using the Fundamental Parameters (FP) approach and grain sizes were estimated.

III.4.2 Scanning electron microscopy (SEM)

Scanning electron microscope (SEM) uses high energy electron beam to capture image of a sample surface. The electron beam is demagnified by two or three electromagnetic condenser lenses and later collimated into a fine probe by scanning coil to scan the surface in a raster. To maximize the mean free electron path, SEM requires high vacuum for operation. When the primary electron beam interacts with the solid they are scattered both elastically and inelastically to produce secondary electrons (SE), backscattered electrons (BSE), Auger electrons and x-rays [144]. As the primary electron interacts with the valence electron of the solid, some of the energy of the primary beam is used to get the valence electrons free from the atom and these electrons are termed as secondary electrons (SE). Most of these electrons have initial kinetic energy $<$100eV and absorbed by the specimen. However, some of the secondary electrons from the top of the sample surface ($<$ 2 nm) may escape the solid into the vacuum and relay information of the topography of the sample. Backscattered electrons (BSE) are produced when the primary electrons interact elastically with the sample and these electrons are ejected from the solid at an angle greater than 90°. BSE possess almost similar range of energy as compared to the primary electrons and provide composition information rather than topographic information [145].

SEM is most commonly used tool for high resolution microstructural images. Proper processing of these images can be utilized to observe surface topography, cracks or porosity in the structure. Even grains and grain boundary can be imaged from properly prepared sample. Ceramic material usually undergo intergranular fracture and imaging fractured surface of ceramic material provides information on grain structure and grain sizes. For the current study, SEM was employed to observe surface cracks and porosity on SPS sintered samples. Moreover, fractured surface from flexural strength study was analyzed using SEM to study fracture mode.

Sample preparation for grain morphology study

To obtain information regarding the grain size and grain boundary, SiC needs to be etched. α-SiC requires Modified Murakami's reagent for etching. Modified Murakami solution was made with 3 g of sodium hydroxide (NaOH) and 30 g of potassium ferricyanide ($K_3Fe(CN)_6$) mixed into 60 mL of distilled water. The samples had to be immersed in the boiling solution ($\sim$110°C) solution for $\sim$8–10 min for proper etching. For β-SiC sample molten salt etching was employed. For molten salt a mixture of 10 g of KNO_3 and 90 g of KOH were heated to a temperature of 480°C and the sample was etched for 5 – 10 min.

III.5 Thermal stability of graphene

Raman scattering

In Raman spectroscopy, the sample is irradiated with laser beams in the UV-visible region. Most of these radiation is either absorbed or transmitted and a small portion of the radiation is scattered in the direction perpendicular to the incident beam. The scattered light can be strong and have the same frequency as the incident beam (ν_0). This is termed as Rayleigh scattering (elastic scattering) where only the momentum is transferred for the incident photons keeping the energy unchanged. If the scattering light is very weak and has frequencies $\nu_0 \pm \nu_m$ (ν_m vibrational frequency of the molecule), then it is called Raman scattering. The photons that loose energy shifts to lower frequency ($\nu_0 - \nu_m$) and known as Stokes shift. When the photons gain energy they shift to higher frequency ($\nu_0 + \nu_m$) and termed as anti-Stokes shift. Therefore, by Raman spectroscopy one can measure vibrational frequency shift from the incident beam frequency [146].

This technique provides information on characteristic values of vibrational frequencies of chemical bonds. Although this technique is a qualitative analysis, it has been used for identifying unknown compounds in solid or liquid phases, detect change in structural order, and phase detection. For the current investigation it is important to understand the interaction between graphene and SiC in the composite. Raman scattering would help in unveiling any structural change in graphene due to thermal degradation. As known, exfoliation of graphite nanoplatelets is important for improvement in mechanical properties. This technique allows unambiguous identification of number of graphene layers by observing the changes in shape, width, and positions of D, G and $G^{'}$ peaks which in turn will give idea about the exfoliation of the graphite nanoplatelets [147]. While it has been well established that high temperature and high pressure processing results in mechanical damage (breakage) of the carbon nanotubes, similar studies have not been conducted for ceramic-graphene composites. For this study, WITec alpha300 R Raman system with a 532 nm laser excitation was used for detailed investigations on fragmentation and exfoliation of graphene in the SPS sintered compacts.

III.6 Mechanical characterization

III.6.1 Bi-axial strength

To determine the failure characteristics of brittle materials, the bi-axial flexure tests are usually used. For this study, ring-on-ring (RoR) biaxial tests will be used to achieve flexural strength for SiC and SiC-C samples. The configuration used in this test exposes the maximum area under a constant maximum stress. Figure III.4 shows the schematic of the RoR fixture, which is an axisymmetric test, where the disc is supported by a ring from one side and loaded by a smaller concentric ring from the other side. This configuration employed a support ring diameter of 15 mm and the loading ring diameter of 5 mm, which ensures valid fracture mode of the samples [148].

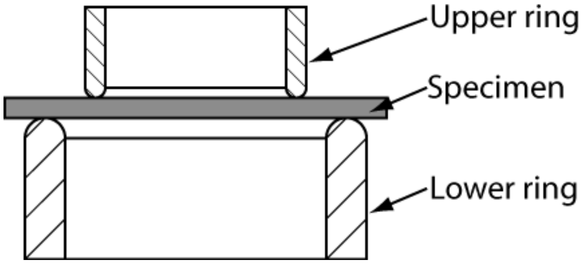

Figure III.4: Schematic of fixture for testing biaxial flexure properties using RoR.

For this test, the discs (SiC and SiC-C) are loaded in the RoR fixture using a table-top test frame (Instron® 5567, Instron Corporation, Norwood, Massachusetts, USA). Adhesive tape is applied on the compressive side of the discs as per ASTM C1499–05 [149]. Displacement controlled loading at a rate of 0.5 mm/min. is used and the peak load at failure is recorded. For each kind of sample, at least 5 discs are subjected to the test to provide a statistical distribution of data.The flexure strength is then determined from the peak load at failure as per Eqn. III.9 [150],

$$\sigma_{\mathrm{RoR}} = \frac{3P}{2\pi t^2}\left[\frac{(1-\nu)(a^2-r^2)}{2R^2} + (1+\nu)\ln\frac{a}{r}\right] \tag{III.9}$$

Where P is the applied load, ν is the Poisson's ratio of the specimen and is assumed to be 0.20 for SiC, a is the radius of the support ring, r is the radius of the load ring, and R and t are the radius and thickness of the disc specimen, respectively.

III.6.2 Vickers hardness

Hardness is a materials ability to resist against plastic deformation under load. Various measurement techniques are used to determine hardness of ceramic materials. Most commonly used technique is Vickers indentation method. In this method, a square based pyramid shaped diamond is pressed using a predefined load against the material under test for a specific time and the surface projected diagonals of the resulting impression is measured after the load is removed (Fig. III.5). The force is applied very smoothly without impact. Hardness value is calculated from the ratio of the applied load to the area of contact of the four faces of the indenter by using the following equation [17].

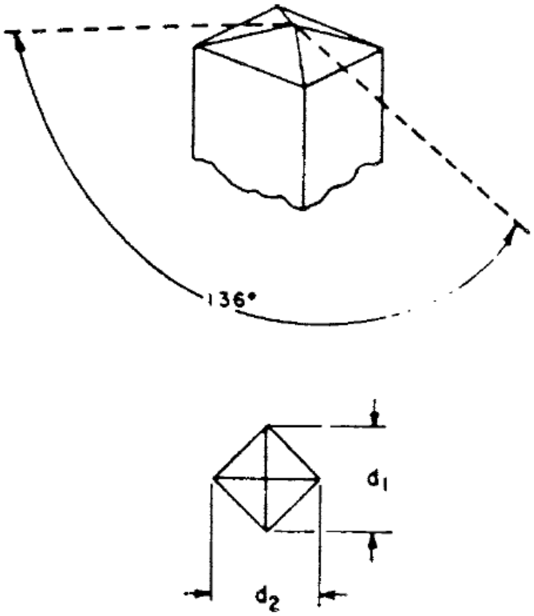

Figure III.5: Schematic of shape of the Vickers indentor and impression of diagonals after load removal [17].

$$HV = 1.8544\left(\frac{P}{d^2}\right) \tag{III.10}$$

Where P is load in kgf and d is the average of length of the two diagonals of the indentation in mm. Vickers hardness unit is HV which can be converted to more commonly used unit GPa by multiplying the HV number by 0.009807.

For the current study, Vickers hardness of the polished samples were obtained using a microhardness tester (Tukon microhardness tester, Page-Wilson corporation, Bridgeport, Connecticut, USA) at a load of 49 N applied for 30s. At least five readings were collected for each sample and an average value is reported.

III.6.3 Fracture toughness and Acoustic emission analysis

One of the major concerns for modern ceramic material is its low fracture toughness which limits its applicability. In this work, microstructure of the silicon carbide is tailored and also reinforced with graphene nanoplatelet to improve fracture toughness of the ceramic. Fracture toughness of a material is defined by the ability of the material containing crack to resist fracture. Different techniques have been used over the years to determine this property of a ceramic namely, direct crack measurement (DCM), indentation strength by bending (ISB), single edge notched beam (SENB), chevron notched beam (CVNMB) etc. Most commonly used technique is the DCM method. If a brittle material is loaded with a sharp indenter and sufficient load is applied both radial cracks develop at the indent as shown in Fig III.6. Fracture toughness was estimated by direct crack measurement (DCM) using the Anstis equation (Eqn. III.11) [151]

$$K_{IC} = A\left(\frac{E}{H}\right)^{\frac{1}{2}}\left(\frac{P}{C^{\frac{2}{3}}}\right) \tag{III.11}$$

where A is a geometric constant (0.016), E is the elastic modulus, H is the hardness value, P is the load, and C is the length of the radial crack from the center of the impression of the indent. In this method, toughness value is a function of radial crack length, elastic modulus and hardness. Since, elastic modulus can be a function of porosity, the following equation proposed by Snead et al. was used for calculating elastic modulus, E [2].

$$E = E_0 \exp(-CV_p) \tag{III.12}$$

Where $E_0 = 460$ GPa is the modulus of non-porous SiC, and $C = 3.57$ is a constant.

Even though this technique provides an average fracture toughness value for a material, it does not provide any insight on various fracture events like crack initiation or crack propagation. Moreover, it does not provide any information on the energy dissipation occurring during the fracture process which helps in better understanding the fracture phenomena in

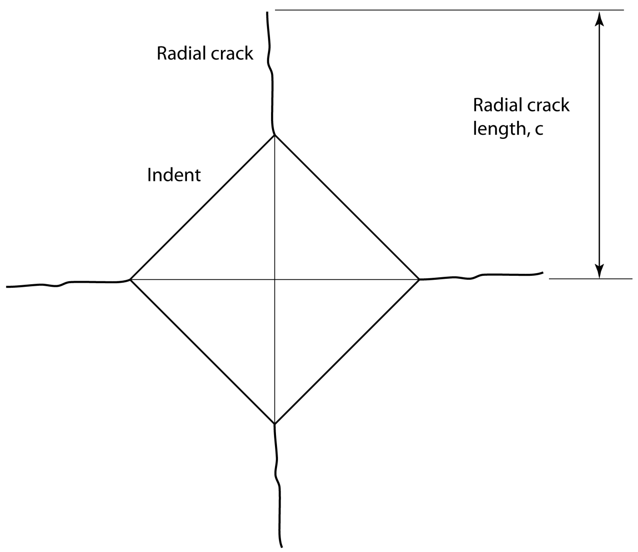

Figure III.6: Schematic representation of radial crack for a brittle material under Vickers indenter.

heterogenous material. The stress waves released due to crack initiation or crack propagation within a material is known as acoustic emission. For brittle material, fracture events are accompanied by sudden changes in stress and strain fields creating acoustic emission within the material. To better understand the fracture events, in addition to DCM method, acoustic emission could be monitored.

For this work, a microhardness tester (Tukon microhardness tester, Page-Wilson corporation, Bridgeport, Connecticut, USA) and a stand alone acoustic emission monitoring system (AMSY-5, Vallen-Systeme GmbH, Munich, Germany) was used to measure fracture toughness while monitoring the acoustic emission related to various fracture phenomena. A schematic representation of the setup is shown in fig. III.7

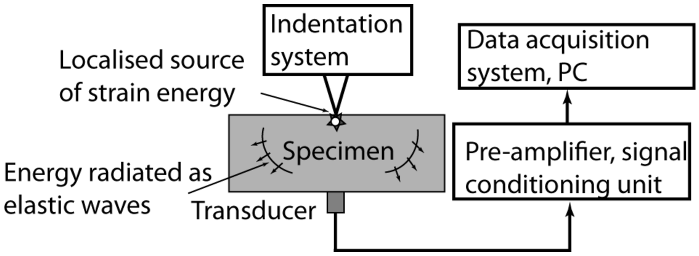

Figure III.7: Schematic representation of AE setup with Vickers indenter.

The AMSY-5 system can store more than 30,000 AE-hits/s and 2.5 MB/s of waveform data. This data is filtered and sorted in real time. Elastic waves generated during fracture events are captured by the piezo-electric sensor and converted into electrical signals. The sensor used for this study had a frequency response in the range of 100 to 400 kHz (AE104A, vallen-systeme GmbH, Munich, Germany). This signal is then fed through a 34dB gain preamplifier that has a response from 2.5 kHz to 3 MHz. From the preamplifier the signal is then sent through acoustic signal preprocessor (ASIPP) to process into digital data with the help of a field programmable gate array (FPGA). Finally, acoustic emission system controller (AsyC) assembles this digital data from ASIPP into data sets and sends to a file in the computer.

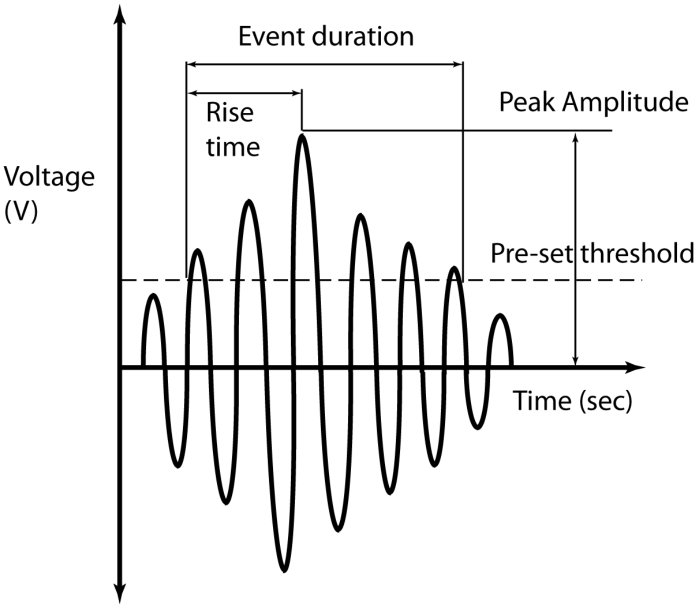

Figure III.8: Schematic representation of acoustic emission waveform.

To monitor AE activity a especially designed sample holder was used. The sensor was placed in the holder such a way that it was directly beneath the sample and a couplant was used to ensure proper transmission of AE events from the sample to the sensor. Typical transient AE waveform contains numerous information such as the number of hits, acoustic energy, rise time, duration time, and peak amplitude as shown in fig. III.8. In this work, we are mainly interested in the acoustic energy that is the integral of the squared of the amplitude over signal duration. The acoustic energy can be directly correlated to the elastic energy released during the fracture events.

While monitoring acoustic emission during indentation, it is important to set a proper threshold to record acoustic emission events without any noise. Initially, a very low threshold (9.9 dB) was set and indentation was performed on aluminum sample. Since aluminum is not brittle, it should not show any indentation induced fracture and should not produced any acoustic emission events during indentation (Fig. III.9). Based on extensive characterization of the aluminum sample, 25.3 dB was chosen as a threshold to avoid recording any noise during indentation experiment. In addition to the threshold, other parameters used for the experiments are sampling rate of 10 MHz and parametric timing of 0.001 s.

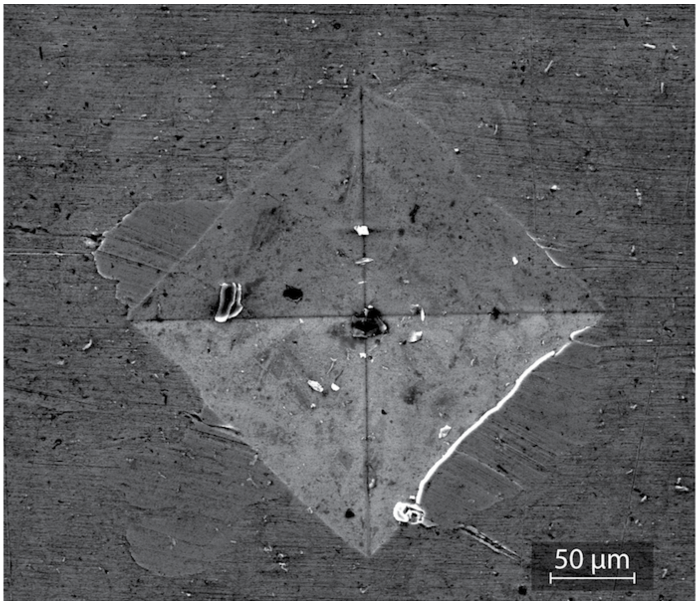

Figure III.9: SEM image of Vickers indent on aluminum showing no fracture.

CHAPTER IV

Characterization of nanostructured silicon carbide consolidated using polymer pyrolysis and spark plasma sintering

IV.1 Polymer–Ceramic formation

To identify the functional groups present in AHPCS and to understand the conversion from polymer to ceramic FTIR was performed as shown in Fig. IV.1(a). The backbone of the polymer is the Si–CH$_2$–Si chain confirmed by three peaks in the spectra for AHPCS; peak at around 1045 cm^{-1} corresponding to CH$_2$ bending, 1355 cm^{-1} corresponding to Si–CH$_2$–Si deformation, and 2920 cm^{-1} corresponding to C–H stretching. Presence of Si–CH$_3$ is identified by three peaks; at around 840 cm^{-1} corresponding to Si–CH$_3$ rocking and Si–C stretching, at around 1250 cm^{-1} corresponding to Si–CH$_3$ stretching and at around 2950 cm^{-1} corresponding to C–H stretching in Si–CH$_3$. Peaks indicating CH=CH$_2$ are at 1630 cm^{-1} corresponding to C=C stretching and 3073 cm^{-1} corresponding to C–H vibration. A strong peak at 2120 cm^{-1} corresponds to Si–H. A peak around 3400 cm^{-1} is due to the water absorbed in the KBr during FTIR experiment [152–154].

After pyrolysis to 350°C (i), intensity of most of the peaks are greatly decreased, especially for Si–H and Si–CH$_3$. The intensity of the C=C stretching at 1630 cm^{-1} and C–H vibration at 3073 cm^{-1} almost disappears from the spectra indicating evolution of CH=CH$_2$. At higher pyrolysis temperature (ii), gradually peak intensity of Si–H decreases which ensures cross-linking by hydrosilylation and dehydrocoupling reactions [152, 153]. Even at 900°C (iii) small peak for Si–H is visible, which disappears at 1150°C (iv) completely as hydrogen is expelled from the structure and polymer to ceramic conversion is completed. At 1400°C (v) only a broad peak corresponding to SiC is present in the IR

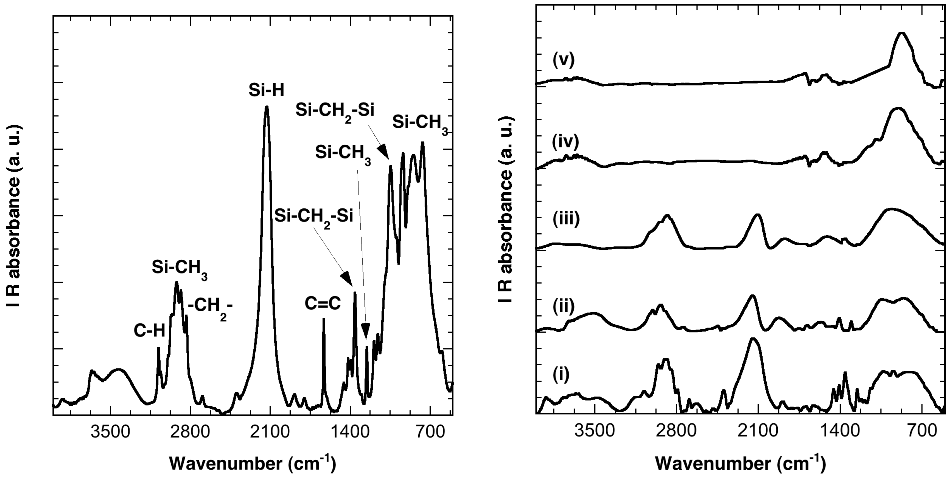

(a) (b)

Figure IV.1: IR Spectra for (a) as received AHPCS and (b) AHPCS heated to 350°C (i), 650°C (ii), 900°C (iii), 1150°C (iv), and 1400°C (v).

spectra.

IV.2 Powder morphology

Scanning electron microscope (SEM) images were used to measure the particle size. Five different images were used and a total of $\sim$300 particles were considered for the measurement. Microstructure of SiC particles after ball milling can be seen in Fig. IV.2 which shows the variation of particle size over a range of 0.2 to 1.25 μm. However, 87% of the particles falls within 0.5 μm range ensuring very small particle size after ball milling. It should be emphasized, however, that this particle size does not indicate grain size of the material after pyrolysis, which is typically in the 1–5 nm range [155].

IV.3 Relative density and Densification

Variation of relative density as a function of sintering temperature is shown in fig. IV.3(a), indicating influence of sintering temperature on densification behavior of SPS sintered SiC. At 1600°C sintering temperature, relative density of the compact is $\sim$60% and increase in sintering temperature to 2000°C showed sudden increase in relative density reaching

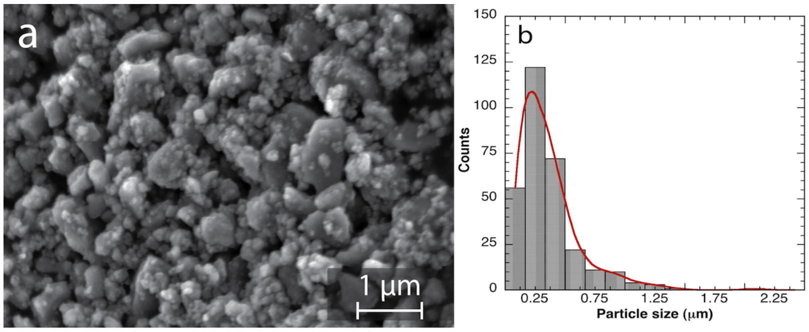

Figure IV.2: Measurement of SiC particle size. (a) Microstructure of SiC particles after high energy ball milling of pyrolyzed AHPCS (b) Distribution of particle size.

92%. The maximum relative density obtained in this investigation is about 95% at 2100°C sintering temperature. To understand the densification process, temperature profile, punch displacement, D and displacement rate, dD/dt as function of time for 2100°C sintering temperature is plotted as shown in fig. IV.3(b). Note that sintering pressure of 70 MPa was applied such a way that in each case the pressure reached 70 MPa when the temperature reached desired sintering temperature. Initially applied pressure starts to rearrange the particles, however, rise in temperature results in expansion of the punch as shown in case of displacement till $\sim$12.5 min. During this period densification of the compact is much lower compared to expansion of the punch, hence decrease in displacement is observed. This is also evident in the displacement rate curve. After that initial period at around 1875°C, displacement starts to increase and displacement rate is maximum at 2000°C. Temperature dependent densification mechanisms such as diffusion is activated after 1875°C. Hence, sintering temperature below 1900°C results in lower relative density of the compacts.

Commercial SiC powder was difficult to sinter without sintering additives even at 2100°C reaching a relative density of 82%. Addition of Al_2O_3 as binder improved sinterability of the commercial powder increasing the relative density to 96%. Relative density of conventionally hot pressed Hexoloy, SA sample was 98.4%.

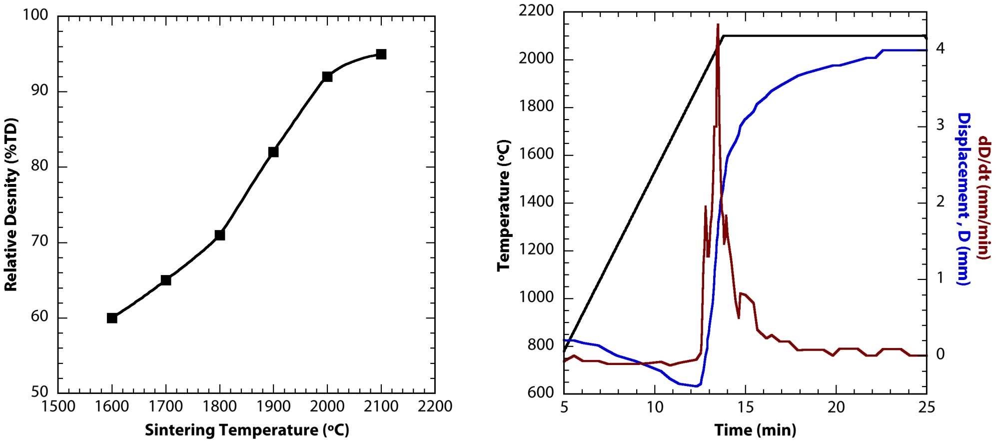

(a) (b)

Figure IV.3: Variation of (a) density as a function of sintering temperature for SPS sintered SiC samples (b) temperature profile, punch displacement, D and displacement rate, dD/dt as function of time.

IV.4 Microstructural evolution

For the current work, SiC powder prepared using polymer pyrolysis at 1400 °C was characterized using x-ray diffraction (XRD). Figure IV.4(a) shows XRD patterns of starting amorphous powder as well as samples compacted using SPS technique. The XRD pattern of the initial SiC powder, obtained through pyrolysis at 1400 °C, exhibited characteristic broad halo peaks with diffused intensity indicating an amorphous/nanocrystalline structure. SPS of amorphous/nanocrystalline powder at various temperatures ranging from 1600 °C to 2100 °C resulted in crystallization of amorphous powder during sintering. Peaks at 36°, 42°, 60°, and 72° correspond to (111), (200), (220) and (311) planes of β-SiC (ICCD: 29–1129). Two small peaks correspond to residual tungsten carbide (WC) which was used as a grinding media for ball milling. For 2000°C and 2100°C SPS sintered samples at 26.43° a small peak can be observed that corresponds to nanocrystalline carbon. Full pattern analysis was performed using XFIT program utilizing fundamental parameters (FP) approach [156]. Calculated average crystallite sizes were 97, 187, 197, 271, 370, and 540 nm for samples sintered at 1600, 1700, 1800, 1900, 2000, and 2100 °C, respectively. This shows that preparing amorphous/nanocrystalline SiC powder using pyrolysis of preceramic precursor and then preparing bulk SiC using SPS can be used effectively to control the grain size.

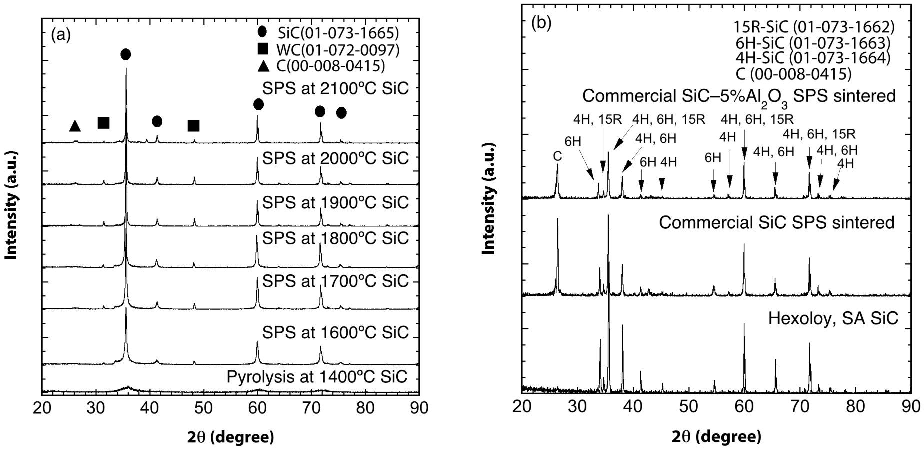

(a) (b)

Figure IV.4: XRD patterns from (a) amorphous SiC powder and spark plasma sintered SiC compacts processed at various temperatures (b) SPS sintered commercial SiC and Commercial Hexoloy SA

XRD patterns for Hexoloy SA, SPS sintered commercial SiC and SPS sintered commercial SiC with binder show peaks for α-SiC as shown in Fig. IV.4(b). Note that samples sintered from commercial powder showed presence of graphite peak at 26.43° indicating excess carbon in the structure. Full pattern analysis was employed in a manner mentioned earlier to estimate average crystal size. Estimated grain sizes were 4.2, 4.1 and 3.0 μm for Hexoloy SA, commercial SiC and commercial SiC-Al_2O_3, respectively. Using same processing parameters resulted in a significantly larger grain size for samples sintered from commercial SiC powder due to crystalline nature of initial powder as compared to pyrolyzed powder that was mostly amorphous in nature.

Grain sizes were also estimated from SEM images of etched samples. Molten salt etching was used for β-SiC samples sintered at 1900, 2000, and 2100 °C and modified Murakami's reagent was used for etching Hexoloy SA, commercial SiC, and commercial SiC-Al_2O_3 samples. In the etching process, etchant selectively etches the grain boundary delineating the microstructure. Figure IV.5 shows variation of microstructure based on

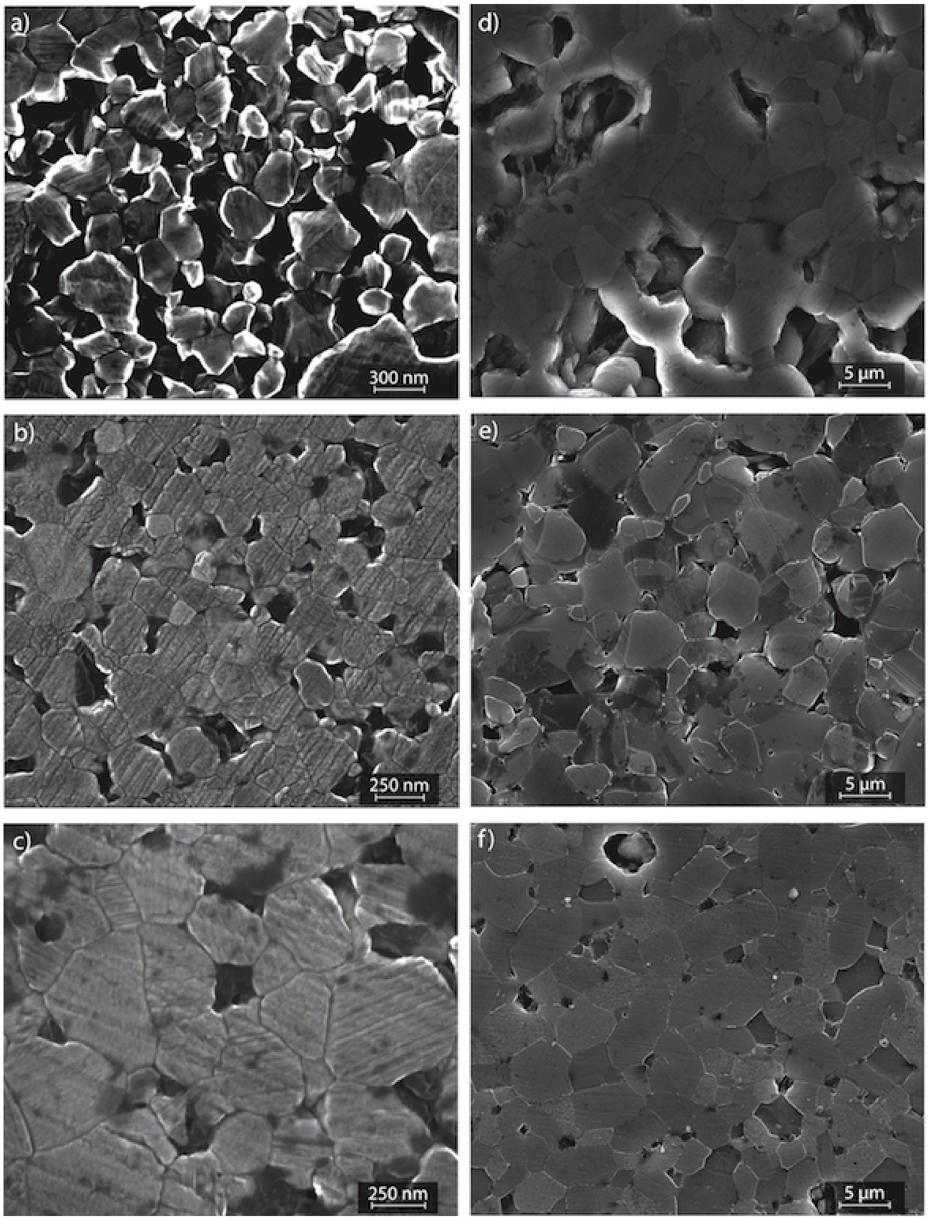

Figure IV.5: Scanning electron micrographs of etched a) 1900°C SiC, b) 2000°C SiC, c) 2100°C SiC, d) Commercial SiC, e) commercial SiC-Al_2O_3, and f) Hexoloy SA.

sintering temperature and source of initial powder. Linear intercept method was used to estimate grain sizes from the SEM images and the shape correction factor employed was 1.22 considering equiaxed grains. For samples sintered using pyrolyzed powder, grain sizes were 260, 345, and 470 nm for sintering temperature 1900, 2000, and 2100°C respectively. Grain sizes were 4.4, 5.0, and 3.9 μm for Hexoloy SA, commercial SiC, and commercial SiC-Al_2O_3, respectively. It is notable that using Al_2O_3 as binder restricts grain growth as reported previously [72]. Grain sizes estimated from both XRD and SEM showed similar trend indicating fabrication approach utilized in the current investigation allows better control over evolution of microstructure during fabrication.

IV.5 Mechanical properties

Increase in hardness with decreasing grain size is reported in literature for both oxide and non-oxide ceramics [157,158]. Vickers hardness of the sintered SiC samples in the present study, however, showed an increasing trend with increase in processing temperature. This is mainly due to the higher residual porosity in the structure at lower sintering temperature resulting in decrease in hardness. Yamamoto et al. also measured increase in Vicker's hardness with the increase of relative density reaching a hardness value of 20 GPa for nanograined-SiC consolidated using SPS [90]. Moreover, Lomello et al. reported influence of density to be stronger than the influence of grain size when grain size of SiC was under 130 nm [94]. In that study, hardness increased to ~25 GPa as a function of density. In the present study, hardness increased from ~4 GPa to ~25 GPa as a function of density. Ryshkewitch reported an exponential dependence of compression strength on porosity content for different ceramic materials [159] and Snead et al. extended this relationship for hardness of ceramic material using the following equation [2]

$$Hv = Hv_0 \exp(-CV_p) \tag{IV.1}$$

Where Hv is Vicker's hardness in GPa, Hv_0 is Vicker's hardness without porosity, C is a constant (5.4), and V_p is volume fraction of porosity. Variation of hardness as a function of porosity content is shown in figure IV.6. The hardness values were fitted to a curve using Eqn. IV.1 by least squares technique. R-squared value determined to be ~0.99 ensured good fit to the experimental data.

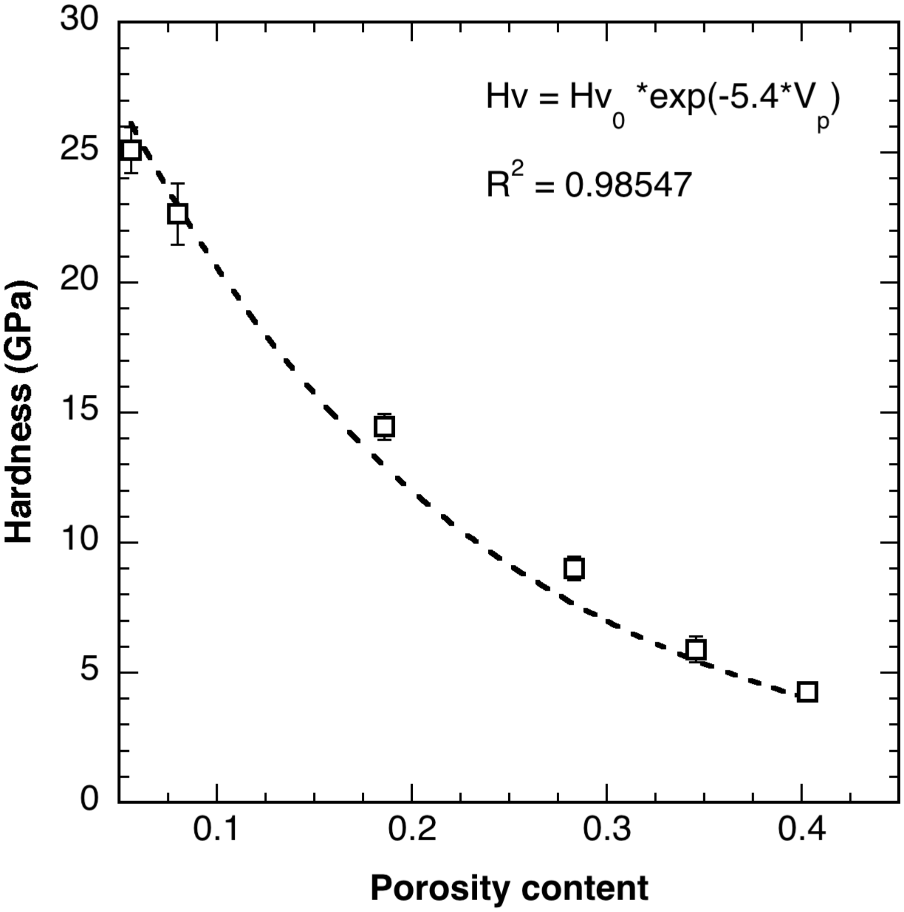

Figure IV.6: Hardness as a function of porosity content for SPS sintered SiC samples.

Hexoloy, SA with 98.4% relative density showed hardness of 25.2 GPa which is similar to hardness of sample sintered using pyrolyzed powder. Dong *et al.* reported Vicker's hardness of 36 GPa for Hexoloy, SA at room temperature with an indentation load of 9.8 N [160]. This is significantly higher than the value observed in the current investigation. This discrepancy is likely due to the difference in indentation load (49 N) used in the current study usually known as indentation size effect [161–163]. Hardness of the commercial SiC sample sintered at 2100°C was largely influenced by porosity of the material. Even at this sintering temperature lack of sinterablility resulted in a moderate hardness of $\sim$ 8.1 GPa. Addition of sintering additive to the commercial powder improved densification, hence, it was expected to have higher hardness value. However, use of 49 N load resulted in deformed indents with surface cracks making it difficult to measure hardness at this load. Therefore, a load of 9.8 N was used to measure hardness of the material. Even though hardness of commercial SiC improved to 20.5 GPa with the addition of binder, still it was less than samples of similar relative density prepared using pyrolysis. This discrepancy in hardness could be explained based on the fracture mode observed in respective materials. Flinders *et al.* previously reported decrease in hardness with change in fracture mode from transgranular to intergranular [164]. As fracture mode changes from transgranular to intergranular, displacing grains during indentation process becomes easier as the crack propagates through the grain boundaries. Hence, drop in hardness is expected. Figure IV.7 shows fracture surface images of different materials used in this study. It should be noted that both SiC sintered at 2100°C and Hexoloy, SA showed transgranular fracture (figs. IV.7a, b) that correlate with higher hardness value observed for these materials. Although commercial SiC sintered at 2100°C showed a mix of transgranular and intergranular fracture, hardness value was dominated by porosity of the material. Interestingly, addition of Al_2O_3 to the commercial powder completely changed the fracture mode to intergranular. This change is a result of grain boundary chemistry as Al and O have been shown to aggregate at the grain boundary [164, 165]. With this change in fracture mode, commercial SiC-Al_2O_3 showed less hardness even with improved densification.

In the current study, flexural strength was determined using a bi-axial flexure setup that utilizes ring-on-ring configuration. This configuration gives the most accurate measure of strength among all the bi-axial setup that are being used [166]. Moreover, bi-axial flexure condition is considered more reliable compared to uni-axial flexure because of maximum tensile stresses occurring within the central loading area, and failure is independent of edge condition. Flexural strength increased from 46 MPa to 302 MPa as

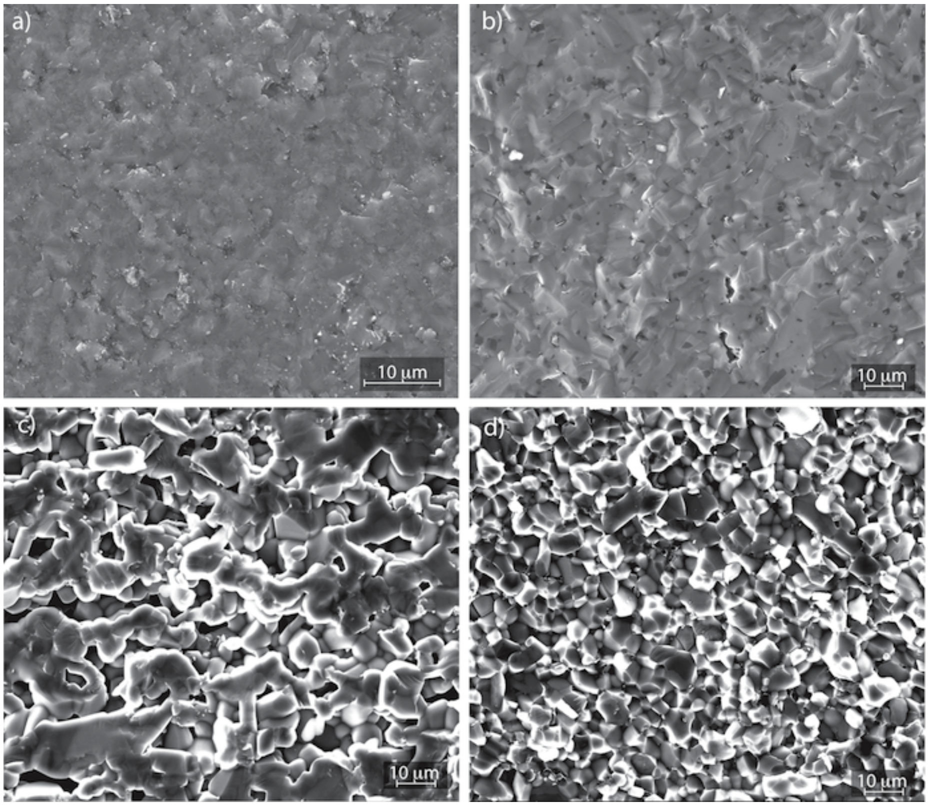

Figure IV.7: SEM fracture surface images of (a) SiC sintered at 2100°C (b) Hexoloy, SA (c) Commercial SiC sintered at 2100°C and (d) Commercial SiC-Al_2O_3 sintered at 2100°C showing different fracture mode.

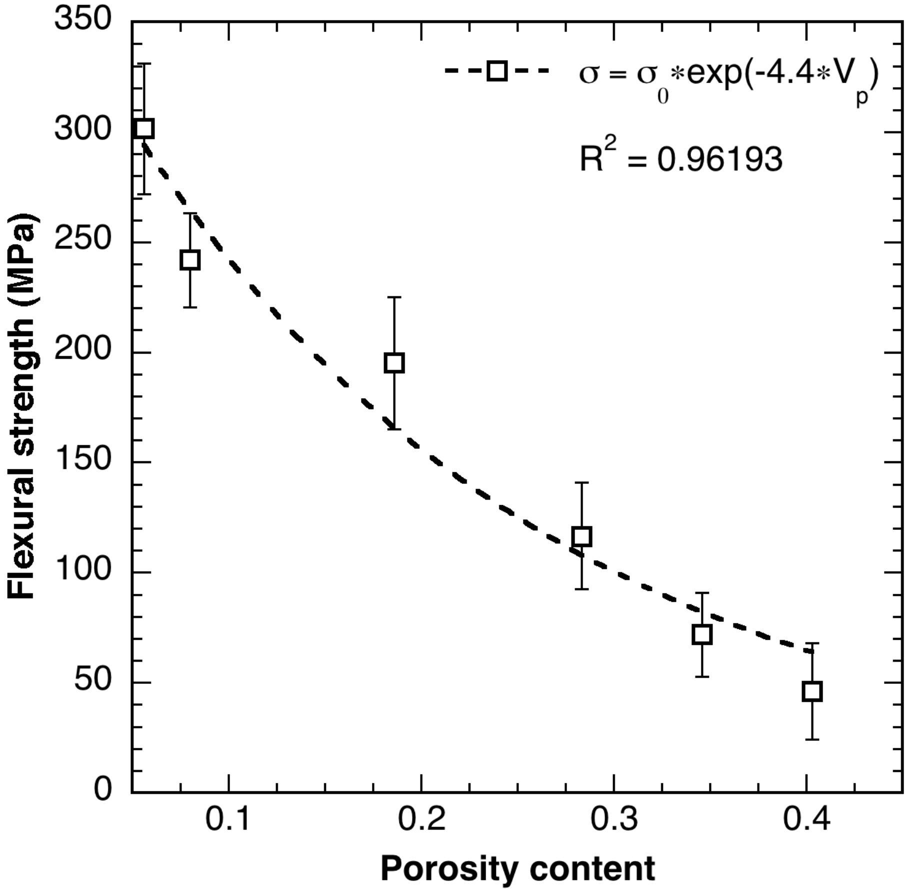

Figure IV.8: Flexural strength as a function of porosity content for SPS sintered SiC samples.

porosity content was reduced with increase in sintering temperature from 1600 to 2100 °C as shown in fig. IV.8. Strength of ceramics depends on relative density, flaw size and grain size. However, for porous ceramics, strength is affected more by porosity than grain size. In general, porosity reduces strength of ceramics by reducing the effective load bearing area [167]. Using the relationship proposed by Ryshkewitch for dependence of strength on porosity content, a curve fitted to the strength values produced a good fit (R-squared value $\sim$96) [159]. The highest value of flexural strength of 302 MPa was observed for sample sintered at 2100°C. This strength value may seem a little lower compared to usually published uni-axial strength data for SiC, but it should be noted that equibiaxial strength of a brittle material is usually lower than uni-axial strength because of more flaws being subjected to high stress at bi-axial test configuration [168]. Several authors have found bi-axial strength to be 20–35% less than uni-axial strength when four-point bending configuration was used [169, 170].

In comparison, commercially available Hexoloy SA also showed slightly lower ($\sim$ 289 MPa) bi-axial strength value. Uni-axial strength of Hexoloy SA using four point bend test is 380 MPa as supplied by the manufacturer. This is 24% higher than the bi-axial strength found in the current investigation and consistent with previous observations as mentioned earlier. Commercial SiC sample sintered at 2100°C showed bi-axial strength of 104 MPa that was 66% less than β-SiC sample sintered using the same parameters. Large flaws in terms of residual porosity in the commercial SiC due to lack of sinterability was responsible for this low strength of the material. Addition of binder significantly improved density of the sintered commercial SiC-Al_2O_3 to 96% and strength also increased to $\sim$276 MPa. With the addition of additives, 14% increase in density resulted in 62% increase in strength for commercial SiC sample. Nonetheless, the strength of commercial SiC-Al_2O_3 was 8% less than SiC samples sintered using pyrolyzed powder. This is due to the embrittlement of the grain boundary as a result of impurities in the form of Al_2O_3 [171]. Recently, in an effort to sinter SiC without binders Yamamoto et al. used SPS to consolidate SiC powder prepared using mechanical alloying of commercially available Si and C powder [90]. Although dense SiC ceramics were prepared using this method, bending strengths were lower compared to commercially available SiC powder consolidated with additives using SPS method. It is suspected that the mechanical alloying leads to incomplete Si–C bonding in the starting powder. This manifests itself as lower mechanical strength in the sintered compact. The processing presented in the present study, however, results in greatly improved properties as the starting SiC powder is prepared by a chemical pyrolysis route which leads to proper Si–C bonding in the starting powder.

Material	**Sintering temperature (°C)**	**Relative density (%)**	**Flexural stregnth (MPa)**	**Vickers hardness (GPa)**	**Fracture toughness (MPa m$^{1/2}$)**
SiC	1900	82.0	195±30	14.5±0.5	3.0±0.1
SiC	2000	92.3	242±21	22.6±1.2	3.4±0.1
SiC	2100	95.0	302±29	25.1±0.9	3.5±0.1
Commercial SiC-5%Al_2O_3	2100	96.0	276±54	20.5±1.4	4.0±0.4
Hexoloy SA	–	98.7	289±56	25.2±0.8	2.5±0.1

Table IV.1: A summary of properties of sintered SiC from AHPCS, powder from commercial source and Hexoloy SA determined in this study

Fracture toughness measured using direct crack measurement (DCM) method is presented in Table IV.1. Samples with proper radial cracks were used for toughness measurement. For samples sintered using pyrolyzed powder, toughness increased with reduction in porosity. Such behavior has been observed by other authors [93]. Fracture resistance depends on crack propagation path and impurities at grain boundary. For non-detectable impurities at grain boundary, grain boundary toughness can be higher than grain toughness rendering transgranular fracture [171]. This has been observed in the current study for materials sintered using pyrolyzed powder as shown in fig. IV.7. Interestingly, Hexoloy SA also showed transgranular fracture as the amount of additives in the sintered material was very less [160]. Nonetheless, the fracture toughness of Hexoloy SA was 40% lower than the fracture toughness of the SiC sintered at 2100°C using pyrolyzed powder. Similar fracture toughness of Hexoloy SA has been reported by other authors using DCM method [172].

Since both samples had similar relative density and hardness, this variation is only a function of crack resistance measured as radial crack length. Finer grains can enhance toughness by impeding crack propagation. As Hexoloy SA had much larger grain size (4.4 μm) compared to SiC sintered at 2100°C (440 nm), difference in toughness for these materials can be observed as a result of such mechanisms. On the contrary, commercial SiC-Al_2O_3 showed higher fracture toughness ($\sim$4.0) compared to the rest of the materials. For this material, Al_2O_3 segregates at the grain boundary rendering the grain boundary weaker than the SiC grains. As a result, crack propagation was changed to intergranular mode from mixed mode in the binder less commercial SiC (fig. IV.7). Intergranular fracture can improve fracture toughness if crack driving force is decreased by deflection of the crack along grain boundaries and not superseded by decrease in grain boundary toughness due to the segregating impurities. In case of commercial SiC-Al_2O_3, toughness of Al_2O_3 is slightly less than SiC. Hence, decrease in crack driving force results in slightly higher toughness in commercial SiC-Al_2O_3.

CHAPTER V

Processing graphene nano-platelet reinforced silicon carbide consolidated using polymer pyrolysis and spark plasma sintering

V.1 Exfoliation and dispersion of graphene nanoplatelets

One of the main challenges in preparing graphene reinforced ceramic matrix is the development of a processing technique to produce good dispersion of the graphene sheets in the ceramic matrix. Dispersion of the graphene sheets significantly affects the final properties of the composite. For last ten years significant effort has been directed towards effective dispersion of carbon nanotube (CNT) in ceramic matrix [12, 34–37]. Since CNT is rolled up form of graphene, similar dispersion and processing parameters can be used to prepare well distributed graphene reinforced ceramic composites. Moreover, graphene with high specific surface area and 2D geometry has better processability compared to CNT [173] that can result in better dispersion in the ceramics matrix.

Most commonly used techniques include powder processing and colloidal processing. In powder processing, filler material is agitated using ultrasonication in a solvent first and then mixed with the ceramic powder in the same solvent using high energy ball milling to produce a slurry of graphene-ceramic mixture. There have been some reports of graphene dispersion and exfoliation using powder processing for Si_3N_4 and Al_2O_3 matrix using different solvent [16, 174]. Solvents used for this method are N-methyl-pyrrolidone (NMP), Dimethylformamide (DMF), γ-butyrolactone (GBL), ethanol, isopropanol etc. Some of them are energetically more favorable for dispersion such as NMP, DMF. However, these solvents are expensive and toxic. Moreover, they have high boiling point making their deposition difficult on surfaces [105]. In colloidal processing, both graphene and ceramic powders are suspended separately in the same solvent by magnetic stirring or untrasonication. The main difference between colloidal processing and powder processing is the surface modification of the filler and ceramic matrix powder before the processing. This modification is achieved by functionalization or by surfactants that creates opposite charges on the surface of the powder. Functionalization is achieved by adding oxide, carboxyl groups on the edge of the graphene sheets. Commonly used surfactants are sodium dodecylbenzene sulfonate (SDBS), cetyl trimethyl ammonium bromide (CTAB).

Enthalpy of mixing calculation

Before using a solvent for exfoliation and dispersion of graphene nanoplatelets, it is important to determine what is the driving force for exfoliation of graphene. External energy is provided for exfoliation of graphene in the solvent by using ultrasonication or ball milling. Hence, the solvent that requires less energy to exfoliate graphene should work better. According to Hernandaz et al. the enthalpy of mixing can be calculated from [175]

$$\frac{\Delta H_{mix}}{V_{mix}} = \frac{2}{T_{flake}}(\delta_G - \delta_{sol})^2\phi \tag{V.1}$$

Where ΔH_{mix} is the enthalpy of mixing, V_{mix} is the volume of the mixture, T_{flake} is thickness of graphene flake, $\delta_G = \sqrt{E^G_{sur}}$ is the square root of the surface energy of graphene, $\delta_{sol} = \sqrt{E^{sol}_{sur}}$ is the square root of the surface energy of solvent, and ϕ is the graphene volume fraction. From equation V.1 we can see that

$$\frac{\Delta H_{mix}}{V_{mix}} \propto (\delta_G - \delta_{sol})^2 \tag{V.2}$$

The smaller the value of $\frac{\Delta H_{mix}}{V_{mix}}$, the higher the probability of exfoliation of graphene. $\frac{\Delta H_{mix}}{V_{mix}}$ will be small, even close to zero if surface energies of graphene and solvent are similar. Surface energy of graphite ranges from ~50 – 75 mJ m^{-2} based on different study [176, 177]. So, a solvent with surface energy within that range would work well for exfoliation and dispersion of graphene.

To determine surface energy of the solvent we have to know the surface tension of the solvent. The following equation shows the relation between surface free energy and surface tension of a solvent

$$E_{Sur}^{Sol} = \gamma_{Sur}^{Sol} + TS_{Sur}^{Sol} \tag{V.3}$$

Where E_{Sur}^{Sol} is the surface energy of the solvent, γ_{Sur}^{Sol} is the surface tension of the solvent, T is temperature in K, and S_{Sur}^{Sol} is the solvent surface entropy. S_{Sur}^{Sol} is a liquid property that varies between 0.07 – 0.14 mJ $\mathrm{m}^{-2}\mathrm{K}^{-1}$. Hence, for calculation S_{Sur}^{Sol} is considered to be 0.1 mJ $\mathrm{m}^{-2}\mathrm{K}^{-1}$. Now if we consider the temperature to be 25°C (298 K), then Eq V.3 becomes,

$$E_{Sur}^{Sol} = \gamma_{Sur}^{Sol} + 29.8 \tag{V.4}$$

Based on equation V.4 we can find E_{Sur}^{Sol} for different solvent as shown in table V.1. As can be seen from the table that NMP and DMF have higher surface energy and will work well for exfoliation of graphite. As mentioned earlier these are expensive and toxic, hence were not used in this study. As per manufacturer's note and the surface energy calculation, isopropanol was used as dispersing media for powder processing where 2 wt% and 5 wt% graphene nanoplatelets were mixed in isopropanol with SiC powder produced using pyrolysis of AHPCS. However, one concern that has not been addressed surprisingly is the possibility of agglomeration of the nanofillers after the solvent is evaporated before further processing. In most cases, the solvent is dried using rotary evaporator or by heating to a higher temperature.

To avoid the possibility of re-agglomeration, another set of samples were prepared using the polymer precursor (AHPCS) as dispersing media. From table V.1 it is evident that AHPCS is also energetically favorable for graphene exfoliation and dispersion. Moreover, dispersion using the solvents mentioned above (NMP, DMF, and IPA) have been shown to

Solvent	Surface tension, γ (mJ/m^2)	Surface energy, E^{Sol}_{Sur} (mJ/m^2)
N-methyl-pyrolidone (NMP)	40.1	69.9
Dimethylformamide (DMF)	37.1	66.9
Isopropanol (IPA)	21.7	51.5
Allylhydridopolycarbosilane (AHPCS)	30.0	60.0

Table V.1: Surface energy for different solvent.

be stable for 4–5 weeks before graphene nanoplatelets starts to re-aggregate again [175]. Keeping this in mind, we believe that using AHPCS as dispersing media and later pyrolyzing it would result in entrapment of exfoliated graphene sheets in SiC matrix. This is schematically represented in Fig. V.1.

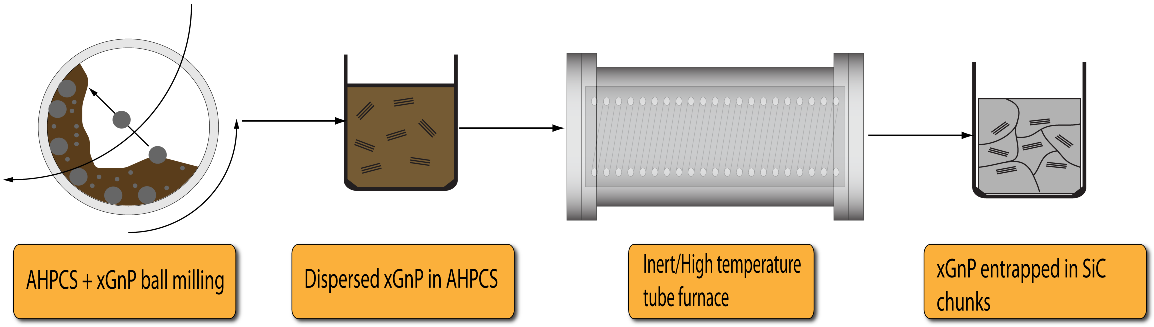

Figure V.1: Schematic of graphene-AHPCS pyrolysis.

V.2 Polymer–Ceramic formation

FTIR was performed to identify any change in conversion from polymer to ceramic due to the addition of graphene as shown in Fig. V.2. Polymer to ceramic conversion almost follows the same curing process. Slight difference is observed in terms of peak intensity. Both 2120 cm^{-1} (Si-H) and 2950 2120 cm^{-1} (C-H stretching in Si-CH$_3$) have a lower peak intensity at 350°C for 2wt% and 5wt% samples compared to AHPCS pyrolyzed at 350°C. However, this does not affect the pyrolysis cycle and at 1400°C a sharp peak for SiC can be observed. There is also a peak at around 1500 cm^{-1} that corresponds to C=C bending due to the addition of graphene nanoplatelets.

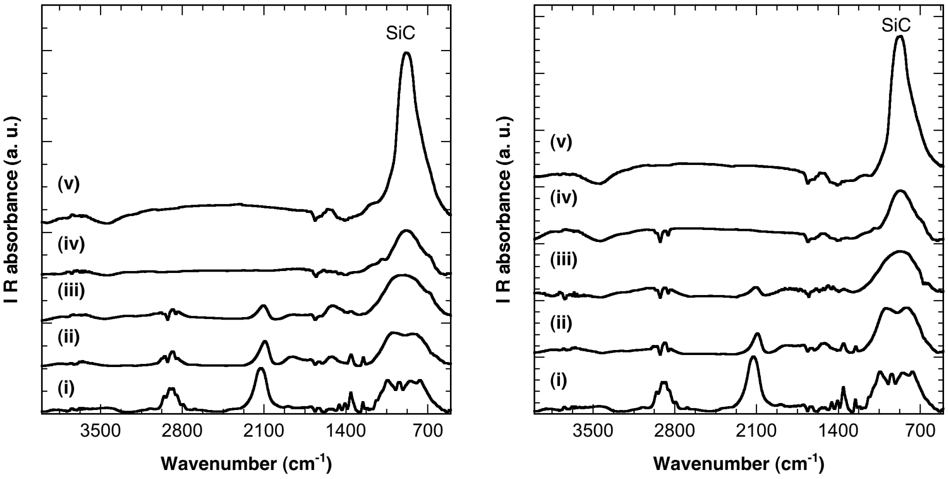

(a) (b)

Figure V.2: IR Spectra for (a) AHPCS-2wt% C and (b) AHPCS-5wt% C heated to 350°C (i), 650°C (ii), 900°C (iii), 1150°C (iv), and 1400°C (v).

V.3 Relative density and Densification

Variation of relative density as a function of sintering temperature and graphene content is presented in table V.2. It is interesting to note that graphene content influence densification along with sintering temperature. Moreover, different dispersion routes also have effect on evolution of porosity in the bulk compact. Absolute density was calculated using rule of mixture as shown in equation V.5.

$$\rho_c = \frac{1}{(W_f/\rho_f) + (W_m/\rho_m)} \tag{V.5}$$

Where, ρ_c =Density of the composite, W_f and W_m are weight fractions of graphene nanoplatelets and SiC, respectively, $\rho_f = 2.2$ g/cc is density of xGnP platelets and $\rho_m = 3.21$ g/cc is density of SiC.

From table V.2 it can be clearly seen that temperature plays an important role in densification with graphene addition. Especially in case of separate graphene addition in SiC matrix using IPA, even at 2000°C the relative densities are 85% for 2wt% C and 88% for 5wt% C addition. Moreover, open porosities are much higher compared to other samples. However, at 2100°C density improves for both samples. It is believed that addition of car-

Sintering temperature (°C)	Sample	Density (g/cc)	Relative density (%)	Open porosity (%)
2000	AHPCS-2wt%C	2.92±0.09	92	1.70
2100	AHPCS-2wt%C	2.98±0.04	94	0.92
2000	AHPCS-5wt%C	2.87±0.05	92	4.27
2100	AHPCS-5wt%C	2.90±0.05	93	1.66
2000	SiC-2wt%C	2.70±0.05	85	11.83
2100	SiC-2wt%C	2.91±0.07	92	2.42
2000	SiC-5wt%C	2.77±0.03	88	8.73
2100	SiC-5wt%C	2.82±0.11	90	4.34

Table V.2: Density and open porosity of graphene reinforced SiC samples at 2000°C and 2100°C sintering temperature.

bon during sintering of SiC activates the sintering process. Furthermore, carbon helps in eliminating the oxide impurities residing at the grain boundaries [178]. At higher sintering temperature the following reaction takes place when there is no excess carbon [179].

$SiO_2 + nSiC = Si \uparrow + SiO \uparrow + CO \uparrow + (n-1)SiC$

Clearly, more volatile products are formed resulting in weight losses at higher sintering temperature. On the other hand, excess carbon leads to the following reaction [179].

$SiO_2 + nSiC + 3\,C = CO \uparrow + (n + 1\,)SiC$

Hence, addition of C would reduce weight losses by reducing the production of volatile phases during sintering. However, addition of carbon can affect densification mechanisms, especially at higher weight fraction. It has been observed that higher weight fraction of only carbon addition can hinder mass transport mechanisms in sintering of SiC [180]. Stobierski et al. performed a systematic study on effect of carbon addition in sintering of SiC [179]. They have observed that addition of 3wt% or more carbon can affect mass transport mechanism which in turn affects pore elimination process and hinders densification of SiC. Moreover, distribution of carbon content can affect the densification mechanism even at lower weight fraction. This effect is evident in case of SiC-graphene samples where the distribution of graphene is believed to be uneven due to processing technique. For SiC-2wt% C and SiC-5wt% C, the densification mechanism is affected due to non-uniform distribution of graphene and results in lower relative density. Increasing the sintering temperature to 2100°C, however, provides better densification for all the samples leading to relative density at or above 90%.

V.4 Microstructural evolution

For the current work, 5wt% graphene-SiC powder prepared using polymer pyrolysis at 1400 °C was characterized using x-ray diffraction (XRD). Figure V.3 shows XRD patterns of starting amorphous/nanocrystalline powder as well as samples compacted using SPS technique. The XRD pattern of the initial graphene-SiC powder, obtained through pyrolysis at 1400 °C, exhibited characteristic broad halo peaks with diffused intensity indicating an amorphous/nanocrystalline structure. Moreover, a peak at 26.4° for (002) plane of graphite indicates the presence of graphene after pyrolysis. Note that this peak was not observed for powder prepared using only AHPCS. SPS of amorphous/nanocrystalline powder at 2100 °C resulted in crystallization of amorphous powder during sintering. Peaks at 36°, 42°, 60°, and 72° correspond to (111), (200), (220) and (311) planes of β-SiC (ICCD: 29–1129). It is postulated in literature that well exfoliation and dispersion of graphene platelets will result in either no peak or very small peak at 26.4° [177]. One can observe that for AHPCS-2wt%

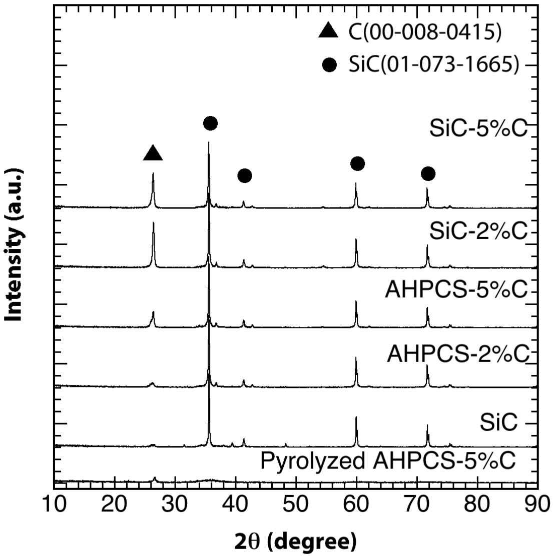

Figure V.3: XRD patterns from amorphous SiC-graphene powder and spark plasma sintered graphene-SiC compacts processed at 2100°C.

C, the peak at 26.4 is very small compared to other samples. Even with AHPCS-5wt% C the graphene peak intensity is much smaller compared to SiC-2wt% C and SiC-5wt% C. This also corroborates our earlier claim that using a separate solvent for dispersion results in non-uniform distribution.

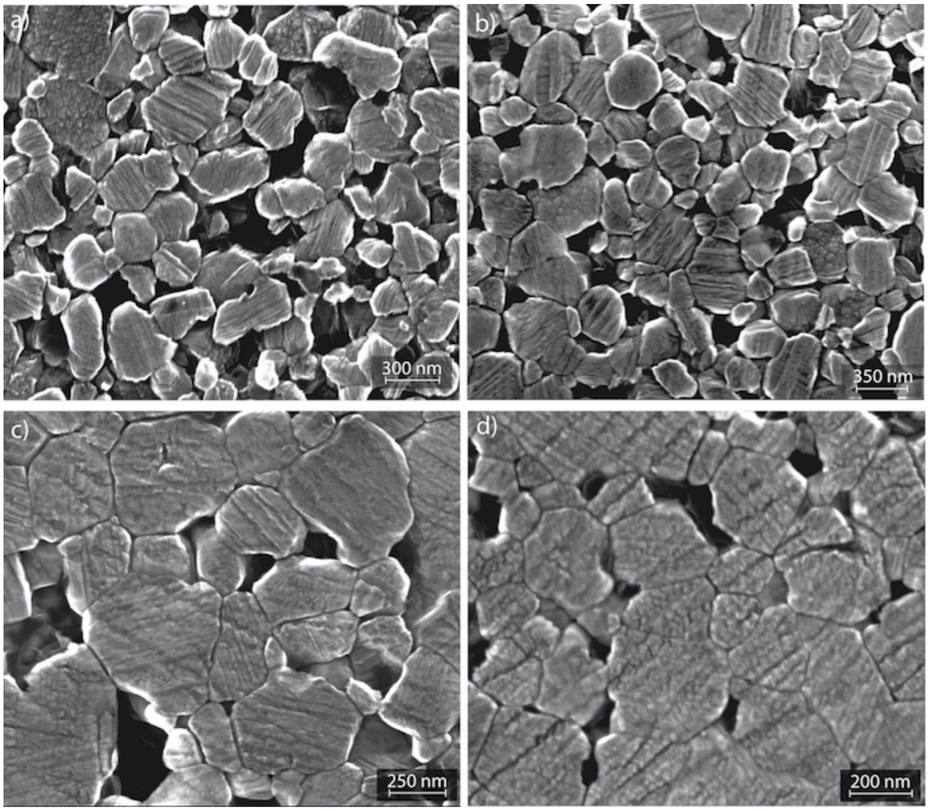

Figure V.4: Scanning electron micrographs of etched a) AHPCS-2wt%C, b) AHPCS-5wt%C, c) SiC-2wt%C, and d) SiC-5wt%C sintered at 2000°C.

Full pattern analysis was performed using XFIT program utilizing fundamental parameters (FP) approach [156]. Calculated average crystallite sizes were 540, 495, 301, 407, and 368 nm for SiC, AHPCS-2%C, AHPCS-5%C, SiC-2%C, and SiC-5%C samples sintered at 2100 °C, respectively. It has been previously reported that addition of graphene restricts grain growth of ceramic matrix during sintering [181, 182]. Addition of carbon lowers dissociation pressure of SiC system rendering limited mass transport through the gas phase. As a result, surface diffusion mechanism is restricted leading to grain refinement [179]. Similar effect is observed in the current study. For the same sintering temperature, addition of 5wt% C lead to 40% reduction in grain size.

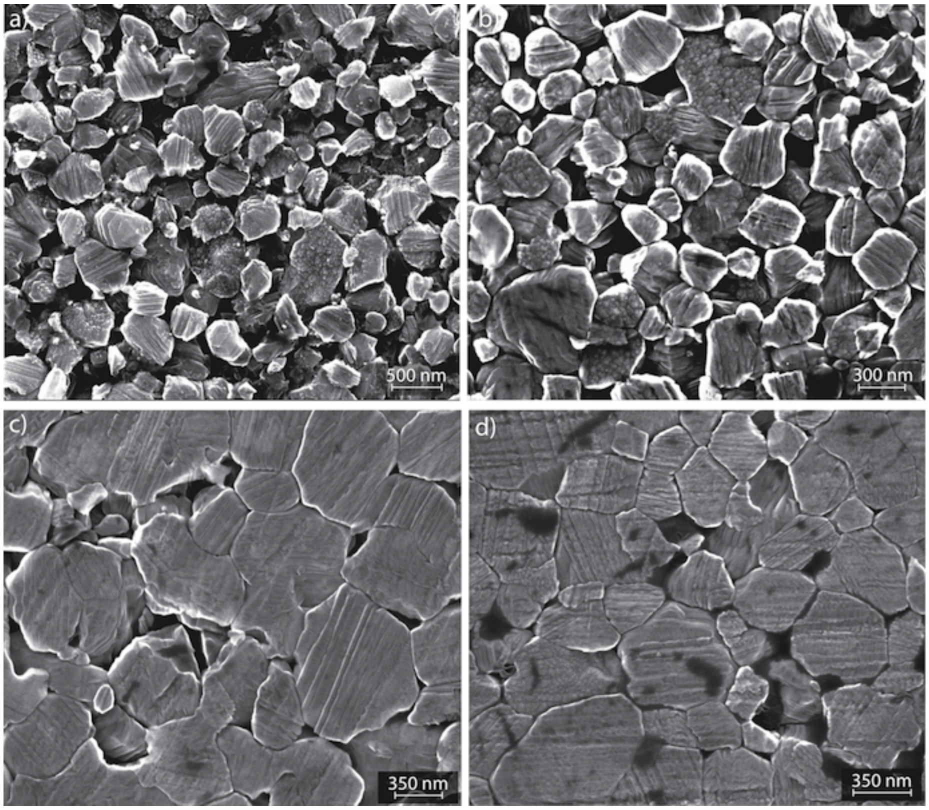

Figure V.5: Scanning electron micrographs of etched a) AHPCS-2wt%C, b) AHPCS-5wt%C, c) SiC-2wt%C, and d) SiC-5wt%C sintered at 2100°C.

Grain sizes were also estimated from SEM images of etched samples. Molten salt etching was used for β-SiC-graphene samples sintered at 2000, and 2100 °C. In the etching process, etchant selectively etches the grain boundary delineating the microstructure. Figure V.4 shows variation of microstructure based on powder preparation and graphene content for samples sintered at 2000°C. Linear intercept method was used to estimate grain sizes from the SEM images and the shape correction factor employed was 1.22 considering equiaxed grains. At 2000°C sintering temperature, grain size vary only marginally with the addition of graphene for both preparation process. For AHPCS-%C samples grain size reduced from 338 nm for 2wt% C to 321 nm for 5 wt% C addition. Similarly, for SiC-%C samples grain size also varied from 354 nm for 2wt% to 328 nm for 5wt% C addition. Figure V.5 shows variation of microstructural change based on powder preparation and graphene content for samples sintered at 2100°C. It is interesting to note that at 2100°C sintering temperature, refinement of grain is much prominent compared to 2000°C samples. For instance, AHPCS-%C samples showed average grain size of 430 nm for 2wt% C whereas 5wt% C samples had average grain size of 335 nm. Similar grain refinement was found in case of SiC-%C samples. SiC-2wt%C had an average grain size of 436 nm and addition of 5wt% C changed the average grain size to 385 nm. Note that the darker regions in the images are not inherent porosity of the samples, those are result of etching.

From the results presented here it is possible to conclude that addition of graphene as a filler material certainly affect grain coarsening process. It acts as a barrier for surface diffusion leading to grain size refinement. Moreover, this effect is more prominent in case of higher sintering temperature as discussed above. One of the challenges in SiC sintering is restriction of grain growth during sintering and addition of graphene nanoplatelets have shown to be effective in doing so, particularly, at higher sintering temperature.

V.5 Thermal stability of graphene

Processing of SiC requires high sintering temperature and simultaneous pressure application for dense bulk form. These processing parameters are considered harsh for any carbon allotropes being introduced in the SiC matrix as filler material. Hence it is critical to obtain information regarding the structural defects that are being introduced due to these processing conditions. In the current study, as-received graphene nanoplatelets were subjected to different pyrolysis cycle to observe any change in the x-ray diffraction peak as shown in Fig. V.6. It should be mentioned here that these are not exfoliated graphene that were subjected to pyrolysis cycle.

For as received graphene, we can see a prominent peak at 26.4°that corresponds to (002) plane of graphite. Four other small peaks are observed at 44.4°, 54.5°, 77.4°, and 83.3° corresponding to (100), (004), (110), and (112) planes of graphite. Pyrolysis to 1000°C or 1250°C showed no change in the peak positions or peak shape for the nanoplatelets.

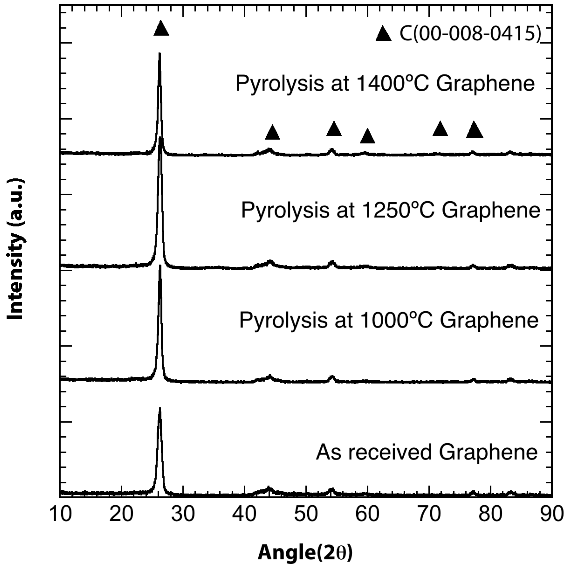

Figure V.6: XRD patterns for as-received graphene and pyrolyzed to different temperatures.

However, at 1400°C a new peak corresponding to (103) plane can be seen at 60°. This peak suggests crystallization of the nanoplatelets at 1400°C.

The experiment mentioned above subjects the nanoplatelets to higher pyrolysis temperature. To understand the complex effect of SPS sintering another set of experiments were performed on different graphene-SiC samples using Raman spectroscopy. Raman spectroscopic analysis can help in detecting number of layers of graphene present in the composite. Moreover, introduction of defects can be identified using this technique. Raman signal of graphene is strong and comparable to graphite. Graphitic structure usually have three distinct peaks. Peak at $\sim$ 1350 cm^{-1} is called D peak (in-pane stretching mode) that provides information on defects present in the crystal structure. The other two peaks are G peak at $\sim$1580 cm^{-1} that represents in-plane vibration of sp^2 carbon atoms and $G^{'}$ peak at $\sim$ 2700 cm^{-1} that represents second order of zone-boundary phonons [147]. The marked difference between Raman signal of graphene and graphite is the shape and intensity of the $G^{'}$ band. In case of graphene, this band is sharp and can be considered a single peak. On the contrary, in graphite, this band is broader and considered a convolution of two peaks. Moreover, intensity of $G^{'}$ peak is almost twice the intensity of G peak in single

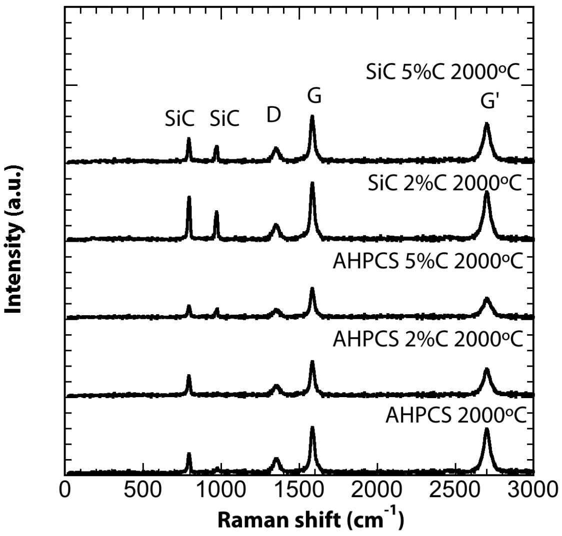

(a)

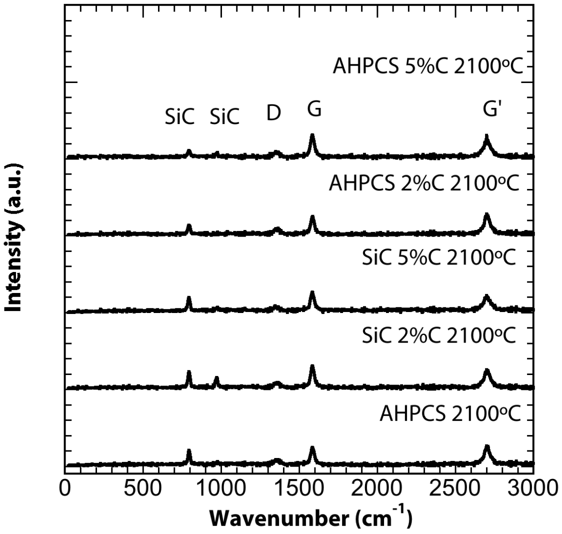

(b)

Figure V.7: Raman Spectra for (a) 2000°C samples and (b) 2100°C samples before normalization.

layer graphene and this can be used to identify single layer graphene. In the current study, we are interested in determining the number of layers qualitatively from the $G^{'}$ peak shape and intensity. We also want to determine defect density after sintering process. Density of defects in graphitic materials is determined using the ratio of intensities of D to G peaks (I_D/I_G).

For the current study, freshly cleaved SiC and graphene-SiC samples were studied using 532 nm laser excitation. The laser power was kept at 0.8mW to prevent any heat induced change in the observed spectra. 100μm spot size was used to collect information from a broad region. For 3C-SiC transverse optical (TO) band is observed at 796 cm^{-1} and longitudinal optical (LO) band is observed at 972 cm^{-1}. Fig. V.7 shows Raman spectra for all SiC and SiC-graphene samples sintered at 2000 and 2100°C. Without any presence of carbon, the Raman spectra of 3C-SiC would only contain two peaks at 796 and 972 cm^{-1}. However, even for monolithic SiC samples D, G and $G^{'}$ peaks were observed at 1350, 1583, and 2701 cm^{-1} respectively. This is due to the excess carbon present in the SiC matrix. Similar D, G and $G^{'}$ peaks were also observed for all the other graphene-SiC samples. To determine the effect of SPS processing, we have to unambiguously identify the contribution of graphene nanoplatelets in these spectra. One way to deconvolute these spectra was to normalize these spectra with respect to a common peak. To do so, there are few assumptions. First of all, the absorption coefficient does not change in these materials. And a peak for SiC should have similar intensity in all these materials since the spectrum is collected over a broad region. Considering these, 796 cm^{-1} TO peak intensity ratio was chosen as a normalizing factor for all the materials. Raman spectra for all the samples after normalization is shown in fig. V.8.

Finally, the spectra for monolithic SiC was subtracted from graphene-SiC spectra to get Raman signal only from graphene nanoplatelets as shown in fig. V.9. After subtraction, D, G, and $G^{'}$ peaks can be identified for AHPCS-2wt% C and AHPCS-5wt% C samples sintered at 2000 and 2100°C. However, negative D, G, and $G^{'}$ were observed for SiC-2wt%

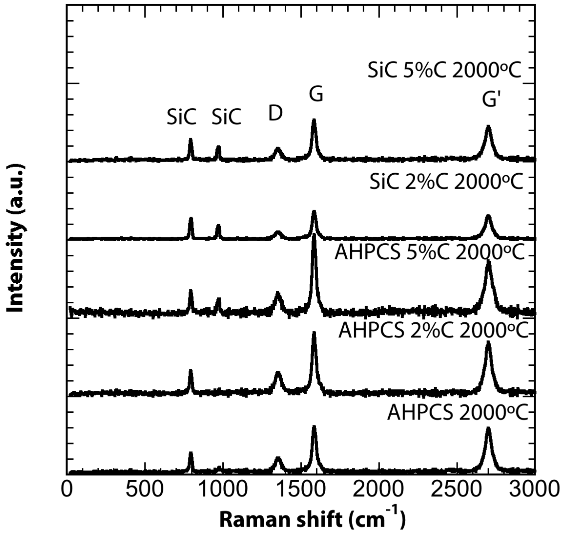

(a)

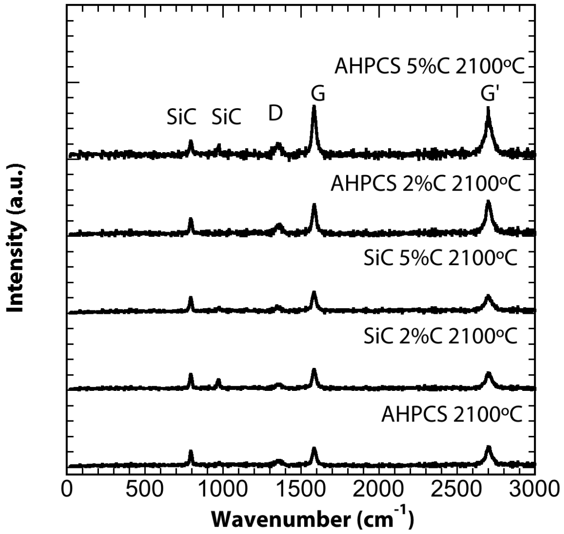

(b)

Figure V.8: Raman Spectra for (a) 2000°C samples and (b) 2100°C samples after normalization using 796 cm^{-1} peak ratio as normalizing factor.

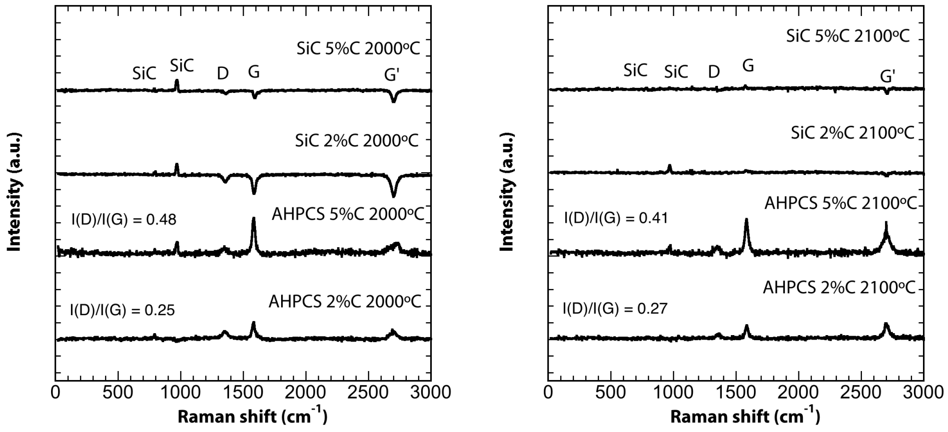

(a) (b)

Figure V.9: Raman Spectra for (a) 2000°C samples and (b) 2100°C samples after subtraction of the spectra of monolithic SiC.

C and SiC-5wt% C samples sintered at 2000°C. For 2100°C sintering temperature, no D, G, and G$^{\prime}$ were observed for SiC-2wt% C and SiC-5wt% C samples.

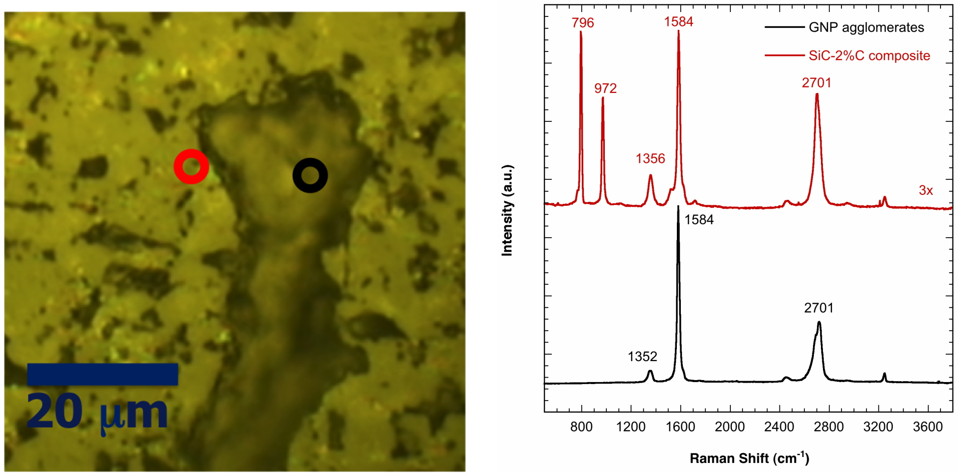

(a) (b)

Figure V.10: (a) Image of SiC-2%C sample with circles indicating places of Raman measurement, and (b) Raman spectra for those two positions.

Raman spectroscopy on the surface of SiC-%C samples was used to investigate the anomaly described above. 2 μm spot size was used to ensure the spectra was collected from a small region. Fig. V.10(a) shows an image of the SiC-2%C sample surface with red and black circle indicating positions of the sample where Raman measurements were taken. From fig. V.10(b) it can be observed that Raman spectra for the black circle indicates only presence of carbon. Peak corresponding to SiC is not present in that spot. The spectra shows D, G, and G$^{\prime}$ peak which are characteristic peaks for graphite or graphene. It is interesting to notice that the intensity ratio of G$^{\prime}$ to G is $\sim$0.43 in this spectra and this suggests that it is a characteristic spectra for crystalline graphite [183]. Moreover, the G$^{\prime}$ peak is broader and is a convolution of two components. After moving away from the black circle to the red circle, the spectra changes and presence of SiC TO (796) and LO (972) peaks can be seen. Also, intensity ratio of G$^{\prime}$ to G peak changes to a higher number indicating few layers of graphene. Hence, it can be concluded that SiC-2%C sample contains regions of graphene agglomerates in the form of graphite.

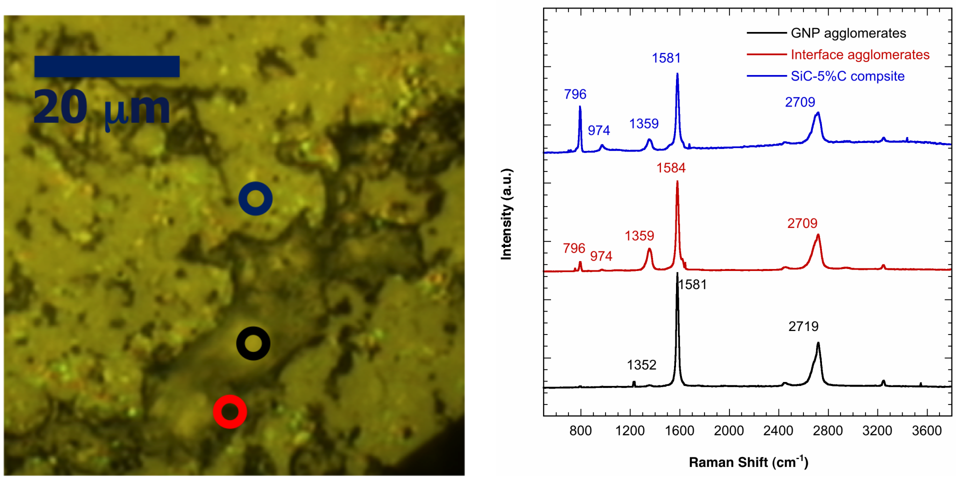

(a) (b)

Figure V.11: (a) Image of SiC-5%C sample with circles indicating places of Raman measurement, and (b) Raman spectra for those three positions.

Slightly different behavior was observed for SiC-5%C sample as shown in fig. V.11. For this sample three locations were chosen to get Raman spectrum (fig. V.11(a)). The black circle is in the center of the crevice, the red circle is at the interface of the crevice and the surface, and the blue circle is away from the crevice. Now, from fig. V.11(b), Raman spectrum at the black circle corresponds to crystalline graphite (graphene agglomerates) as was observed for SiC-2%C. Moreover, the G$^{\prime}$ peak is at a higher wavenumber (2719) and the D peak is very weak. This suggests that this spectra refers to crystalline graphite without defect. At the interface, Raman spectrum shows presence of SiC (two small peaks) and a higher D (1359) peak. This higher D-band infers chemical bonding between SiC and GNP agglomerates. Even after moving away from the agglomerates, the Raman spectrum does not change significantly. For the composite (blue circle), the spectrum shows TO (796) and LO (972) peaks for SiC and D, G, and $G^{'}$ bands for graphite. Note that intensity for $G^{'}$ band was less than half of intensity of G band and was still at a higher wavenumber. This indicates presence of agglomerates even on the surface. Therefore, it is certain that SiC-5%C contains larger regions of GNP agglomerates.

From the above discussion, it can be inferred that SiC-2%C and SiC-5%C samples contain agglomerates and Raman spectra collected from these materials would have effect of these agglomerates on the intensity of D, G, and $G^{'}$ band. Wang *et al.* have reported that intensity of G band is almost similar for monolayer graphene and graphite [184]. However, with increase in number of graphene layers there is linear increase in intensity of G band till 10 layers and after that it starts to decrease. As SiC sample produced Raman spectrum that resembled spectrum of multilayer graphene, it will have higher G band intensity compared to SiC-%C sample which contains crystalline graphite. Moreover, $G^{'}$ band in GNP agglomerates produced much lower intensity as compared to multilayer graphene. As a result, subtraction of spectrum of monolithic SiC from SiC-%C samples resulted in negative peak.

Number of graphene layers

Graf *et al.* developed a method to determine number of graphene layers from the relative integrated intensity of $G/G^{'}$ [185]. According to their work, the relative integrated intensity of $G/G^{'}$ varies from 0.25 to 0.63 linearly for 1 to 4 number of graphene layers. Then the ratio becomes 0.7 for 6 layers and above 0.85 the number of layers is more than 10, therefore making it difficult to distinguish between multilayer graphene and graphite. For the current study, after subtraction of the spectrum of monolithic SiC, we had spectrum only from the platelets added to the matrix. Those spectra were used for calculating the integrated intensity ratio of G and $G^{'}$. For samples sintered at 2100°C, AHPCS-2%C and

AHPCS-5%C had the integrated intensity ratio of 0.56, and 0.81 respectively that suggest $\sim$4 layers of graphene in AHPCS-2%C and more than 6 layers of graphene in AHPCS-5%C sample. For samples sintered at 2000°C, the ratio were 0.6, and 0.9 for AHPCS-2%C, and AHPCS-5%C samples respectively. Therefore, we can consider AHPCS-2%C samples had better exfoliation of graphene platelets and had platelets containing 4–5 layers of graphene sheets. However, at 5wt% loading the platelets were not exfoliated as compared to 2wt% samples and had 6 or more graphene sheets in them.

Defect density

Density of defects in graphitic materials is usually inferred from the ratio of intensities of D to G peaks (I_D/I_G). The D to G peak intensity ratios are presented in fig. V.9 for samples sintered at 2000, and 2100°C. Average defect density for both sintering temperature shows similarity. At 2wt% the defect density is almost 1.5–2 times the defect density at 5wt%. As 2wt% samples had better exfoliation, that resulted in higher surface area for graphene platelets to interact with the host matrix and induce more defects. Moreover, higher multiplication of GNPs due to exfoliation also results in higher defect density. On the contrary, 5wt% samples had more number of graphene layers that resembles nanocrystalline graphite. Hence, the defect density was much lower for 5wt% sample. This behavior has been observed for other graphene-ceramic composite [186].

V.6 Effect of graphene nanoplatelets on hardness of nanocomposites

The focus of this study is to improve toughness of SiC matrix using graphene nanoplatelets as reinforcing filler. However, it is desirable to keep other mechanical properties of SiC at least similar to the matrix properties if not enhanced. Hardness is ability of a material to resist permanent deformation under load. Hence it is critical to understand the effect of addition of graphene on hardness of the composites. Surprisingly, most of the published literature do not report the effect of nanofiller addition on hardness of the composite. Generally, it is considered that addition of a nanofiller would increase or decrease the hardness of the composite depending on the hardness of the 2nd phase. Nonetheless, effect of nanofillers in deciding the hardness of the host matrix is not well explained in literature.

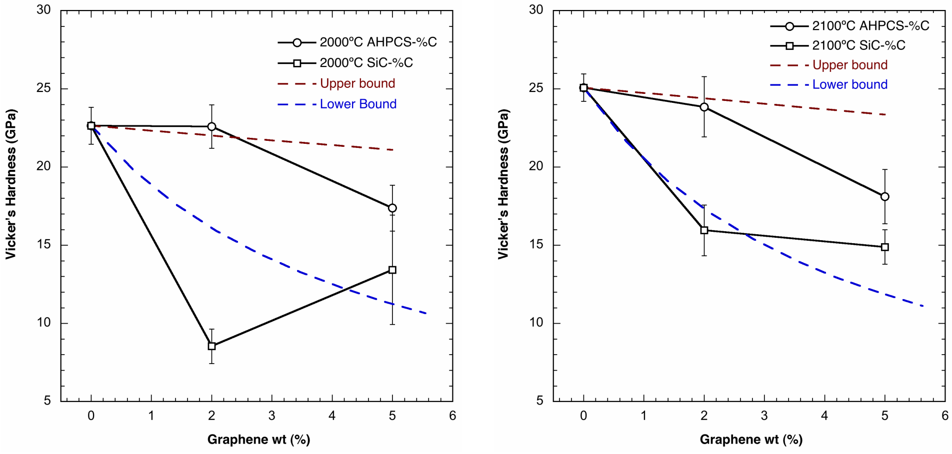

(a) (b)

Figure V.12: Vickers hardness for (a) 2000°C samples and (b) 2100°C samples as a function of graphene weight fraction.

Vickers hardness is plotted in fig. V.12 as a function of graphene weight fraction for graphene-SiC matrix sintered at 2000°C and 2100°C. From the figure, we can see that hardness varies as a function of graphene content. Moreover, this variation also depends on the processing route that was used. In literature, various allotropes of carbon such as fiber or nanotube are considered as a soft phase [187] and considered a reason for decrease in hardness of the composites. Recently, Kim reported the use of rule of mixture for estimating the hardness of a composite with a soft and a hard phase as shown below [188].

$$H_c^{up} = v_h H_h + v_s H_s \tag{V.6}$$

$$H_c^{low} = \frac{1}{v_h/H_h + v_s/H_s} \tag{V.7}$$

Where, H_h and H_s are hardness values of hard and soft phases, respectively. v_h and v_s are the volume fractions of hard and soft phases, respectively. The subscript 'up' is for upper bound and subscript 'low' is for lower bound of hardness of the composite. These equations are based on Reuss and Voigt model where Reuss model consider that all the elements of the composite bear equal stress (Eq V.7) and Voigt model considers that all the elements undergo equal strain (Eq V.6). If we consider SiC matrix to be hard phase and graphene nanoplatelets to be soft phase, then we can calculate the volume fraction by using

$$v_s = \frac{\rho_c}{\rho_s} w_s \tag{V.8}$$

$$v_h = \frac{\rho_c}{\rho_h} w_h \tag{V.9}$$

Where ρ_c is density of the composite, ρ_s and ρ_h are densities of soft and hard phases, respectively. So, the volume fraction of graphene is, $v_s = 0.0292$ when $w_s = 0.02\%$ and $v_s = 0.0729$ for $w_s = 0.05$. It should be noted that Reuss and Voigt models do not take porosity into account. Therefore, hardness of SiC was considered to be 22.64 and 25.08 GPa for 2000 and 2100°C sintering temperature respectively. These values represent the hardness of these materials with almost similar porosity. For the soft phase, hardness of graphite was considered to be $H_s = 1.5$ GPa. Following equations V.6 and V.7 we found the upper and lower bound of the hardness of the composites as shown in fig. V.12.

It is postulated that uniform distribution of soft phase will lead to hardness close to upper bound whereas non-uniform dispersion of soft phase will lead to hardness value close to lower bound. From the table we can see that for AHPCS-2wt% C hardness values are almost similar to upper bound values for both 2000 and 2100°C. However, for AHPCS-5wt% C hardness values are slightly smaller than upper bound values for both 2000 and 2100°C indicating some aggregation. On the contrary, for SiC-%C samples hardness values were close to or lower than lower bound hardness value. Especially, in case of SiC-2wt%C sintered at 2000°C, the hardness value is almost half of lower bound hardness. This sample had much higher porosity ($\sim$15%) compared to all the other samples sintered at 2000°C. Thus the reduction in hardness was a convoluted effect of non-uniform distribution of graphene nanoplatelets and higher residual porosity. As discussed in the previous section, for SiC-%C samples graphene agglomerates in the form of graphite were detected. This indicates formation of agglomerates due to the processing technique can affect hardness adversely.

V.7 Toughening by graphene nanoplatelets

The focus of the current investigation is to increase fracture toughness of SiC matrix by reinforcing it with high strength and high modulus graphene nanoplatelets. The addition of such platelets are expected to increase overall toughness of the composite by inducing various extrinsic toughening mechanisms. Crack trapping is one of the most recognized toughening mechanisms that has been identified around 1960. As crack propagates through the matrix, crack front comes across the filler particles and gets arrested. With increase in load, parts of the crack front bow out if the filler particle is sufficiently tough and meets up with crack front. In this way, energy required for the crack front increases resulting in toughening of the matrix. Another toughening mechanism is crack bridging. Crack bridging occurs when faces of an advancing crack are bridged together by impenetrable particles for some distance behind the crack tip and thereby reduce effective crack-tip intensity. The size of this bridging zone depends on the breaking strength of the filler particles. Crack deflection is another toughening mechanism that includes crack front and filler particle interaction leading to non-planar crack. In this case, as the crack front changes its direction, more surfaces are created and energy required to create those surfaces leads to enhancement in toughness of the matrix material. Crack tip shielding, a toughening mechanism, is observed when a macroscopic crack tip comes across a micro-crack region. The micro-cracks provides a shielding effect by redistributing and reducing the near tip stresses. This in turn increases the fracture toughness.

For the current investigation, fracture toughness values were measured using direct crack measurement (DCM) method. Samples with proper radial cracks were used for toughness measurement. Variation of fracture toughness of graphene-SiC composites is

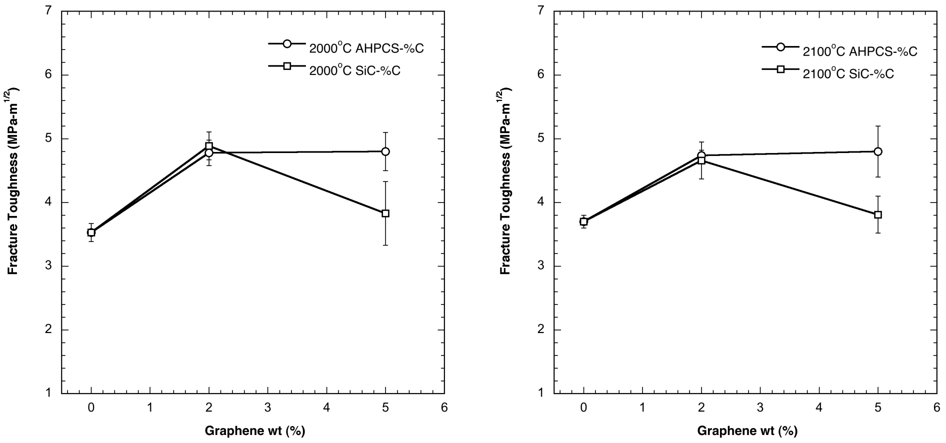

(a) (b)

Figure V.13: Fracture toughness of (a) 2000°C samples and (b) 2100°C samples as a function of graphene weight fraction.

shown in fig. V.13. For AHPCS-2wt%C samples 40% increase in fracture toughness is observed compared to monolithic SiC at 2000°C sintering temperature. Addition of more nanoplatelets do not improve toughness after that. Similarly, we can see improvement of fracture toughness for AHPCS-2wt% C samples over monolithic SiC at 2100°C sintering temperature. Interestingly, SiC-2wt% C also shows improvement in fracture toughness compared to monolithic SiC at both sintering temperature. However, we call this improvement 'apparent'. As we know, in DCM method fracture toughness is a function of load, elastic modulus, hardness and radial crack length. If we consider the load and the crack length to be constant, then we get,

$$K_{IC} \propto \left(\frac{E}{H}\right)^{1/2} \tag{V.10}$$

From Eqn V.10, one can see that fracture toughness is inversely proportional to hardness value. Therefore, reduction in hardness of the material will result in improvement in fracture toughness even though the radial crack length is unaffected by the filler addition. Note that for SiC-2wt%C the hardness values were 62% and 36% lower compared to monolithic SiC sintered at 2000 and 2100°C, respectively. Thus, the apparent improvement in fracture toughness for SiC-2wt% C samples can not be considered due to any toughening by filler material. Surprisingly, this effect has been ignored in published literature. For instance,

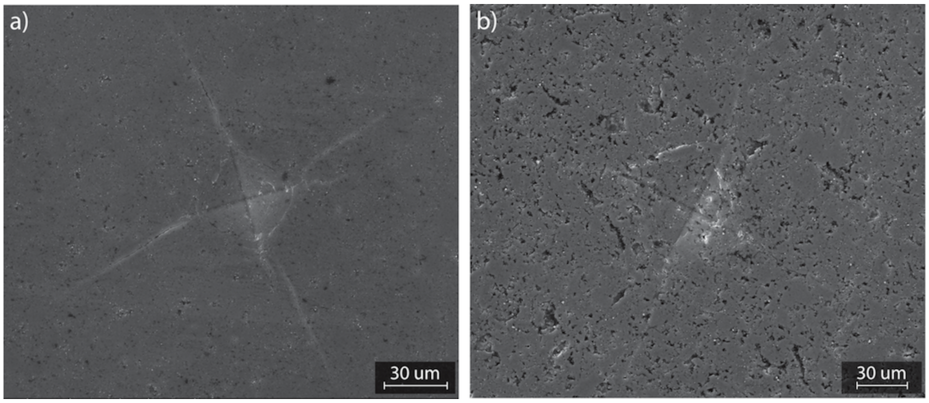

Figure V.14: Indentation radial crack shown for (a) AHPCS-2wt%C and (b) SiC-2wt%C sintered at 2100°C.

Walker et al. reported remarkable increase in fracture toughness of Si_3N_4 by incorporating graphene platelets (GPL) [133]. In their work, fracture toughness of Si_3N_4 increased from 2.8 to 6.6 MPa-$m^{1/2}$ with addition of 1.5vol% GPL. However, hardness value decreased from 22.3 to 15.7 GPa for the same GPL content. It is easily noticeable that this increase in toughness is not only a result of increase in fracture resistance. Rather it is dependent on both increase in fracture resistance and decrease in hardness of the composite. Thus we believe while determining fracture toughness using DCM, this effect of hardness should be considered. Fig. V.14 shows an example of indentation fracture of AHPCS-2wt% C and SiC-2wt% C samples sintered at 2100°C. SiC-2wt%C shows a lot of porosity while AHPCS-2wt% C is quite dense.

Mechanism of toughening

Fracture toughness measurement only provides quantitative values of fracture resistance without providing the reason behind toughening. In order to investigate the toughening mechanism, it is important to analyze crack propagation through these materials. For the current study, crack profiling was used for understanding toughening mechanism.

Crack profiling

For understanding the crack propagation process, monitoring the crack front during indentation would have been ideal. Nonetheless, in-situ crack propagation monitoring is challenging and only possible for transparent materials such as glass. Hence, posteriori examination of the crack can provide valuable information regarding crack front and particle interaction. Indentation cracks for all 2000 and 2100°C samples were examined from

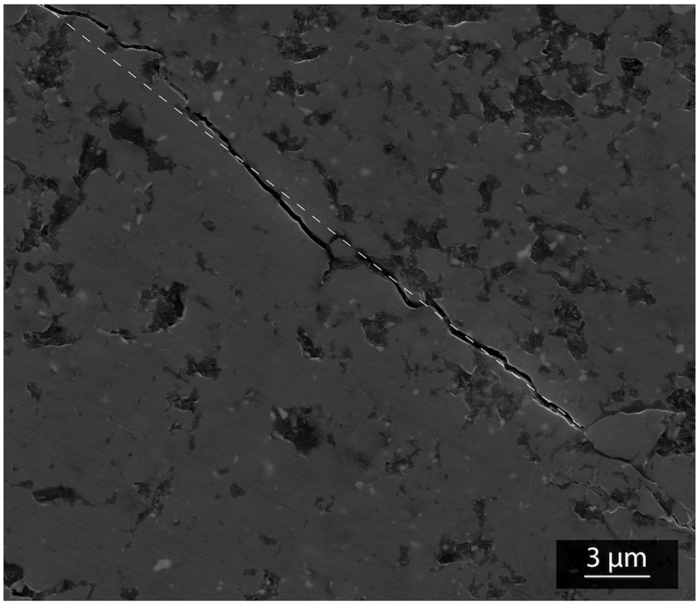

Figure V.15: A representative crack profile for an AHPCS-%C sample.

SEM images. The lengths of the radial crack and change in angle of the crack front were measured with respect to the direction of crack propagation. Fig. V.15 shows a representative crack path and a line indicating the direction of propagation. After measuring the deflection angles, histograms were prepared. The frequency distribution of the deflection angle is presented in fig. V.16(a). The distribution is bimodal in nature for all the materials. The first distribution is for angles between 0 and 5°. For SiC and SiC-2%C sample, this distribution has a higher frequency (0.65) whereas AHPCS-2%C has a much lower frequency (0.3). This indicates toughening in AHPCS-2%C material. The second distribution is centered near 15 and 20° for SiC and SiC-2%C sample respectively. For higher toughness this distribution should translate towards higher deflection angle. For AHPCS-2%C, this distribution shifts towards 35°. This can be clearly understood from fig. V.16(b), where cumulative frequency is plotted as a function of deflection angle. It can be clearly seen that the median deflection angle for SiC, SiC-2%C and SiC-5%C samples are at much lower

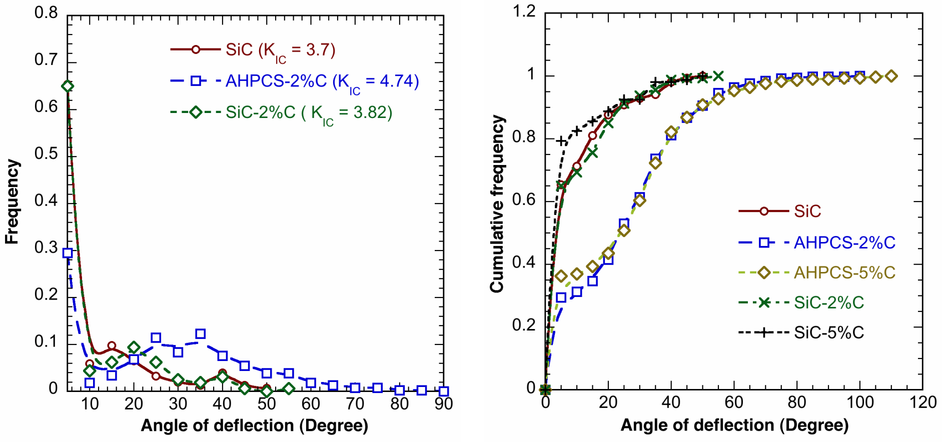

(a) (b)

Figure V.16: Plot of (a) frequency distribution of measured deflection angle (b) cumulative frequency distribution of measured deflection angle.

angle (5°) and correspond to lower fracture toughness. On the other hand, the median deflection angle for AHPCS-2%C and AHPCS-5%C samples increases to $\sim 35°$ representing higher fracture toughness.

Crack deflection model

Faber and Evans developed a theoretical model for different filler geometry and have shown that crack deflection is the dominant mechanism in platelet reinforced ceramic [189, 190]. When an advancing crack meets a secondary inclusion, it tilts at an angle depending on the geometry, position, and residual stress developed between the particle and the matrix. Subsequently, the crack twists if the adjacent filler drives the crack to tilt in the opposite direction. As a result there is increase in fracture surface area leading to larger energy absorption in comparison with monolithic material. While the initial crack front grows under mode I stress intensity, tilting and twisting of the crack forces the crack to grow under mixed mode condition. Hence, increment in toughness by deflection was evaluated using local stress intensities at the tilted and twisted crack front. Using strain energy release rate and stereological projection the following equations were developed by Faber and Evans,

$$\frac{(G_c^t)_{sphere}}{G_c^{matrix}} = 1 + 0.87V_f \tag{V.11}$$

$$\frac{(G_c^t)_{rod}}{G_c^{matrix}} = 1 + V_f(0.6 + 0.014(L/d) - 0.0004(L/d)^2) \tag{V.12}$$

$$\frac{(G_c^t)_{plate}}{G_c^{matrix}} = 1 + 0.28V_f(d/t) \tag{V.13}$$

Where $\frac{(G_c^t)_{sphere}}{G_c^{matrix}}$, $\frac{(G_c^t)_{rod}}{G_c^{matrix}}$, and $\frac{(G_c^t)_{plate}}{G_c^{matrix}}$ are fracture energy ratio of composite to monolithic material for spherical, rod shaped and plate shaped filler material. V_f is the volume fraction of the filler, L/d is the length to diameter ratio for rod, and d/t is the diameter to thickness ratio for plate.

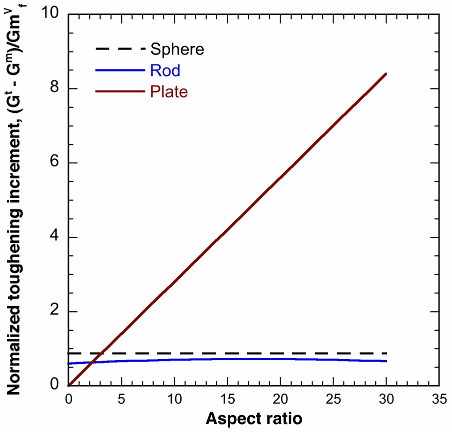

Figure V.17: Normalized toughening increment for crack deflection mechanism as a function of particle aspect ratio for three different morphologies.

Considering these equations, if the increment in toughening (normalized) is plotted against aspect ratio we get fig. V.17. It is interesting to note that plate shaped particles with high aspect ratio can have extreme toughening due to crack deflection mechanism. On the contrary, spherical or rod shaped inclusion show minimal effect on toughening through crack tilting. Hence, it is apparent that graphene platelet with high aspect ratio would provide more toughening compared to carbon nanotube or other spherical inclusion.

For the current investigation, fracture energy was calculated using, $G_c = \frac{K_{Ic}^2(1-\nu^2)}{E}$, where K_{Ic}, E, and ν are fracture toughness, Elastic modulus, and Poisson's ratio respectively. K_{Ic} and E were used from experimental results and ν was assumed to be 0.2. Values of G_c are plotted as a function of weight fraction in fig. V.18. Based on the model, fracture energy should increase with platelet volume fraction if the aspect ratio remains the same. Experimental results show that at 2wt% graphene fracture energy is comparable to the predicted behavior, however, at higher loading condition the behavior of the material deviates from the model. This deviation is due to decrease in aspect ratio of the platelets due to higher platelet thickness at higher weight fraction. To corroborate this we have plotted the theoretical behavior for decreasing aspect ratio with increasing weight fraction and it can be seen that experimental results closely follows the predicted behavior at higher weight fraction.

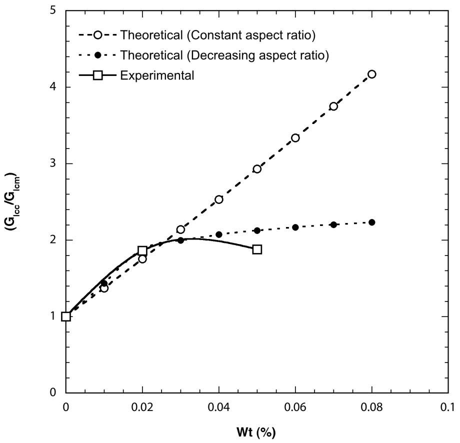

Figure V.18: Increment in fracture energy as a function of weight fraction.

From the above discussion, it can be concluded that crack deflection is the main toughening mechanism observed in the graphene reinforced composites. Moreover, crack profiling process shows that SiC-%C samples do not show toughening behavior as compared to monolithic SiC sample.

V.8 Correlation between toughness and acoustic energy

During Vickers indentation, fracture of brittle material under the indenter results in release of stored elastic strain energy in the form of acoustic emission. Careful monitoring of these acoustic events can help in understanding the fracture behavior of the material. In the current study, acoustic emission events were monitored during Vickers indentation to correlate the fracture behavior to the released acoustic energy. Fig. V.19 show cumulative acoustic energy released during indentation for 2% and 5% graphene reinforced SiC samples sintered at 2000°C. During initial elastic indentation period the energy is much smaller as it only corresponds to the friction between the indenter and the material. After about 15 seconds, there is an abrupt increase in the acoustic events as the material started to fracture till the indentation load reached its nominal value. After that there is minimal acoustic events under constant indentation load. This suggests that crack formation and propagation take place during the initial loading period and hold period does not influence crack propagation significantly. Finally, minimal AE events are observed during unloading. This slight increase is due to friction between the indenter and the surface.

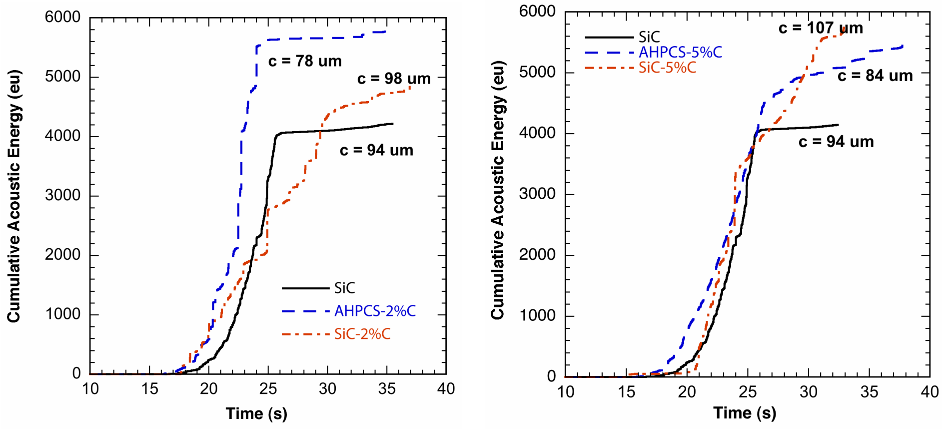

(a) (b)

Figure V.19: Cumulative acoustic energy as a function of time for (a) 2%C samples sintered at 2000°C (b) 5%C samples sintered at 2000°C.

Dyjak et al. divided the acoustic emission events into two parts during indentation [191]. During loading, release of acoustic waves with lower amplitudes were correlated to the formation of radial cracks. Subsequent acoustic waves usually were higher in amplitude that were mainly due to wing cracks developed during unloading. However, in the current study, post-indentation SEM revealed that wing cracks were not formed during unloading.

Hence, abrupt increase in acoustic energy was mainly due to formation of radial cracks during loading.

Cumulative acoustic energy can be correlated to the radial crack growth. Gerberich et al. were the first to correlate the sum of stress wave amplitude to the area swept by the radial crack [192]. They developed the following semi-empirical formula based on elasticity theory,

$$\Delta A \approx \left(\sum g\right)^2 E/K^2 \tag{V.14}$$

Where ΔA is the incremental area swept by the radial crack, $\sum g$ is the sum of the stress wave amplitudes corresponding to the incremental growth, E is the elastic modulus, and K is the stress intensity factor. For a material, E and K would be constant and we will get,

$$\Delta A \propto \left(\sum g\right)^2 \tag{V.15}$$

From the definition of acoustic energy, E, is proportional to the square of the amplitude of the wave. That is $E \propto g^2$. Hence, we can write,

$$\Delta A \propto \Delta E \tag{V.16}$$

From Eqn V.16, it is evident that area swept by the advancing crack is proportional to the increment in acoustic energy recorded during fracture. Gerberich et al. verified this observation experimentally for material with different thickness. Later, Dyjak et al. also observed similar behavior for indentation on silicon carbide. They developed an empirical relation between AE energy and the radial crack length. Based on that relation higher crack length would produce higher acoustic energy. However, fig. V.19 does not seem to show such relationship at a first glance. If we consider larger crack length will result in larger area swept by the crack then looking at table V.3, one can see that SiC, SiC-

Sample	Radial crack length (μm)	Cumulative AE energy (eu)
SiC	94	4144
AHPCS-2%C	78	5772
SiC-2%C	98	5362
AHPCS-5%C	84	5574
SiC-5%C	107	5755

Table V.3: Radial crack length and cumulative AE energy for SiC and graphene reinforced samples sintered at 2000°C.

2%C, and SiC-5%C show this proportional relationship. On the contrary, AHPCS-2%C and AHPCS-5%C even with smaller radial crack length as compared to monolithic SiC, show higher cumulative energy. This can be explained based on the definition of the radial crack length. Radial crack length is the length of the crack from the center of the indent till the end without taking the deflection of the crack into account. Therefore, even with smaller radial crack length, in case of AHPCS-2%C and AHPCS-5%C, higher cumulative acoustic energy was possible since deflection of the radial crack due to the uniform distribution of graphene platelets resulted in higher area swept by the advancing crack. Similar observation was reported by From et al. [193]. They have observed that incorporation of 5 wt% Al_2O_3 in zirconia (ZrO_2) matrix resulted in 16% increase in fracture toughness with higher cumulative acoustic energy. The higher value of cumulative acoustic energy was attributed to energy dissipation during crack propagation as the crack had to overcome the platelet barrier. Mei et al. correlated work of fracture to cumulative acoustic energy carbon fiber reinforced SiC [194]. They concluded that AE energy can be used quantitatively for toughness characterization and is directly proportional to the flexural work of fracture. However, they did not see a direct correlation between fracture toughness and cumulative acoustic energy. Similarly, we can conclude that acoustic energy is not proportional to fracture toughness (radial crack length), but area swept by the crack correlates well with the acoustic energy and can be used as a qualitative tool to understand fracture behavior of ceramic composites.

V.9 Effect of graphene nanoplatelets on strength of nanocomposites

In the current study, the main focus is toughening of the SiC composite through extrinsic toughening mechanisms. However, it is desirable to maintain the strength at the same level as compared to the monolithic SiC. Fig. V.20 shows flexural strength of the composites sintered at 2000 and 2100°C. While AHPCS-%C samples showed 5 – 20% strength improvement, strength reduction was observed for SiC-%C samples. As highly localized residual stresses develop around a second phase in a ceramic composite due to differences in coefficient of thermal expansion (CTE), and elastic properties, size of the platelet plays an important role in deciding unstable crack initiation. When a flaw in a ceramic reaches a critical size, catastrophic fracture initiates. Hence, to understand the effect of the inclusion on strength it is important to calculate the critical flaw size in these composites. To have any strengthening effect on the ceramic composite, the platelet size has to be smaller than the critical flaw size.

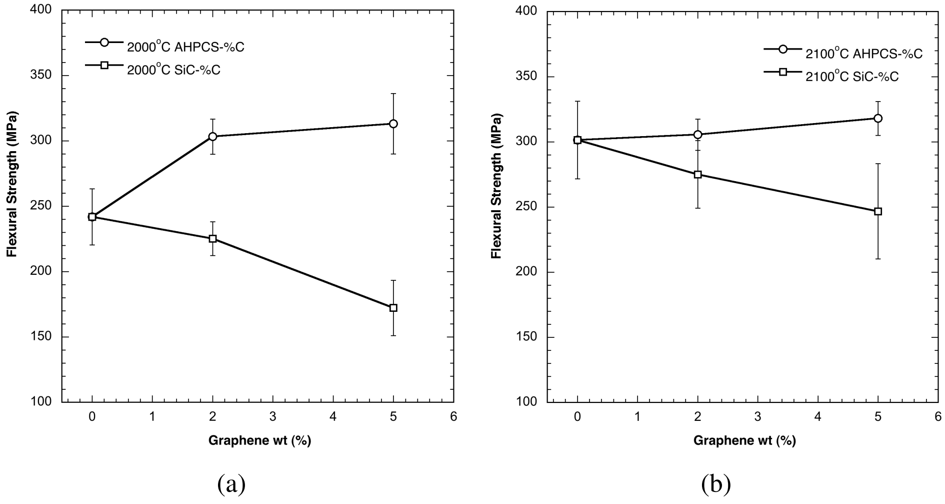

(a) (b)

Figure V.20: Flexural strength as a function of graphene content for (a) samples sintered at 2000°C, and (b) samples sintered at 2100°C.

Based on Griffith's fracture criterion, cracks should be observed adjacent to any second phase particle as maximum tensile stress around the particle does not depend on particle size [195]. However, Davidge and Green showed that the stress around a particle depends on its size [196]. According to them, stresses around a particle is highly localized and limited amount of stored strain energy is associated with a particle based on its size. Hence, crack extension would only occur if the stored strain energy is sufficient. Lange also used an energy balance approach to determine the critical particle size that can result in unstable crack growth [197]. Both of these approach consider spherical inclusion and residual stress around the particle while determining the critical flaw size. Moreover, the volume fraction of the second phase was also ignored in these cases. Pompe *et al.* also used an energy based approach and developed relation for determining the critical flaw size [198]. In their analysis, it was considered that the failure occurs in the matrix adjacent to the particle due high local stress field. This stress field was considered to be a superposition of the external load and the residual stress in the matrix near the platelet. So, the critical the flaw size can be estimated using the following Eqn,

$$C_{crit} = \frac{K_{Ic}^2}{\xi^2(\sigma_f + \sigma_{res})^2} \tag{V.17}$$

Where, K_{Ic} is the fracture toughness, ξ is the compliance function and is 1.25, σ_f is the fracture strength and σ_{res} is the residual stress around the platelet. Residual stress around the platelet can be estimated using Eqn. V.18

$$\sigma_{res_p} = -3v_m \frac{(\alpha_p - \alpha_m)\Delta T}{v_p/K_m + v_m/K_p + 3/4G_m} \tag{V.18}$$

Where α, v, K, G are the coefficient of thermal expansion, volume fraction, bulk modulus, and shear modulus, respectively, and ΔT is the temperature difference on going from the stress free state to room temperature. Subscript p, and m correspond to platelet, and matrix, respectively. Bulk and shear modulus were calculated using elastic modulus of the respective materials. Elastic modulus of SiC was determined using nanoindentation and for graphene it was considered to be 1000 GPa based on literature. For determination of residual stress on the platelet the values of the variables used in Eqn. V.18 are listed in Table V.4. Volume fraction of graphene was considered to be $v_p = 0.0292$ when weight fraction is 2% and $v_p = 0.0729$ when weight fraction is 5%.

Variable	Value	unit
α_p	6×10^{-6}	/°C
α_m	4×10^{-6}	/°C
ΔT	1375	°C
E_m	430	GPa
E_p	1000	GPa
K_m	256	GPa
K_p	641	GPa
G_m	176	GPa

Table V.4: Variables used for calculation of residual stress on platelet due to coefficient of thermal expansion mismatch.

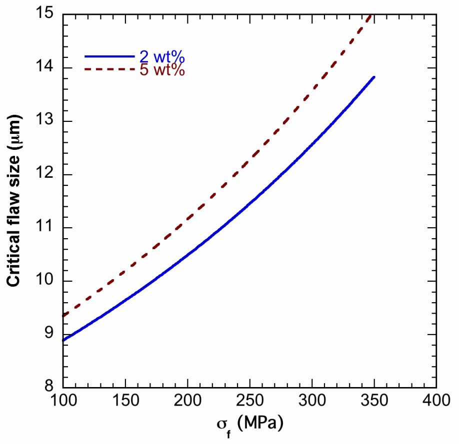

Figure V.21: Critical flaw size as a function of fracture strength.

While determining the critical flaw size using Eqn. V.17, fracture toughness values obtained in this study were used. Critical flaw size for both 2 wt% and 5 wt% samples were plotted as a function of fracture strength in fig. V.21. As shown in fig. V.20, fracture strength varies between 150 MPa to 320 MPa for all the samples tested in this study. Hence, critical flaw size in these composites can be $\sim$ 9.5 – 14 μm depending on the volume fraction and fracture strength of the composites. As the average platelet size used in this study is 5 μm, the platelet would not act as a critical flaw in these composites if they do not form agglomerate due to processing. Therefore, platelet can provide strengthening to the composite.

Strengthening observed in the AHPCS-%C samples was due to two reasons. Firstly, average platelet size in AHPCS-%C samples varied between 3 – 6 μm. Since, platelet size is smaller than critical flaw size and CTE of platelet is higher than matrix, then the residual stress developed in the matrix is compressive in nature. This compressive stress reduces the external tensile load through superimposition and increases strength of the composite. Secondly, strengthening can also occur through toughening. Fracture strength is related to fracture toughness by the following relation,

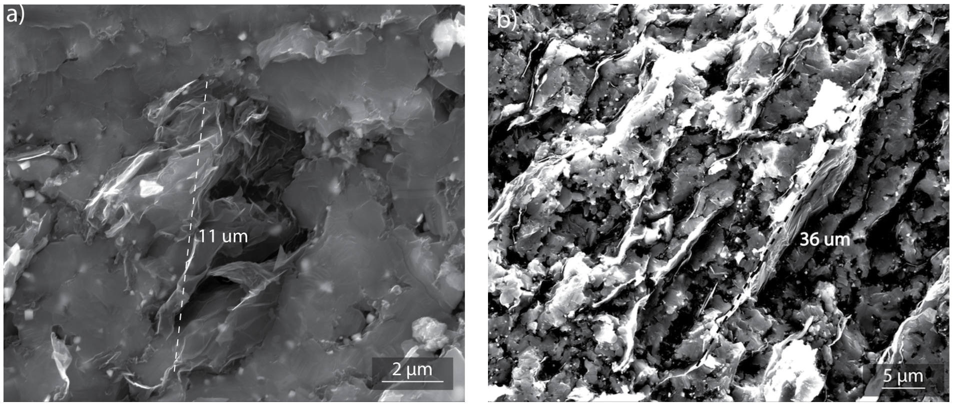

(a) (b)

Figure V.22: Size of agglomerates shown in (a) SiC-2%C sintered at 2000°C, and (b) SiC-5%C sintered at 2000°C.

$$\sigma_f = \beta \left(\frac{K_{Ic}}{c^{1/2}} \right) \tag{V.19}$$

Where β is a constant and c is critical crack length. As we have seen improvement in toughness in AHPCS-%C samples, strengthening is also expected in these material.

On the contrary, SiC-%C samples showed reduction in strength. As all the samples had almost similar relative density, strength can only be affected by agglomerates that are larger than critical flaw size for initiation of unstable crack growth in these composites. To check the size of agglomerates in these samples, SEM images were taken of the fractured surface. Fig. V.22 shows average size of agglomerates seen in SiC-2%C and SiC-5%C samples. Based on the fracture strength, critical flaw sizes for SiC-2%C and SiC-5%C are $\sim$ 10.5 and 10 μm. From fig. V.22 it can seen that the size of the agglomerates are larger than critical flaw size. Such agglomerates act as critical flaw in these composites and act as fracture initiation point. Hence, reduction in strength was observed in these composites compared to monolithic SiC samples. Niihara *et al.* observed similar behavior in SiC platelet reinforced Al_2O_3 composites [199]. With 2μm particle strengthening was observed even for 10 vol%, however, with 8μm particle strength degraded at 10 vol% due to particle size exceeding critical flaw size. Davidge *et al.* reported strengthening in thoria sphere reinforced glass ceramic as the spheres were smaller than critical flaw size and well dispersed in the glass matrix [196].

In summary, platelet reinforcement can result in strengthening in ceramic composite if the platelet size is smaller than the critical flaw size. For AHPCS-%C samples size such was the case and strengthening was observed. On the other hand, improper dispersion of platelets can result in formation of agglomerates that are larger than critical flaw size, and thereby reduces strength of the composite. Formation of agglomerates larger than critical flaw size in SiC-%C samples severely affected strength of those composites by acting as unstable fracture initiation point.

CHAPTER VI

Summary and future work

Polymer pyrolysis technique followed by spark plasma sintering technique was used successfully to fabricate fine grained bulk SiC and graphene-SiC samples by in-situ crystallization of amorphous-SiC obtained from pyrolysis of polymer precursor. Based on experimental results the following has been observed:

1. Polymer pyrolysis yielded starting powder that was mostly amorphous. IR study revealed that hydrosilylation and dehydrocoupling reactions take place during pyrolysis of the polymer. Even at 900°C pyrolysis temperature presence of hydrogen was detected. At 1150°C hydrogen was completely expelled from the structure. Pyrolysis to higher temperature (1400°C) resulted in complete conversion of the polymer.

2. SPS technique was successful in producing high density fine grained SiC. The sintering temperature played a vital role in compacting SiC, where β-SiC phases were formed due to in-situ crystallization of amorphous SiC. Initiation of rapid densification starts around 1900°C sintering temperature as determined from punch displacement data. Increase in the processing temperature resulted in an increase in the relative bulk density from 60% to 95% through ordering of the structure. Grain size measurement using XRD and SEM revealed that crystallite size increased from 97 to 540 nm with increasing sintering temperature from 1600 to 2100 °C. Even with very high sintering temperature grain growth was restricted due to amorphous/nanocrystalline starting powder and SPS sintering technique.

3. Reduction of porosity at higher processing temperature resulted in increase in Vick-

ers hardness. The highest flexural strength of ∼302 MPa was observed for SiC sintered at 2100 °C at a relative density of 95%, which is 4.5% greater than that of near theoretically dense commercially available microcrystalline SiC (Hexoloy SA). Moreover, SiC sintered at 2100°C showed 40% higher fracture toughness compared to Hexoloy SA. For comparison, commercial SiC powder was sintered using an additive. Strength and hardness values were lower for this material due to embrittlement caused by the presence of impurity at the grain boundary. Hence, it is concluded that the combination of polymer pyrolysis with spark plasma sintering technique yields dense SiC with superior mechanical properties while restricting grain growth.

4. Two different dispersion routes were followed to make bulk samples at 2000°C and 2100°C. Thermodynamic calculation showed that the polymer precursor and IPA can be used as a dispersing media. One set of samples were prepared using IPA as dispersing media for dispersion of graphene in SiC matrix. Another set was prepared utilizing AHPCS as dispersing solvent and graphene nanoplatelets were entrapped in SiC matrix after pyrolysis. IR study confirms no change in pyrolysis characteristic due to addition of graphene platelets.

5. Relative density measurement showed that addition of graphene can hinder densification process. Especially at higher weight fraction carbon acts as a barrier to densification mechanisms and results in lower density even at 2000°C. This was more prominent for samples prepared using IPA as dispersing media. On the other hand, addition of graphene as a filler material was shown to affect grain coarsening process. It acts as a barrier for surface diffusion leading to grain size refinement. Moreover, this effect is more prominent in case of higher sintering temperature (40% reduction). One of the challenges in SiC sintering is restriction of grain growth during sintering and addition of graphene nanoplatelets have shown to be effective in doing so, particularly, at higher sintering temperature.

6. Hardness as a function of graphene weight fraction showed different trend for different processing routes. Analysis using Reuss-Voigt model indicated uniform dispersion of graphene content in case AHPCS-%C samples as they showed hardness values close to upper bound hardness values. On the contrary, hardness of SiC-%C samples were close to lower bound hardness values referring to non-uniform dispersion.

7. Addition of graphene nanoplatelet also affected fracture toughness of the composites. AHPCS-2wt%C sample showed 40% improvement over monolithic SiC samples. Analyzing crack profiles and measurement of deflection angle provided insight into toughening process. Frequency distribution of deflection angle confirmed crack deflection to be the main toughening mechanism. Acoustic emission study also corroborated crack deflection to be contributing to the overall toughness of the composite.

8. Critical flaw size was calculated for all the samples. It was observed that for SiC-%C samples formation of agglomerates resulted in platelet size larger than critical flaw size and reduction in strength. However, for AHPCS-%C samples graphene platelets were well dispersed and had strengthening effect. 5–20% improvement was observed for AHPCS-%C samples.

9. Raman spectroscopic analysis confirmed presence of graphene in the final composite structure. Number of graphene layers was estimated from relative integrated intensity ratio of $G/G^{'}$. AHPCS-2%C samples had better exfoliation and 3–4 layers of graphene in the platelets. However, AHPCS-5%C samples had more than 6 layers of platelet and that resulted in a limited improvement in mechanical properties at higher weight fraction.

While a good insight was gained on dispersion of graphene nanoplatelets and its effect on mechanical properties of SiC, there are other aspects of this composite that can be probed further. Detailed analysis presented in this study can be used as a basis for developing a numerical model. Such model can be used to predict variation in properties as a function of graphene weight fraction. Transmission electron microscopy can be used to measure graphene platelet thickness to compare with Raman spectroscopy results. Unfortunately, due to lack of facility this could not be included in the current investigation. One other aspect that can be explored is the study of kinetics during the polymer to ceramic conversion while containing graphene platelets. This would help in understanding the process better in terms of nucleation and grain growth. Moreover, such study can help in tailoring the fabrication process to obtain composites with better mechanical properties.

BIBLIOGRAPHY

[1] R. A. Andrievski, “Synthesis, structure and properties of nanosized silicon carbide,” *Reviews on Advanced Materials Science*, vol. 22, pp. 1–20, DEC 2009.

[2] L. L. Snead, T. Nozawa, Y. Katoh, T.-S. Byun, S. Kondo, and D. A. Petti, “Handbook of SiC properties for fuel performance modeling,” *Journal of Nuclear Materials*, vol. 371, pp. 329–377, SEP 15 2007. 1st Symposium on Nuclear Fuels and Structural Materials for Next Generation Nuclear Reactors, Reno, NV, JUN 04-08, 2006.

[3] R. Munro, “Material properties of a sintered alpha-sic,” *Journal of Physical and Chemical Reference Data*, vol. 26, no. 5, pp. 1195–1203, 1997.

[4] Starfire Inc., “Starfire smp–10 datasheet,”

[5] N. Jepps and T. Page, “Polytypic transformations in silicon carbide,” *Progress in Crystal Growth and Characterization*, vol. 7, no. 14, pp. 259 – 307, 1983.

[6] F. I. Hurwitz, “Suspension of sic powders in allylhydridopolycarbosilane (ahpcs): Control of rheology,” *Ceramic Engineering and Science Proceedings*, vol. 21, pp. 45–52, 2000.

[7] S. Kang, *Sintering: Densification, Grain Growth and Microstructure*. Elsevier Science, 2004.

[8] M. Rahaman, *Ceramic Processing and Sintering*. Materials Engineering, Taylor & Francis, 2003.

[9] R. M. German, P. Suri, and S. Park, “Review: liquid phase sintering,” *Journal of Materials Science*, vol. 44, no. 1, pp. 1–39, 2009.

[10] M. Tokita, “Mechanism of spark plasma sintering,” in *Proceeding of NEDO International Symposium on Functionally Graded Materials*, vol. 21, p. 22, Japan, 1999.

[11] Y. Ding, S. Dong, Z. Huang, and D. Jiang, “Fabrication of short c fiber-reinforced sic composites by spark plasma sintering,” *Ceramics International*, vol. 33, no. 1, pp. 101–105, 2007.

[12] G. Zhan, J. Kuntz, J. Garay, and A. Mukherjee, “Electrical properties of nanoceramics reinforced with ropes of single-walled carbon nanotubes,” *Applied Physics Letters*, vol. 83, pp. 1228–1230, Aug 11 2003.

[13] A. K. Geim and K. S. Novoselov, “The rise of graphene,” *Nature materials*, vol. 6, no. 3, pp. 183–191, 2007.

[14] S. Bae, H. Kim, Y. Lee, X. Xu, J.-S. Park, Y. Zheng, J. Balakrishnan, T. Lei, H. R. Kim, Y. I. Song, *et al.*, “Roll-to-roll production of 30-inch graphene films for transparent electrodes,” *Nature nanotechnology*, vol. 5, no. 8, pp. 574–578, 2010.

[15] C. Lee, X. Wei, J. Kysar, and J. Hone, “Measurement of the elastic properties and intrinsic strength of monolayer graphene,” *Science*, vol. 321, no. 5887, pp. 385–388, 2008.

[16] Y. Fan, L. Wang, J. Li, J. Li, S. Sun, F. Chen, L. Chen, and W. Jiang, “Preparation and electrical properties of graphene nanosheet/al2o3 composites,” *Carbon*, vol. 48, no. 6, pp. 1743–1749, 2010.

[17] ASTM-C1327-08, “Standard test method for vickers indentation hardness of advanced ceramics,” vol. ASTM International, 2008.

[18] K. Jian, Z. Chen, Q. Ma, and W. Zheng, “Effects of pyrolysis processes on the microstructures and mechanical properties of c-f/sic composites using polycarbosilane,” *Materials Science and Engineering A-Structural Materials Properties Microstructure and Processing*, vol. 390, no. 1-2, pp. 154–158, 2005.

[19] C. A. Daniels, *Ceramics: Structure and Properties*. Abyss Books, 2002.

[20] P. K. Mallik, *Fiber-Reinforced Composites: Materials, Manufacturing and Design*. Marcel Dekker, Inc, 1988.

[21] G. Orange, H. Tanaka, and G. Fantozzi, "Fracture-toughnes of pressureless sintered silicon-carbide - a comparison of K_{Ic} measurement methods," *Ceramics International*, vol. 13, no. 3, pp. 159–165, 1987.

[22] M. Ippolito, A. Mattoni, L. Colombo, and F. Cleri, "Fracture toughness of nanostructured silicon carbide," *Applied Physics Letters*, vol. 87, OCT 3 2005.

[23] S. Lee and C. Kim, "Effects of α-SiC versus β-SiC starting powders on microstructure and fracture-toughness of SiC sintered with Al_2O_3-Y_2O_3 additives," *Journal of the American Ceramic Society*, vol. 77, pp. 1655–1658, JUN 1994.

[24] H. Hofler and R. Averback, "Grain-growth in nanocrystalline $TiO_2$and its relation to Vickers hardness and fracture-toughness," *Scripta Metallurgica et Materialia*, vol. 24, pp. 2401–2406, DEC 1990.

[25] J. Karch and R. Birringer, "Nanocrystalline ceramics - possible candidates for net-shape forming," *Ceramics International*, vol. 16, no. 5, pp. 291–294, 1990.

[26] R. Ma, J. Wu, B. Wei, J. Liang, and D. Wu, "Processing and properties of carbon nanotubes-nano-SiC ceramic," *Journal of Materials Science*, vol. 33, pp. 5243–5246, NOV 1 1998.

[27] A. Bravo-Leon, Y. Morikawa, M. Kawahara, and M. Mayo, "Fracture toughness of nanocrystalline tetragonal zirconia with low yttria content," *Acta Materialia*, vol. 50, pp. 4555–4562, Oct 28 2002.

[28] G. Zhan, J. Kuntz, J. Wan, and A. Mukherjee, “Single-wall carbon nanotubes as attractive toughening agents in alumina-based nanocomposites,” *Nature Materials*, vol. 2, pp. 38–42, Jan 2003.

[29] A. Peigney, “Composite materials: Tougher ceramics with nanotubes,” *Nature Materials*, vol. 2, pp. 15–16, Jan 2003.

[30] Y. Zhao, J. Qian, L. Daemen, C. Pantea, J. Zhang, G. Voronin, and T. Zerda, “Enhancement of fracture toughness in nanostructured diamond-SiC composites,” *Applied Physics Letters*, vol. 84, pp. 1356–1358, Feb 23 2004.

[31] J. Kuntz, G. Zhan, and A. Mukherjee, “Nanocriletalline-matrix ceramic composites for improved fracture toughness,” *MRS Bulletin*, vol. 29, pp. 22–27, Jan 2004.

[32] M. Trunec and Z. Chlup, “Higher fracture toughness of tetragonal zirconia ceramics through nanocrystalline structure,” *Scripta Materialia*, vol. 61, pp. 56–59, Jul 2009.

[33] R. Siegel, S. Chang, B. Ash, J. Stone, P. Ajayan, R. Doremus, and L. Schadler, “Mechanical behavior of polymer and ceramic matrix nanocomposites,” *Scripta Materialia*, vol. 44, pp. 2061–2064, May 18 2001.

[34] E. Thostenson, P. Karandikar, and T. Chou, “Fabrication and characterization of reaction bonded silicon carbide/carbon nanotube composites,” *Journal of Physics D-Applied Physics*, vol. 38, pp. 3962–3965, Nov 7 2005.

[35] G. Zhan and A. Mukherjee, “Carbon nanotube reinforced alumina-based ceramics with novel mechanical, electrical, and thermal properties,” *International Journal of Applied Ceramic Technology*, vol. 1, no. 2, pp. 161–171, 2004.

[36] J. Guo, J. Ning, and Y. Pan, “Fabrication and properties of carbon nanotube/SiO2 composites,” in *Composite Materials III* (Zhang, L and Guo, JK and Tuan, WH, ed.), vol. 249 of *Key Engineering Materials*, pp. 1–4, 2003.

[37] A. Peigney, E. Flahaut, C. Laurent, F. Chastel, and A. Rousset, “Aligned carbon nanotubes in ceramic-matrix nanocomposites prepared by high-temperature extrusion,” *Chemical Physics Letters*, vol. 352, pp. 20–25, Jan 24 2002.

[38] I. Chen and X. Wang, “Sintering dense nanocrystalline ceramics without final-stage grain growth,” *Nature*, vol. 404, pp. 168–171, Mar 9 2000.

[39] M. Mayo, D. Hague, and D. Chen, “Processing nanocrystalline ceramics for applications in superplasticity,” *Materials Science and Engineering A-Structural Materials Properties Microstructure and Processing*, vol. 166, pp. 145–159, Jul 15 1993.

[40] R. Averback, H. Hofler, and R. Tao, “Processing of nano-grained materials,” *Materials Science and Engineering A-Structural Materials Properties Microstructure and Processing*, vol. 166, pp. 169–177, JUL 15 1993.

[41] A. Peigney, C. Laurent, E. Flahaut, and A. Rousset, “Carbon nanotubes in novel ceramic matrix nanocomposites,” *Ceramics International*, vol. 26, no. 6, pp. 677–683, 2000.

[42] E. Ionescu, A. Francis, and R. Riedel, “Dispersion assessment and studies on AC percolative conductivity in polymer-derived Si-C-N/CNT ceramic nanocomposites,” *Journal of Materials Science*, vol. 44, pp. 2055–2062, Apr 2009.

[43] L. Gao, L. Jiang, and J. Sun, “Carbon nanotube-ceramic composites,” *Journal of Electroceramics*, vol. 17, pp. 51–55, SEP 2006.

[44] H. Kim, A. Abdala, and C. Macosko, “Graphene/polymer nanocomposites,” *Macromolecules*, vol. 43, no. 16, pp. 6515–6530, 2010.

[45] S. Stankovich, D. Dikin, G. Dommett, K. Kohlhaas, E. Zimney, E. Stach, R. Piner, S. Nguyen, and R. Ruoff, “Graphene-based composite materials,” *Nature*, vol. 442, no. 7100, pp. 282–286, 2006.

[46] W. Knippenberg, *Growth Phenomena in Silicon Carbide*. Philips research reports, Valkenburg, 1963.

[47] R. Ruh, A. Zangvil, and J. Barlowe, “Elastic properties of sic, aln, and their solid solutions and particulate composites.,” *American Ceramic Society Bulletin*, vol. 64, no. 10, pp. 1368 – 1373, 1985.

[48] J. J. Berzelius, “Untersuchungen uber die flussspathsaure und deren merkwurdigsten verbindungen,” *Annalen der Physik*, vol. 77, no. 6, pp. 169–230, 1824.

[49] K. A. Schwetz, *Silicon Carbide Based Hard Materials*, pp. 683–748. Wiley-VCH Verlag GmbH, 2008.

[50] K. Yamada and M. Mohri, “Properties and applications of silicon carbide ceramics,” in *Silicon Carbide Ceramics* (S. Somiya and Y. Inomata, eds.), pp. 13–44, Springer Netherlands, 1991.

[51] D. A. White, S. M. Oleff, R. D. Boyer, P. Budinger, and J. Fox, “Preparation of silicon carbide from organosilicon gels: I. synthesis and characterization of precursor gels,” *Advanced Ceramic Materials;(USA)*, vol. 2, no. 1, 1987.

[52] D. White, S. Oleff, and J. Fox, “Preparation of silicon carbide from organosilicon gels: Ii. gel pyrolysis and sic characterization,” *Advanced Ceramic Materials;(USA)*, vol. 2, no. 1, 1987.

[53] M. Endo and N. Urasato, “Preparation and sintering properties of ultrafine silicon carbide powder obtained by vapor phase reaction,” in *Silicon Carbide Ceramics1*, pp. 119–147, Springer, 1991.

[54] T. Hirai and M. Sasaki, “Silicon carbide prepared by chemical vapor deposition,” in *Silicon Carbide Ceramics1*, pp. 77–98, Springer, 1991.

[55] R. Riedel, M. Seher, J. Mayer, and D. V. Szabó, "Polymer-derived si-based bulk ceramics, part i: Preparation, processing and properties," *Journal of the European Ceramic Society*, vol. 15, no. 8, pp. 703–715, 1995.

[56] S. Yajima, J. Hayashi, and M. Omori, "Continuos Silicon-Carbide fibers of high tensile strength," *Chemistry Letter*, no. 9, pp. 931–934, 1975.

[57] Z. Zhang, C. Scotto, and R. Laine, "Processing stoichiometric silicon carbide fibers from polymethylsilane. Part 1 - Precursor fiber processing," *Journal of Materials Chemistry*, vol. 8, pp. 2715–2724, DEC 1998.

[58] M. Gozzi, M. Goncalves, and I. Yoshida, "Near-stoichiometric silicon carbide from a poly(methylsilylene)/tetra-allylsilane mixture," *Journal of Material Science*, vol. 34, pp. 155–159, Jan 1 1999.

[59] B. Boury, N. Bryson, and G. Soula, "Stoichiometric silicon carbide from borate-catalyzed polymethylsilane-polyvinylsilane formulations," *Applied Organometallic Chemistry*, vol. 13, pp. 419–430, Jun 1999.

[60] Z. Zhang, F. Babonneau, R. Laine, Y. Mu, J. Harrod, and J. Rahn, "Poly(methylsilane) - A high ceramic yield precursor to Silicon carbide," *Journal of the American Ceramic Society*, vol. 74, pp. 670–673, Mar 1991.

[61] D. Seyferth, "Pre-ceramic polymers - past, present, and future," in *Materials Chemistry - An Emerging Discipline* (Interrante, LV and Caspar, LA and Ellis, AB, ed.), vol. 245 of *Advances in Chemistry Series*, pp. 131–160, 1995.

[62] C. Whitmarsh and L. Interrante, "Synthesis and structure of a highly branched polycarbosilane derived from (Chloromethyl) Trichlorosilane ," *Organometallics*, vol. 10, pp. 1336–1344, May 1991.

[63] L. Interrante, K. Moraes, Q. Liu, N. Lu, A. Puerta, and L. Sneddon, “Silicon-based ceramics from polymer precursors,” *Pure and Applied Chemistry*, vol. 74, pp. 2111–2117, NOV 2002.

[64] K. V. Moraes, *The Densification, Crystallization and Mechanical Porperties if Allylhydridoploycarbosilane-Derived Silicon Carbide*. PhD thesis, Rensselaer Polytechnic Institute, USA, 2000.

[65] L. Interrante, J. Jacobs, W. Sherwood, and C. Whitmarsh, “Fabrication and properties of fiber- and particulate-reinforced SiC matrix composites obtained with (A)HPCS as the matrix source,” *CMMC 96 - Proceedings of the First International Conference ON Ceramic and Metal Matrix Composites, Pts 1 AND 2*, vol. 127-, no. Part 1 & 2, pp. 271–278, 1997.

[66] R. German, *Sintering Theory and Practice*. A Wiley-Interscience publication, Wiley, 1996.

[67] R. L. Coble, “Sintering crystalline solids. i. intermediate and final state diffusion models,” *Journal of Applied Physics*, vol. 32, no. 5, pp. 787–792, 1961.

[68] W. D. Kingery, “Densification during sintering in the presence of a liquid phase. i. theory,” *Journal of Applied Physics*, vol. 30, no. 3, pp. 301–306, 1959.

[69] R. M. German, *Liquid phase sintering*. Springer, 1985.

[70] S. Prochazka, “Sintering of silicon carbide.,” *Materials Science Research*, vol. 9, pp. 421 – 431, 1974.

[71] M. Mulla and V. Krstic, “Pressureless sintering of β-sic with al_2o_3 additions,” *Journal of Materials science*, vol. 29, no. 4, pp. 934–938, 1994.

[72] F. Lange, “Hot-pressing behaviour of silicon carbide powders with additions of aluminum oxide,” *Journal of Materials Science*, vol. 10, no. 2, pp. 314–320, 1975.

[73] Y.-W. Kim and M. Mitomo, “Fine-grained silicon carbide ceramics with oxynitride glass,” *Journal of the American Ceramic Society*, vol. 82, no. 10, pp. 2731–2736, 1999.

[74] D. Sciti and A. Bellosi, “Effects of additives on densification, microstructure and properties of liquid-phase sintered silicon carbide,” *Journal of Materials Science*, vol. 35, no. 15, pp. 3849–3855, 2000.

[75] R. Vassen and D. Stover, “Properties of silicon-based ceramics produced by hot isostatic pressing ultrafine powders,” *Philosophical Magazine B-Physics of Condensed Matter Statistical Mechanics Electronic Optical and Magnetic Properties*, vol. 76, no. 4, pp. 585–591, 1997.

[76] R. Vassen and D. Stover, “Processing and properties of nanograin silicon carbide,” *Journal of the American Ceramic Society*, vol. 82, no. 10, pp. 2585–2593, 1999.

[77] Y. Shinoda, T. Nagano, H. Gu, and F. Wakai, “Superplasticity of silicon carbide,” *Journal of the American Ceramic Society*, vol. 82, no. 10, pp. 2916–2918, 1999.

[78] M. Gadzira, G. Gnesin, O. Mykhaylyk, V. Britun, and O. Andreyev, “Solid solution of carbon in β-sic,” *Materials Letters*, vol. 35, no. 56, pp. 277 – 282, 1998.

[79] M. Gadzira, G. Gnesin, O. Mykhaylyk, and O. Andreyev, “Synthesis and structural peculiarities of nonstoichiometric β-sic,” *Diamond and Related Materials*, vol. 7, no. 10, pp. 1466 – 1470, 1998.

[80] O. Yamda, Y. Miyamoto, and M. Koizumi, “High-pressure self-combustion sintering of silicon-carbide,” *American Ceramic Society Bulletin*, vol. 64, no. 2, pp. 319–321, 1985.

[81] J. Qian, G. Voronin, T. W. Zerda, D. He, and Y. Zhao, “High-pressure, high-temperature sintering of diamondsic composites by ball-milled diamondsi mixtures,” *Journal of Materials Research*, vol. 17, pp. 2153–2160, 8 2002.

[82] Z. Munir, U. Anselmi-Tamburini, and M. Ohyanagi, “The effect of electric field and pressure on the synthesis and consolidation of materials: A review of the spark plasma sintering method,” *Journal of Materials Science*, vol. 41, no. 3, pp. 763–777, 2006.

[83] D. M. Hulbert, A. Anders, D. V. Dudina, J. Andersson, D. Jiang, C. Unuvar, U. Anselmi-Tamburini, E. J. Lavernia, and A. K. Mukherjee, “The absence of plasma in “spark plasma sintering”,” *Journal of Applied Physics*, vol. 104, no. 3, pp. 033305–033305–7, 2008.

[84] D. M. Hulbert, A. Anders, J. Andersson, E. J. Lavernia, and A. K. Mukherjee, “A discussion on the absence of plasma in spark plasma sintering,” *Scripta Materialia*, vol. 60, no. 10, pp. 835 – 838, 2009.

[85] S. Diouf and A. Molinari, “Densification mechanisms in spark plasma sintering: Effect of particle size and pressure,” *Powder Technology*, vol. 221, no. 0, pp. 220 – 227, 2012.

[86] Z. Zhaohui, W. Fuchi, W. Lin, L. Shukui, and S. Osamu, “Sintering mechanism of large-scale ultrafine-grained copper prepared by {SPS} method,” *Materials Letters*, vol. 62, no. 24, pp. 3987 – 3990, 2008.

[87] J. Garay, “Current-activated, pressure-assisted densification of materials,” *Annual Review of Materials Research*, vol. 40, no. 1, pp. 445–468, 2010.

[88] G. Molénat, L. Durand, J. Galy, and A. Couret, “Temperature control in spark plasma sintering: an fem approach,” *Journal of Metallurgy*, vol. 2010, 2010.

[89] U. Anselmi-Tamburini, S. Gennari, J. Garay, and Z. Munir, “Fundamental investigations on the spark plasma sintering/synthesis process: Ii. modeling of current and temperature distributions,” *Materials Science and Engineering: A*, vol. 394, no. 1, pp. 139 – 148, 2005.

[90] T. Yamamoto, T. Kondou, Y. Kodera, T. Ishii, M. Ohyanagi, and Z. Munir, “Mechanical properties of beta-sic fabricated by spark plasma sintering,” *Journal of Materials Engineering and Performance*, vol. 14, no. 4, pp. 460–466, 2005.

[91] F. Guillard, A. Allemand, J.-D. Lulewicz, and J. Galy, “Densitication of SiC by SPS-effects of time, temperature and pressure,” *Journal of the European Ceramic Society*, vol. 27, no. 7, pp. 2725–2728, 2007.

[92] A. Lara, A. L. Ortiz, A. Munoz, and A. Dominguez-Rodriguez, “Densification of additive-free polycrystalline β-sic by spark-plasma sintering,” *Ceramics International*, vol. 38, no. 1, pp. 45 – 53, 2012.

[93] Z.-H. Zhang, F.-C. Wang, J. Luo, S.-K. Lee, and L. Wang, “Processing and characterization of fine-grained monolithic sic ceramic synthesized by spark plasma sintering,” *Materials Science and Engineering: A*, vol. 527, no. 78, pp. 2099 – 2103, 2010.

[94] F. Lomello, G. Bonnefont, Y. Leconte, N. Herlin-Boime, and G. Fantozzi, “Processing of nano-sic ceramics: Densification by {SPS} and mechanical characterization,” *Journal of the European Ceramic Society*, vol. 32, no. 3, pp. 633 – 641, 2012.

[95] Q. Shen, R. Li, C. Wang, and L. Zhang, “Densification of short carbon fiber reinforced silicon carbide by spark plasma sintering,” *Composite Materials III*, vol. 249, pp. 133–135, 2003.

[96] R. Li, Q. Shen, and L. Zhang, “Fabrication of short-c-f/sic functionally graded materials,” *Functionally Graded Materials VII*, vol. 423-4, pp. 253–256, 2003.

[97] H. Tang, X. Zeng, X. Xiong, L. Li, and J. Zou, “Mechanical and tribological properties of short-fiber-reinforced sic composites,” *Tribology International*, vol. 42, no. 6, pp. 823–827, 2009.

[98] X. He, Y. Guo, Y. Zhou, and D. Jia, "Microstructures of short-carbon-fiber-reinforced SiC composites prepared by hot-pressing," *Materials Characterization*, vol. 59, pp. 1771–1775, DEC 2008.

[99] B. Kelly, *Physics of Graphite*. RES mechanica monographs, Applied Science Publishers, 1981.

[100] R. Peierls, "Quelques propriétés typiques des corps solides," *Annales de l'instritut Henri Poincaré*, 1935.

[101] L. D. Landau, "Zur theorie der phasenumwandlungen ii.," *Phys. Z. Sowjetunion*, vol. 11, pp. 26–35, 1937.

[102] K. S. Novoselov, A. K. Geim, S. Morozov, D. Jiang, Y. Zhang, S. Dubonos, I. Grigorieva, and A. Firsov, "Electric field effect in atomically thin carbon films," *Science*, vol. 306, no. 5696, pp. 666–669, 2004.

[103] S. Stankovich, D. A. Dikin, R. D. Piner, K. A. Kohlhaas, A. Kleinhammes, Y. Jia, Y. Wu, S. T. Nguyen, and R. S. Ruoff, "Synthesis of graphene-based nanosheets via chemical reduction of exfoliated graphite oxide," *Carbon*, vol. 45, no. 7, pp. 1558–1565, 2007.

[104] Y. Hernandez, V. Nicolosi, M. Lotya, F. M. Blighe, Z. Sun, S. De, I. McGovern, B. Holland, M. Byrne, Y. K. Gun'Ko, *et al.*, "High-yield production of graphene by liquid-phase exfoliation of graphite," *Nature Nanotechnology*, vol. 3, no. 9, pp. 563–568, 2008.

[105] M. Lotya, Y. Hernandez, P. J. King, R. J. Smith, V. Nicolosi, L. S. Karlsson, F. M. Blighe, S. De, Z. Wang, I. McGovern, *et al.*, "Liquid phase production of graphene by exfoliation of graphite in surfactant/water solutions," *Journal of the American Chemical Society*, vol. 131, no. 10, pp. 3611–3620, 2009.

[106] J. Hass, W. De Heer, and E. Conrad, "The growth and morphology of epitaxial multilayer graphene," *Journal of Physics: Condensed Matter*, vol. 20, no. 32, p. 323202, 2008.

[107] C. Berger, Z. Song, T. Li, X. Li, A. Y. Ogbazghi, R. Feng, Z. Dai, A. N. Marchenkov, E. H. Conrad, P. N. First, *et al.*, "Ultrathin epitaxial graphite: 2d electron gas properties and a route toward graphene-based nanoelectronics," *The Journal of Physical Chemistry B*, vol. 108, no. 52, pp. 19912–19916, 2004.

[108] P. R. Somani, S. P. Somani, and M. Umeno, "Planer nano-graphenes from camphor by cvd," *Chemical Physics Letters*, vol. 430, no. 1, pp. 56–59, 2006.

[109] A. Reina, X. Jia, J. Ho, D. Nezich, H. Son, V. Bulovic, M. S. Dresselhaus, and J. Kong, "Large area, few-layer graphene films on arbitrary substrates by chemical vapor deposition," *Nano letters*, vol. 9, no. 1, pp. 30–35, 2008.

[110] X. Li, W. Cai, L. Colombo, and R. S. Ruoff, "Evolution of graphene growth on ni and cu by carbon isotope labeling," *Nano letters*, vol. 9, no. 12, pp. 4268–4272, 2009.

[111] N. Zhan, M. Olmedo, G. Wang, and J. Liu, "Layer-by-layer synthesis of large-area graphene films by thermal cracker enhanced gas source molecular beam epitaxy," *Carbon*, vol. 49, no. 6, pp. 2046–2052, 2011.

[112] D. V. Kosynkin, A. L. Higginbotham, A. Sinitskii, J. R. Lomeda, A. Dimiev, B. K. Price, and J. M. Tour, "Longitudinal unzipping of carbon nanotubes to form graphene nanoribbons," *Nature*, vol. 458, no. 7240, pp. 872–876, 2009.

[113] K. Novoselov, A. K. Geim, S. Morozov, D. Jiang, M. K. I. Grigorieva, S. Dubonos, and A. Firsov, "Two-dimensional gas of massless dirac fermions in graphene," *nature*, vol. 438, no. 7065, pp. 197–200, 2005.

[114] Y. Zhang, Y.-W. Tan, H. L. Stormer, and P. Kim, “Experimental observation of the quantum hall effect and berry’s phase in graphene,” *Nature*, vol. 438, no. 7065, pp. 201–204, 2005.

[115] C. Soldano, A. Mahmood, and E. Dujardin, “Production, properties and potential of graphene,” *Carbon*, vol. 48, no. 8, pp. 2127–2150, 2010.

[116] E. Pop, D. Mann, Q. Wang, K. Goodson, and H. Dai, “Thermal conductance of an individual single-wall carbon nanotube above room temperature,” *Nano Letters*, vol. 6, no. 1, pp. 96–100, 2006.

[117] P. Kim, L. Shi, A. Majumdar, and P. McEuen, “Thermal transport measurements of individual multiwalled nanotubes,” *Physical review letters*, vol. 87, no. 21, p. 215502, 2001.

[118] A. A. Balandin, S. Ghosh, W. Bao, I. Calizo, D. Teweldebrhan, F. Miao, and C. N. Lau, “Superior thermal conductivity of single-layer graphene,” *Nano letters*, vol. 8, no. 3, pp. 902–907, 2008.

[119] C. Lee, X. Wei, Q. Li, R. Carpick, J. W. Kysar, and J. Hone, “Elastic and frictional properties of graphene,” *physica status solidi (b)*, vol. 246, no. 11-12, pp. 2562–2567, 2009.

[120] D. Cai and M. Song, “Recent advance in functionalized graphene/polymer nanocomposites,” *Journal of Materials Chemistry*, vol. 20, no. 37, pp. 7906–7915, 2010.

[121] A. Yasmin and I. Daniel, “Mechanical and thermal properties of graphite platelet/epoxy composites,” *Polymer*, vol. 45, no. 24, pp. 8211–8219, 2004.

[122] T. Ramanathan, A. Abdala, S. Stankovich, D. Dikin, M. Herrera-Alonso, R. Piner, D. Adamson, H. Schniepp, X. Chen, R. Ruoff, S. Nguyen, I. Aksay, R. Prud’homme, and L. Brinson, “Functionalized graphene sheets for polymer nanocomposites,” *Nature Nanotechnology*, vol. 3, no. 6, pp. 327–331, 2008.

[123] A. Yasmin, J. Luo, and I. Daniel, "Processing of expanded graphite reinforced polymer nanocomposites," *Composites Science and Technology*, vol. 66, no. 9, pp. 1182–1189, 2006.

[124] B. Debelak and K. Lafdi, "Use of exfoliated graphite filler to enhance polymer physical properties," *Carbon*, vol. 45, no. 9, pp. 1727–1734, 2007.

[125] K. Kalaitzidou, H. Fukushima, and L. T. Drzal, "A new compounding method for exfoliated graphite–polypropylene nanocomposites with enhanced flexural properties and lower percolation threshold," *Composites Science and Technology*, vol. 67, no. 10, pp. 2045–2051, 2007.

[126] K. Kalaitzidou, H. Fukushima, and L. Drzal, "A new compounding method for exfoliated graphite-polypropylene nanocomposites with enhanced flexural properties and lower percolation threshold," *Composites Science and Technology*, vol. 67, no. 10, pp. 2045–2051, 2007.

[127] G. Chen, D. Wu, W. Weng, and C. Wu, "Exfoliation of graphite flake and its nanocomposites," *Carbon*, vol. 41, no. 3, pp. 619–621, 2003.

[128] G. Chen, H. Wang, and W. Zhao, "Fabrication of highly ordered polymer/graphite flake composite with eminent anisotropic electrical property," *Polymers for Advanced Technologies*, vol. 19, no. 8, pp. 1113–1117, 2008.

[129] S. Bandla and J. C. Hanan, "Microstructure and elastic tensile behavior of polyethylene terephthalate-exfoliated graphene nanocomposites," *Journal of Materials Science*, vol. 47, no. 2, pp. 876–882, 2012.

[130] K. Wakabayashi, C. Pierre, D. A. Dikin, R. S. Ruoff, T. Ramanathan, L. C. Brinson, and J. M. Torkelson, "Polymer-graphite nanocomposites: effective dispersion and major property enhancement via solid-state shear pulverization," *Macromolecules*, vol. 41, no. 6, pp. 1905–1908, 2008.

[131] K. Wang, Y. Wang, Z. Fan, J. Yan, and T. Wei, “Preparation of graphene nanosheet/alumina composites by spark plasma sintering,” *Materials Research Bulletin*, vol. 46, no. 2, pp. 315 – 318, 2011.

[132] J. Liu, H. Yan, M. J. Reece, and K. Jiang, “Toughening of zirconia/alumina composites by the addition of graphene platelets,” *Journal of the European Ceramic Society*, 2012.

[133] L. S. Walker, V. R. Marotto, M. A. Rafiee, N. Koratkar, and E. L. Corral, “Toughening in graphene ceramic composites,” *Acs Nano*, vol. 5, no. 4, pp. 3182–3190, 2011.

[134] P. Hvizdos, J. Dusza, and C. Balazsi, “Tribological properties of si_3n_4-graphene nanocomposites,” *Journal of the European Ceramic Society*, vol. 33, no. 12, pp. 2359 – 2364, 2013. Nanoceramics and Ceramic-based Nanocomposites.

[135] K. Kim, W. Regan, B. Geng, B. Alemán, B. Kessler, F. Wang, M. Crommie, and A. Zettl, “High-temperature stability of suspended single-layer graphene,” *physica status solidi (RRL)-Rapid Research Letters*, vol. 4, no. 11, pp. 302–304, 2010.

[136] D. Long, W. Li, W. Qiao, J. Miyawaki, S.-H. Yoon, I. Mochida, and L. Ling, “Graphitization behaviour of chemically derived graphene sheets,” *Nanoscale*, vol. 3, no. 9, pp. 3652–3656, 2011.

[137] H. Fukushima, *Graphite nanoreinforcements in polymer nanocomposites*. PhD thesis, Michigan State University, 2003.

[138] XG sciences., “xgnp® graphene nanoplatelets - grade m technical data sheet,”

[139] W. Zhao, M. Fang, F. Wu, H. Wu, L. Wang, and G. Chen, “Preparation of graphene by exfoliation of graphite using wet ball milling,” *Journal of materials chemistry*, vol. 20, no. 28, pp. 5817–5819, 2010.

[140] ASTM-C830-00, "Standard test methods for apparent porosity, liquid absorption, apparent specific gravity, and bulk density of refractory shapes by vacuum pressure," vol. ASTM International, 2000.

[141] P. Griffiths and J. De Haseth, *Fourier Transform Infrared Spectrometry*. Chemical Analysis: A Series of Monographs on Analytical Chemistry and Its Applications, Wiley, 2007.

[142] D. Krawitz, A., *Introduction to Diffraction in Materials Science and Engineering*. John Wiley & Sons, 2001.

[143] R. W. Cheary and A. Coelho, "A fundamental parameters approach to x-ray line-profile fitting," *Journal of Applied Crystallography*, vol. 25, no. 2, pp. 109–121, 1992.

[144] K. Vernon-Parry, "Scanning electron microscopy: an introduction," *III-Vs Review*, vol. 13, no. 4, pp. 40 – 44, 2000.

[145] R. Egerton, *Physical Principles of Electron Microscopy: An Introduction to TEM, SEM, and AEM*. Springer Science+Business Media, 2006.

[146] J. Ferraro, K. Nakamoto, and C. Brown, *Introductory Raman Spectroscopy*. Academic Press, 2003.

[147] A. C. Ferrari, J. C. Meyer, V. Scardaci, C. Casiraghi, M. Lazzeri, F. Mauri, S. Piscanec, D. Jiang, K. S. Novoselov, S. Roth, and A. K. Geim, "Raman spectrum of graphene and graphene layers," *Physical Review Letters*, vol. 97, NOV 3 2006.

[148] A. A. Wereszczak, J. J. Swab, and R. H. Kraft, "Effects of machining on the uniaxial and equibiaxial flexure strength of cap3 ad-995 al_2o_3," *ARL Technical Report*, 2003.

[149] ASTM-C1499-05, "Standard test method for monotonic equibiaxial flexural strength of advanced ceramics at ambient temperature," vol. ASTM International, 2005.

[150] J. E. O. Ovri, “A parametric study of the biaxial strength test for brittle materials,” *Materials Chemistry and Physics*, vol. 66, no. 1, pp. 1 – 5, 2000.

[151] G. Anstis, P. Chantikul, B. Lawn, and D. Marshall, “A critical evaluation of indentation techniques for measuring fracture toughness: I, direct crack measurements,” *Journal of the American Ceramic Society*, vol. 64, no. 9, pp. 533–538, 1981.

[152] H. Li, L. Zhang, L. Cheng, Y. Wang, Z. Yu, M. Huang, H. Tu, and H. Xia, “Effect of the polycarbosilane structure on its final ceramic yield,” *Journal of the European Ceramic Society*, vol. 28, no. 4, pp. 887–891, 2008.

[153] H. Li, L. Zhang, L. Cheng, Y. Wang, Z. Yu, M. Huang, H. Tu, and H. Xia, “Polymer-ceramic conversion of a highly branched liquid polycarbosilane for SiC-based ceramics,” *Journal of Materials Science*, vol. 43, pp. 2806–2811, APR 2008.

[154] M. Huang, Y. Fang, R. Li, T. Huang, Z. Yu, and H. Xia, “Synthesis and Properties of Liquid Polycarbosilanes with Hyperbranched Structures,” *Journal of Applied Polymer Science*, vol. 113, pp. 1611–1618, AUG 5 2009.

[155] S. C. Zunjarrao, A. Rahman, and R. P. Singh, “Characterization of the evolution and properties of silicon carbide derived from a preceramic polymer precursor,” *Journal of the American Ceramic Society*, vol. 96, no. 6, pp. 1869–1876, 2013.

[156] R. W. Cheary and A. A. Coelho, “Programs xfit and fourya, deposited in ccp14 powder diffraction library, engineering and physical sciences research council, daresbury laboratory, warrington, england.,” 1996.

[157] A. Krell and P. Blank, “Grain-size dependence of hardness in dense submicrometer alumina,” *Journal of the American Ceramic Society*, vol. 78, pp. 1118–1120, APR 1995.

[158] R. Rice, C. Wu, and F. Borchelt, “Hardness grain-size relations in ceramics,” *Journal of the American Ceramic Society*, vol. 77, pp. 2539–2553, OCT 1994.

[159] E. Ryshkewitch, “Compression strength of porous sintered alumina and zirconia ,” *Journal of the American Ceramic Society*, vol. 36, no. 2, pp. 65–68, 1953.

[160] X. Dong, S. Jahanmir, and L. Ives, “Wear transition diagram for silicon carbide,” *Tribology International*, vol. 28, no. 8, pp. 559 – 572, 1995.

[161] A. Mukhopadhyay, S. Datta, and D. Chakraborty, “On the microhardness of silicon nitride and sialon ceramics,” *Journal of the European Ceramic Society*, vol. 6, no. 5, pp. 303 – 311, 1990.

[162] J. Gong, J. Wu, and Z. Guan, “Analysis of the indentation size effect on the apparent hardness for ceramics,” *Materials Letters*, vol. 38, no. 3, pp. 197 – 201, 1999.

[163] J. Gong, J. Wu, and Z. Guan, “Examination of the indentation size effect in low-load vickers hardness testing of ceramics,” *Journal of the European Ceramic Society*, vol. 19, no. 15, pp. 2625 – 2631, 1999.

[164] M. Flinders, D. Ray, A. Anderson, and R. Cutler, “High-toughness silicon carbide as armor,” *Journal of the American Ceramic Society*, vol. 88, pp. 2217–2226, Aug 2005.

[165] X. Zhang, M. Sixta, and L. De Jonghe, “Grain boundary evolution in hot-pressed ABC-SiC,” *Journal of the American Ceramic Society*, vol. 83, pp. 2813–2820, Nov 2000.

[166] J. Ritter, K. Jakus, A. Batakis, and N. Bandyopadhyay, “Appraisal of biaxial strength testing,” *Journal of Non-Crystalline Solids*, vol. 38-39, Part 1, no. 0, pp. 419 – 424, 1980.

[167] F. Knudsen, “Dependence of mechanical strength of brittle polycrystalline specimens on porosity and grain size,” *Journal of the American Ceramic Society*, vol. 42, no. 8, pp. 376–387, 1959.

[168] M. Giovan and G. Sines, "Biaxial and uniaxial data for statistical comparisons of a ceramics strength," *Journal of the American Ceramic Society*, vol. 62, no. 9-10, pp. 510–515, 1979.

[169] A. A. Wereszczak, J. J. Swab, and R. H. Kraft, "Effects of machining on the uniaxial and equibiaxial flexure strength of cap3 ad-995 al_2o_3," *ARL Technical Report*, 2005.

[170] A. K. Singh, S. C. Zunjarrao, and R. P. Singh, "Processing of uranium oxide and silicon carbide based fuel using polymer infiltration and pyrolysis," *Journal of Nuclear Materials*, vol. 378, no. 3, pp. 238 – 243, 2008.

[171] C. Conner and K. Faber, "Segregant-enhanced fracture in magnesium-oxide," *Journal of Materials Science*, vol. 25, pp. 2737–2742, JUN 1990.

[172] K. Faber and A. Evans, "Intergranular crack-deflection toughening in silicon-carbide," *Journal of the American Ceramic Society*, vol. 66, no. 6, pp. C94–C96, 1983.

[173] T. He, J. Li, L. Wang, J. Zhu, and W. Jiang, "Preparation and consolidation of alumina/graphene composite powders," *Mater Trans*, vol. 50, no. 4, pp. 749–51, 2009.

[174] C. Ramirez, F. M. Figueiredo, P. Miranzo, P. Poza, and M. I. Osendi, "Graphene nanoplatelet/silicon nitride composites with high electrical conductivity," *Carbon*, vol. 50, no. 10, pp. 3607–3615, 2012.

[175] Y. Hernandez, V. Nicolosi, M. Lotya, F. M. Blighe, Z. Sun, S. De, I. McGovern, B. Holland, M. Byrne, Y. K. Gun'Ko, *et al.*, "High-yield production of graphene by liquid-phase exfoliation of graphite," *Nature Nanotechnology*, vol. 3, no. 9, pp. 563–568, 2008.

[176] J. Abrahamson, "The surface energies of graphite," *Carbon*, vol. 11, no. 4, pp. 337–362, 1973.

[177] S. Wang, Y. Zhang, N. Abidi, and L. Cabrales, “Wettability and surface free energy of graphene films,” *Langmuir*, vol. 25, no. 18, pp. 11078–11081, 2009.

[178] W. v. Rijswijk and D. J. Shanefield, “Effects of carbon as a sintering aid in silicon carbide,” *Journal of the American Ceramic Society*, vol. 73, no. 1, pp. 148–149, 1990.

[179] L. Stobierski and A. Gubernat, “Sintering of silicon carbidei. effect of carbon,” *Ceramics international*, vol. 29, no. 3, pp. 287–292, 2003.

[180] E. Ermer, P. Wiesłsaw, and S. Ludosłsaw, “Influence of sintering activators on structure of silicon carbide,” *Solid state ionics*, vol. 141, pp. 523–528, 2001.

[181] K. Wang, Y. Wang, Z. Fan, J. Yan, and T. Wei, “Preparation of graphene nanosheet/alumina composites by spark plasma sintering,” *Materials Research Bulletin*, vol. 46, no. 2, pp. 315–318, 2011.

[182] Y. Fan, M. Estili, G. Igarashi, W. Jiang, and A. Kawasaki, “The effect of homogeneously dispersed few-layer graphene on microstructure and mechanical properties of al2o3 nanocomposites,” *Journal of the European Ceramic Society*, vol. 34, no. 2, pp. 443 – 451, 2014.

[183] A. C. Ferrari, “Raman spectroscopy of graphene and graphite: disorder, electron–phonon coupling, doping and nonadiabatic effects,” *Solid State Communications*, vol. 143, no. 1, pp. 47–57, 2007.

[184] Y. Wang, Z. Ni, Z. Shen, H. Wang, and Y. Wu, “Interference enhancement of raman signal of graphene,” *Applied Physics Letters*, vol. 92, no. 4, pp. 043121–043121, 2008.

[185] D. Graf, F. Molitor, K. Ensslin, C. Stampfer, A. Jungen, C. Hierold, and L. Wirtz, “Spatially resolved raman spectroscopy of single-and few-layer graphene,” *Nano letters*, vol. 7, no. 2, pp. 238–242, 2007.

[186] G. B. Yadhukulakrishnan, S. Karumuri, A. Rahman, R. P. Singh, A. Kaan Kalkan, and S. P. Harimkar, "Spark plasma sintering of graphene reinforced zirconium diboride ultra-high temperature ceramic composites," *Ceramics International*, vol. 39, no. 6, pp. 6637–6646, 2013.

[187] K. Hirota, H. Hara, and M. Kato, "Mechanical properties of simultaneously synthesized and consolidated carbon nanofiber (cnf)-dispersed sic composites by pulsed electric-current pressure sintering," *Materials Science and Engineering: A*, vol. 458, no. 1, pp. 216–225, 2007.

[188] H. S. Kim, "On the rule of mixtures for the hardness of particle reinforced composites," *Materials Science and Engineering: A*, vol. 289, no. 1, pp. 30–33, 2000.

[189] K. Faber and A. Evans, "Crack deflection processes – i. theory," *Acta Metallurgica*, vol. 31, no. 4, pp. 565–576, 1983.

[190] K. Faber and A. Evans, "Crack deflection processes – ii. experiment," *Acta Metallurgica*, vol. 31, no. 4, pp. 577–584, 1983.

[191] P. Dyjak and R. P. Singh, "Acoustic emission analysis of nanoindentation-induced fracture events," *Experimental mechanics*, vol. 46, no. 3, pp. 333–345, 2006.

[192] W. Gerberich and C. Hartbower, "Some observations on stress wave emission as a measure of crack growth," *International Journal of Fracture Mechanics*, vol. 3, no. 3, pp. 185–192, 1967.

[193] P. From, R. Pyrz, B. Clausen, and E. Nielsen, "Indentation and acoustic emission in filtration processed platelet reinforced ceramics," *Materials Science and Engineering: A*, vol. 197, no. 2, pp. 231–236, 1995.

[194] H. Mei, Y. Sun, L. Zhang, H. Wang, and L. Cheng, "Acoustic emission characterization of fracture toughness for fiber reinforced ceramic matrix composites," *Materials Science and Engineering: A*, vol. 560, pp. 372–376, 2013.

[195] A. A. Griffith, “The phenomena of rupture and flow in solids,” *Philosophical transactions of the royal society of london. Series A, containing papers of a mathematical or physical character*, pp. 163–198, 1921.

[196] R. Davidge and T. J. Green, “The strength of two-phase ceramic/glass materials,” *Journal of Materials Science*, vol. 3, no. 6, pp. 629–634, 1968.

[197] F. Lange, “Criteria for crack extension and arrest in residual, localized stress fields associated with second phase particles,” in *Fracture Mechanics of Ceramics* (R. Bradt, D. Hasselman, and F. Lange, eds.), pp. 599–609, Springer US, 1974.

[198] W. Pompe and D. Wilkinson, “Microstructural design of platelet reinforced ceramics,” *Le Journal de Physique IV*, vol. 3, no. C7, pp. C7–1889, 1993.

[199] K. Niihara, A. Nakahira, T. Uchiyama, and T. Hirai, “High-temperature mechanical properties of al2o3-sic composites,” in *Fracture Mechanics of Ceramics* (R. Bradt, A. Evans, D. Hasselman, and F. Lange, eds.), pp. 103–116, Springer US, 1986.

VITA

Arif Rahman

Candidate for the Degree of

Doctor of Philosophy

Dissertation: Fabrication of nanostructured SiC and SiC-exfoliated graphene nanocomposites using spark plasma sintering of polymer derived SiC

Major Field: Mechanical Engineering

Biographical:

Personal Data: Born in Chittagong, Bangladesh on March 25th, 1983.

Education:

Received the B.S. degree from Bangladesh University of Engineering and Technology, Dhaka, Bangladesh, 2006, in Mechanical Engineering

Received the M.S. degree from Oklahoma State University, Stillwater, OK, 2009, in Mechanical Engineering

Completed the requirements for the degree of Doctor of Philosophy with a major in Mechanical Engineering Oklahoma State University in July, 2014.

Experience:

- Worked as a teacher's assistant for several undergraduate and graduate courses from 2007 till 2014
- Worked as a research assistant at Mechanics of Advanced Materials Lab with ceramics for 7 years